REVISTA MILITAR de CIÊNCIA e TECNOLOGIA

Print version: ISSN 0102-3543

Volume XL - 3º Quarter 2023

ENGENHARIA MILITAR

Mobilidade, Contramobilidade e Proteção

BE

Revista Militar de Ciência e Tecnologia

Comandante do Exército:
Gen Ex Tomás Miguel Ribeiro Paiva

Departamento de Ciência e Tecnologia:
Gen Ex Achilles Furlan Neto

Departamento de Educação e Cultura do Exército:
Gen Ex Francisco Carlos Machado Silva

Comandante do Instituto Militar de Engenharia:
Gen Div Juraci Ferreira Galdino

Diretor da BIBLIEx:
Cel Art Marcos Walfrido Ricarte Figueiredo

Direção, Impressão e Distribuição:

Diretor:
Cel Art Marcos Walfrido Ricarte Figueiredo

Editor executivo:
Cap R1 Antônio Carlos Manhães de Souza

Administração, revisão, programação e diagramação:
Coordenação: INSTITUTO MILITAR DE ENGENHARIA – IME

Redação, Diagramação e OJS:
Rubenildo Pithon de Barros
Marcela Fagundes Casotti
Luiz Tadeu Carqueija Mota

Revisão Tikinet:
Revisores: Cristina Saez; Guilherme Oliveira; Piero Kanaan • Diagramador: Lívia Loureiro; Ilário Junior

Impressão e distribuição:
BIBLIEx

Desde 1949
"A Gráfica do Exército" - Compromisso com a Qualidade

Impresso na Gráfica do Exército
Al. Mal. Rondon - Setor de Garagens - QGEx - SMU - CEP:70630-901 - Brasília - DF
Tel: 3415-4367 - Site: http://www.graficadoexercito.eb.mil.br
E-mail: divcmcl@graficadoexercito.eb.mil.br

PUBLICAÇÃO TRIMESTRAL

REVISTA MILITAR de CIÊNCIA e TECNOLOGIA

REVISTA MILITAR DE CIÊNCIA E TECNOLOGIA - Volume XL
3º Trimestre de 2023

INSTITUTO MILITAR DE ENGENHARIA - IME
Praça General Tibúrcio, 80 - Praia Vermelha -
Rio de Janeiro-RJ - CEP 22.290-270 -
Tel.: (21) 2546-7115
Website: https://ebrevistas.eb.mil.br/CT - Email: rmct@ime.eb.br

BIBLIOTECA DO EXÉRCITO
EDITORA (BIBLIEx)
Palácio Duque de Caxias - Praça D. de Caxias, 25
3º andar - Ala Marcílio Dias
Centro - Rio de Janeiro-RJ
CEP 20.221-260
Tel.: (21) 2519-5707

ACESSE NOSSA REVISTA DIGITAL

Nossa capa:
Homenagem ao Quadro de Engenheiros Militares

EDITORIAL

REVISTA MILITAR de CIÊNCIA e TECNOLOGIA

The analysis of current science, technology and society allow us to outline an overview of contemporary Brazilian research. Thus, in an increasingly interconnected and challenging global scenario, the national scientific production from the most diverse public and private academic institutions in the country has stood out for its thematic diversity and methodological depth. Recent advances in areas such as materials engineering, environmental science, information technology and public safety reveal not only the vigor of national research, but also its commitment to strategic and social issues. This editorial brings together seven studies that exemplify this multiplicity of approaches and applications, as well as proposes reflection on these subjects that illustrate this multifaceted advance strongly based on innovation.

High-Performance Materials for Ballistic Defense

The evaluation of the toughness of ultra-high hardness steel for ballistic application by impact test represents a significant advance in materials engineering aimed at personal and vehicular protection. The search for metal alloys able to resist extreme impacts without compromising structural integrity is essential for the development of lighter and more effective armors, with both military and civilian applications.

Regional Biomaterials: The Case of Bovine Hooves in the Northeast

The study of the composition, structure, and effect of water absorption in bovine hooves from the Northeast region reveals the potential of biological materials as sources of knowledge for veterinary, industrial, and environmental applications. The analysis of interaction between organic structure and moisture can contribute to more sustainable practices in livestock and reuse of agro-industrial waste.

Fake News and Social Media: A Computational Approach

The growing concern about digital disinformation is addressed in the review of methods based on propagation data for detecting Fake News on virtual social networks. By investigating how fake news spreads in digital environments, researchers propose more effective algorithms to identify patterns of manipulation and mitigate their effects on public opinion.

Thin Film Technology: Surface Engineering Innovation

The development of a sputtering system with a radio frequency source assisted by magnetic fields to produce thin films represents a technological frontier in the manufacture of electronic, optical, and biomedical devices. Precision in the deposition of materials at the nanoscale is critical for the miniaturization and efficiency of advanced components.

Meteorology, Air Transport and Sustainability

The impact of the closure of airports due to weather conditions on flight delays and the cost of CO_2 emissions highlights the intersection between climate, logistics, and the environment. The analysis of side effects of extreme weather events on air transport reinforces the need for integrated policies that consider both operational efficiency and sustainability.

Green Nanotechnology: Synthesis of $CsFeO_2$ by Sol-Gel/Combustion

The synthesis and characterization of $CsFeO_2$ nanoparticles using the sol-gel/combustion method highlights the role of nanotechnology in the creation of multifunctional materials with magnetic, catalytic and electronic properties. The use of techniques of low-cost and lower environmental impact reinforces the commitment to cleaner and more accessible science.

Smart Public Safety: Acoustic Detection of Gunfire

Finally, advances in the detection of gunfire signals based on acoustic sensors point to technological solutions that can transform the response to situations of urban violence. Intelligent systems capable of identifying gunshots in real time offer crucial support to security forces and the protection of vulnerable communities.

In conclusion, these studies, although diverse in scope, reflect the dynamism of national research and its ability to dialogue with great contemporary challenges. From public security to sustainability, from technological innovation to the valorization of regional resources, national science continues to build bridges between knowledge and social transformation. It is in this context that the Military Institute of Engineering is located, a bicentennial corporate university whose primary objective is to meet the needs of the Brazilian Army, but without leaving aside dual applications that may contribute as much as possible to civil society. Thus, the role to be played by the Military Journal of Science and Technology (RMCT, Open Access Publication), one of the regular publications of the Brazilian Army, is considered paramount in military science and technology.

We wish you an excellent reading!

Dr. Eng. Fernando M. Araujo-Moreira
Editor-in-Chief of RMCT

SUMMARY

VOL.40 Nº3 2023
https://doi.org/10.22491/rmct.v40i3.11270.en

Impact testing to evaluate the toughness of ultra-high hardness steel for ballistic applications

Charles Hudson Martins de Vasconcelos[1,3], charles.vasconcellos@ime.eb.br, Orcid 0000-0002-3472-2998
Cristhian Ricardo Loayza Loayza[2], crislo@ufpa.br, Orcid 0000-0002-0662-715X
Ademir Ângelo Castro Filho[2], engangelo80@gmail.com, Orcid 0000-0003-4713-0817
Eduardo de Magalhães Braga[2], edbraga@ufpa.br, Orcid 0000-0003-0739-7592
Andersan dos Santos Paula[1], andersan@ime.eb.br, Orcid 0000-0002-0904-4240
Ricardo Pondé Weber[1], rpweber@ime.eb.br, Orcid 0000-0002-7431-8316
[1]Instituto Militar de Engenharia - IME, [2]Universidade Federal do Pará - UFPA,
[3]Centro de Instrução Almirante Braz de Aguiar - CIABA

ABSTRACT: *Ultra-high hardness armor grade steels are commonly used in sectors such as patrol vehicles, cash-in-transit vehicles, armored personnel carriers, building protection, among others. The aim of this work was to evaluate the toughness of a material in this class by determining the ductile-to-brittle transition temperature (DBTT) using some of its definitions. Charpy impact tests were conducted and the fracture faces of the specimens were evaluated through both macroscopic and microscopic analysis. The tests were conducted at temperatures ranging from -60°C to room temperature, using specimens extracted longitudinally to the rolling direction. Micrographic analyses indicated that determining the DBTT using the energy absorption criterion is appropriate and reliable. The obtained results show that, based on an absorbed energy of 12.92 J, the transition temperature is -27.73°C.*

KEYWORDS: *Toughness, ductile-to-brittle transition temperature, impact test, ultra-high hardness steel.*

RESUMO: Os aços de nível de blindagem de ultra-alta dureza são comumente utilizados nos setores de veículos de patrulha, veículos de transporte de valores, viaturas blindadas de transporte de pessoas, proteção de edificações, entre outros. O objetivo deste trabalho se constituiu na avaliação da tenacidade de um material dessa classe, determinando a temperatura de transição dúctil-frágil (TTDF) utilizando algumas das suas definições. Realizou-se ensaios de impacto Charpy e a avaliação combinada das faces de fratura dos corpos de prova por macroscopia e microscopia. Os testes foram realizados em temperaturas que variaram de -60°C a temperatura ambiente com corpos de prova retirados longitudinalmente à direção de laminação. As análises micrográficas ostentaram que a determinação da TTDF por critério de absorção de energia é adequada e confiável. Os resultados logrados são que, com base em 12,92 J de energia absorvida, a temperatura é -27,73°C.

PALAVRAS-CHAVE: Tenacidade, temperatura de transição dúctil-frágil, ensaio de impacto, aço de ultra-alta dureza.

1. Introduction

In recent decades, studies involving the field of armor have always been engaged in efforts to provide light armor technologies that can defeat projectiles (Armor-Piercing, AP). To meet these requirements, the availability of tempered and quenched armor steels has been increased, and most importantly, the MIL-DTL-46100E specification has been upgraded to High Hardness Armor (HHA) steels [1]. Although this metal specification has met the intended applications, considerable efforts have been made to develop ultra-high hardness—quenched and tempered (UHH-Q&T) steels with a hardness of 600 HB or more [2].

The various types of steel offered by each supplier are generally differentiated according to a specific and increasing hardness value. The lowest hardness value corresponds to rolled homogeneous armor steel (RHA – 380-430 HBW), then medium hard armor steel (MHA - 420-480 HBW), HHA steel (480-540 HBW), and the highest level of hardness is reached with UHA or UHH-Q&T steel (570-640 HBW) [3].

Focusing on the projectile-target interaction, it can be determined that penetration mechanisms result from the property that represents the degree of deformation a material can withstand before fracturing. In ductile materials, fracture occurs due to the initial stress wave, radial fracture, shattering, plugging, frontal petaling, rear petaling, fragmentation and ductile hole enlargement. However, when a brittle material is used, the entire study can be summarized by the characteristics of fragmentation [4].

These phenomena bring up the need to determine a limit temperature, below which the material's fracture behavior changes from ductile to brittle, in order to predict occurrences of brittle fracture. This temperature is called the Ductile-to-Brittle Transition Temperature (DBTT) of materials and the Charpy impact test is considered to be one of the most suitable for studying this issue [5-7].

By collecting energy absorption data through the Charpy impact test of metallic materials such as UHH-Q&T steel at various temperatures, the DBTT of this material can be determined. It is usually seen that there are two levels of absorbed energy, called the lower shelf and the upper shelf, and a region between them, called the transition zone [8-12].

It is therefore known that at temperatures corresponding to the lower energy absorption shelf, the material will fracture, mainly in a brittle manner with a predominance of the cleavage fracture micromechanism, while at temperatures corresponding to the upper energy absorption shelf, the material will fracture in a mostly ductile manner due to the coalescence of microcavities. A laborious task, however, is to determine the DBTT, which will be a reference temperature for the change in the material's fracture behavior from ductile to brittle as the temperature decreases [10, 13-15].

Checking how the fracture face looks is one of the methodologies for designating the DBTT, ranging from a fracture with a 100% shiny to 100% opaque appearance, and this characterization is done exclusively by visual observation of the fracture face, making it possible to establish a temperature at which the change in fracture micromechanism occurs. However, a suitable criterion would be needed to define the DBTT, as it would be difficult to determine this in experimental practice by evaluating these fractured specimens alone. For this purpose, the methodology indicated in ASTM E23 [16], which is the standard for carrying out the impact test, can be used.

However, the visual comparison method described in the standard is inaccurate, as the photographs to be used for comparison with the fracture faces of the test specimens leave something to be desired in terms of quality, resulting in a comparison with a high probability of inaccuracy [17-20]. It is therefore important to apply other methodologies to determine the DBTT. In the simplest and most accurate method, the DBTT is determined from the curve of absorbed energy as a function of temperature, and one possible criterion in this scenario is to consider that the DBTT is the temperature at which the average energy between the upper and lower levels of the curve is reached, illustrated in Fig. 1 [21-23].

In this context, the objective of this work was to determine the DBTT using some of its definitions combined with macroscopic and microscopic analyses of the fracture surface and metallurgical factors. Different test temperatures were used, in order to cover the range from temperatures at which the material of interest is expected to show 100% brittle fracture to temperatures at which 100% ductile fracture occurs.

2. Material and methods

2.1 Material

The material under study is UHH steel with a yield strength of 1500 MPa, thickness 5 mm, quenched and tempered (QT), classified as armor grade. This material meets the requirements for shape tolerances in accordance with EN 10029 [24], flatness tolerances in accordance with EN 10029 Class N – Steel Type L [24] and surface properties in accordance with EN 10163-2 Class B Subclass 3 [25].

The applicability of this material is as an additional protective sheet, or in cases where weight is critical, providing protection against both penetration and explosions. This same material is used in patrol vehicles, cash-in-transit vehicles (CIT), armored personnel carriers (APCs), building protection and other sectors. The chemical composition and mechanical properties of the material, specified in the standard, are shown in **Tables 1** and **2**, respectively.

Table 1 - Main chemical composition of the material (% mass).

C	Si	Mn	Ni	Cr	Mo	B	S	P
0.47	0.70	1.00	3.00	1.50	0.70	0.0005	0.003	0.01

Source: [26].

Table 2 - Main mechanical properties of the material.

Hardness HBW	Yield strength $Rp_{0.2}$ mín. MPa	Ultimate strength R_m min. MPa	Elongation %
570-640	1500	2000	7

Source: [26].

2.2 Sample preparation

The test specimens were extracted from a 500 x 500 x 5 mm plate of UHH-Q&T steel using the electrical discharge machining process. The specimen dimensions follow the sub-size classification of ASTM E23 [16], i.e., 10 x 5 x 55 mm, with a 2 mm deep V--notch in the 5 mm thickness, a 45° angle, and a root radius of 0.25 mm at the center of the specimen, verified using a profile projector and an optical microscope (OM)).

2.3 Charpy impact test

The Charpy impact tests were conducted in a Panambra impact tester, model PW30/15R, with a 30 J hammer, in accordance with ASTM E23 standard [16], using three specimens for each temperature. The tests began at room temperature (20.8°C) and were extended to lower temperatures: 0°C, -20°C, -40°C and -60°C. To reach these temperatures below room temperature, the specimens were inserted into liquid nitrogen, thus obtaining the absorbed energy as a function of temperature.

In order to evaluate the data obtained through the Charpy test, a curve of absorbed energy as a function of temperature is drawn up, but for better clarity in the analysis, this curve must be adjusted, and the method used was based on that proposed by Ericksonkirk, Shaikh and Ericksonkirk [27]. Using this method, the absorbed energy data as a function of the temperatures used in the test was adjusted using the formulation based on the hyperbolic tangent, which complies with Eq. 1.

$$Y = A + B * tanh\frac{T - D}{C} \qquad (1)$$

In Eq. 1, Y is the variable to be adjusted and T is the test temperature variable. The adjustment variables A, B, C and D are illustrated in **Fig. 1** and are defined as follows: A: average of the energies between the upper and lower shelves; B: range between the energies of the upper and lower shelves; C: half of the transition temperature range; and D: temperature of the average of the lower and upper shelves.

The DBTT value was established according to the following definitions:

- $DBTT_{EA}$: Ductile-to-Brittle Transition Temperature at which the arithmetic mean of the absorbed energies in the upper and lower shelves occurs.
- $DBTT_{BN}$: Ductile-to-Brittle Transition Temperature at which zero ductility transition occurs, i.e., 100% brittle fracture.
- $DBTT_{ND}$: Ductile-to-Brittle Transition Temperature at which there is zero brittleness transition, i.e. 100% ductile fracture.

Fig. 1 - Illustration of the adjustment variables of the hyperbolic tangent equation.

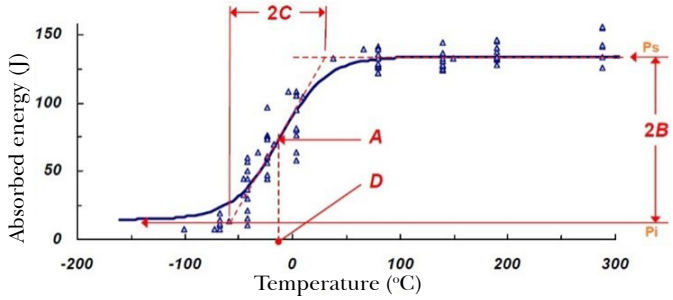

Source: [27].

2.4 Macroscopy versus microscopy of the fracture

Fracture surface analysis was conducted on specimens fractured in Charpy impact tests. The samples were previously cleaned in an ultrasound machine using an acetone solution. For imaging, a ZEISS SteREO Discovery V12 optical stereomicroscope and a FEI Quanta FEG 250 scanning electron microscope (SEM) were used, in accordance with ASTM standard E2142 [28].

3. Results and discussion

The microstructural aspect of the BM observed via OM, the presence of columnar laths and lath blocks after etching with 2% nital solution, can be seen in **Fig. 2(a)**, which confirms that the material is tempered martensitic steel. **Fig. 2(b)** shows the SEM image, which indicates that the laths shown in the previous image are acicular martensite laths.

One of the main purposes was to determine whether or not the material under study exhibits a ductile-to-brittle transition with decreasing temperature and, if so, in what temperature range the phenomenon occurs. The ductile-to-brittle transition is related to temperature by the impact energy measured in the test.

Fig. 2 - Microstructure of BM: (a) micrograph via OM; (b) micrograph via SEM.

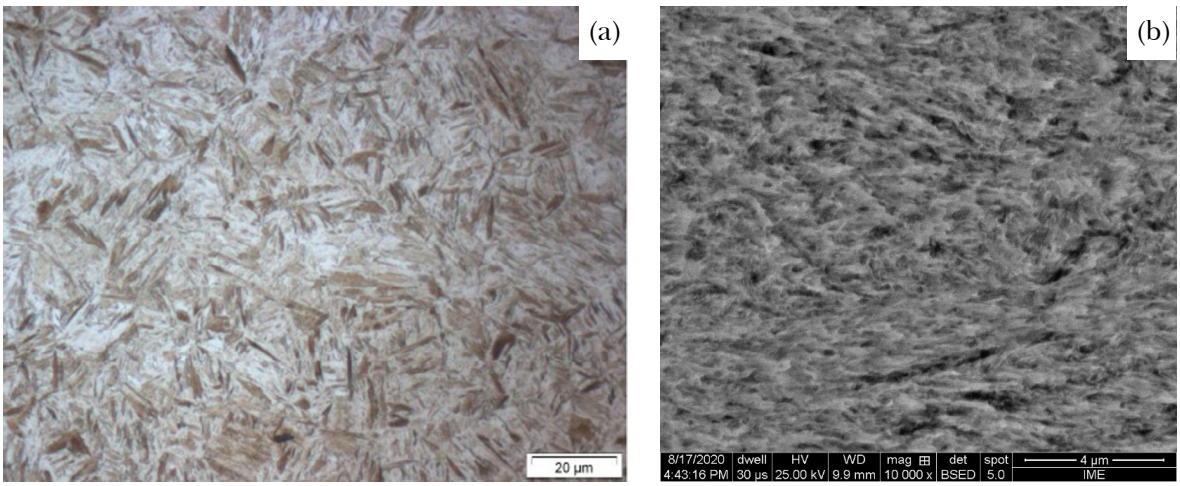

For some researchers, such as Burdekin and Folch [29], the DBTT is defined as the temperature range over which the change in energy levels from low to high occurs. However, as in practice there is usually no sudden change in energy, but rather a transition zone, it is difficult to determine the DBTT precisely. Therefore, a series of tests were carried out at different temperatures combined with macroscopic, microscopic and chemical composition analyses, which allowed the DBTT to be determined, which is an important parameter when selecting a material from the point of view of toughness or tendency to occur brittle fracture [29].

3.1 Absorbed energy

Table 3 shows the values obtained in the Charpy tests using the specimens made from the material under study. It should be noted that all the specimens separated completely during the test.

Table 3 - Charpy impact test results (values in Joule).

Temperature (°C)	CP01	CP02	CP03	Average
20.8	16.0	16.0	16.0	16.0
0.0	15.0	15.0	15.0	15.0
-20.0	15.0	14.0	14.0	14.3
-40.0	10.0	10.0	12.0	10.7
-60.0	10.0	9.0	12.0	10.3

Fig. 3 shows the absorbed energy curve as a function of temperature for the UHH-Q&T steel under study. The behavior of the curve obtained is characteristic of high-strength steels, with a relatively small variation in absorbed energy over a temperature range of -80 to 100°C [5]. It is plausible to see in the curve that at higher temperatures, the impact energy is greater and is compatible with a ductile mode of fracture. As the temperature decreases, the impact energy reduces over a relatively small temperature interval (around 20°C), from which the impact energy presents a low and essentially constant value; in this interval, the fracture mode is brittle.

The absorbed energy value is obtained by directly reading the value on the tester's scale. By plotting these values as a function of the temperature used in the test, it is possible to verify the change in the material's behavior according to the change in temperature. The plateau regions were identified by visual examination of the points plotted on the graph. Thus, it was found that the lower plateau comes at a temperature of -60°C, while the upper plateau comes in the range of 0°C to 20.8°C.

After defining the energy thresholds, the transition region (-40 to -20°C) was adjusted by linear regression. The results are shown in **Fig. 4**. Next, the hyperbolic tangent was adjusted using the MS – Excel Solver function. **Fig. 5** shows the results obtained: the graphical form; the equation of the adjusted hyperbola; and the value of the correlation coefficient (R^2) relating to the adjustment of the experimental points with the hyperbolic tangent curve.

Fig. 3 - Absorbed energy curve as a function of temperature in the Charpy impact test.

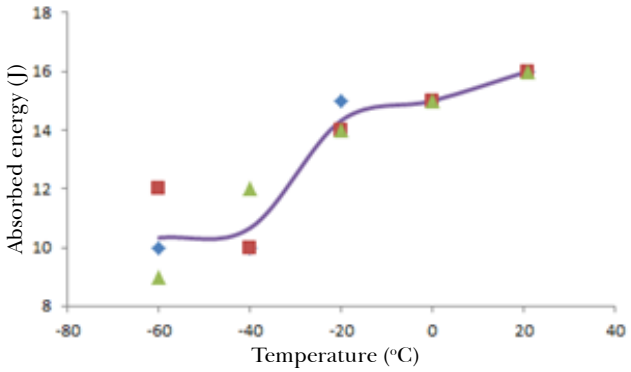

Fig. 4 - Linear regression of the transition region.

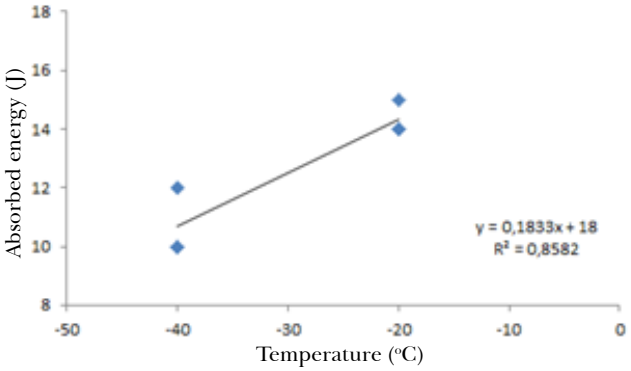

Fig. 5 - Absorbed energy curve as a function of temperature adjusted by the hyperbolic tangent method.

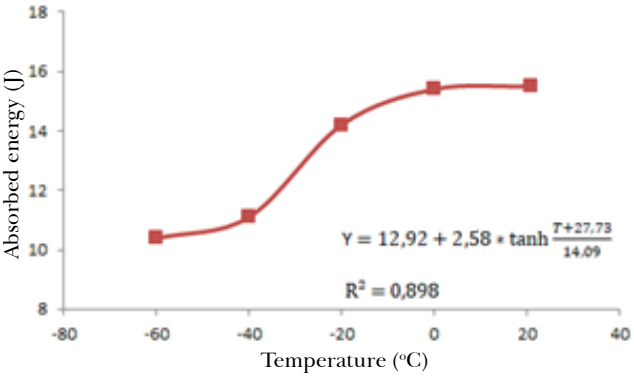

By drawing up the graphs shown, it was possible to determine the following parameters, which are illustrated **in Fig. 6**: temperatures $DBTT_{EA}$, $DBTT_{BN}$ and

$DBTT_{(ND)}$; and energy of the upper parameter (EUP) and lower parameter (ELP). **Table 4** shows the values of these parameters and the temperatures of the upper parameter (TUP) and lower parameter (TLP) by absorbed energy criterion.

Fig. 6 - Parameters $DBTT_{EA}$, $DBTT_{BN}$, $DBTT_{(ND)}$), EUP and ELP.

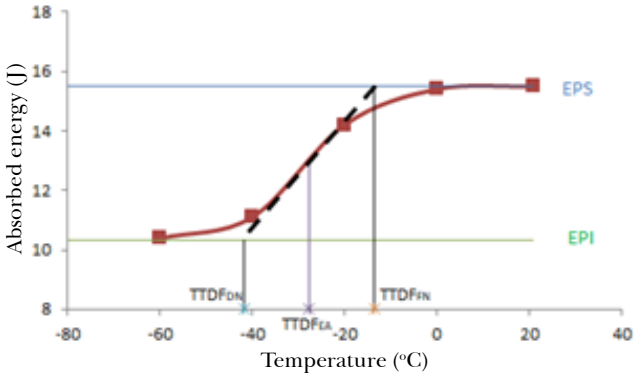

Table 4 - Results obtained by absorbed energy criterion using the hyperbolic tangent method.

Parameter	Value
$DBTT_{(EA)}$ (°C)	-27.73
$DBTT_{(BN)}$ (°C)	-41.83
$DBTT_{(ND)}$ (°C)	-13.64
EUP (J)	15.50
TUP (°C)	-13.64
ELP (J)	10.33
TLP (°C)	-41.83

3.2 Macroscopic and microscopic analysis

The macrographs of the fracture surfaces of the specimens are shown in **Fig. 7**. It is visually noticeable that, although there is a likelihood of a discrepancy occurring, as the test temperature decreases, there is a decrease in shear fracture, i.e. the percentage of ductile fracture area decreases, giving way to brittle fracture. With regard to the topic of lateral expansion, there was no evidence of this occurring, even in specimens at 0°C and room temperature, classified at first as mainly ductile.

It is possible to classify and quantify these fractures by means of qualitative and quantitative analyses of the percentage of ductile fracture, respectively, using the ASTM E23 standard as a reference [16]. However, other studies [30-31] have shown that the values obtained when each of the different definitions for determining DBTT is adopted are different from each other. As a result, measuring DBTT values based on qualitative and

quantitative ductile fracture percentage criteria, despite also being results of the evaluation of the fracture faces of the test specimens, are certainly susceptible to incredulity.

Table 5 shows the percentages obtained by both criteria (qualitative and quantitative) and confirms the significant differences between them. Also, when the values for the percentage of ductile fracture of the surfaces are compared with the values obtained using the absorbed energy criterion, incompatibility is observed, despite the fact that they are achieved by different criteria. From the evaluation of the fracture faces, it is clear that there is a risk of disparity between the results, since the appearance of the fracture faces of different materials can be similar.

Fig. 7 - Macroscopy of the fracture face of Charpy impact test specimens at temperatures: (a) ambient; (b) 0°C; (c) -20°C; (d) -40°C; (e) -60°C (5X magnification).

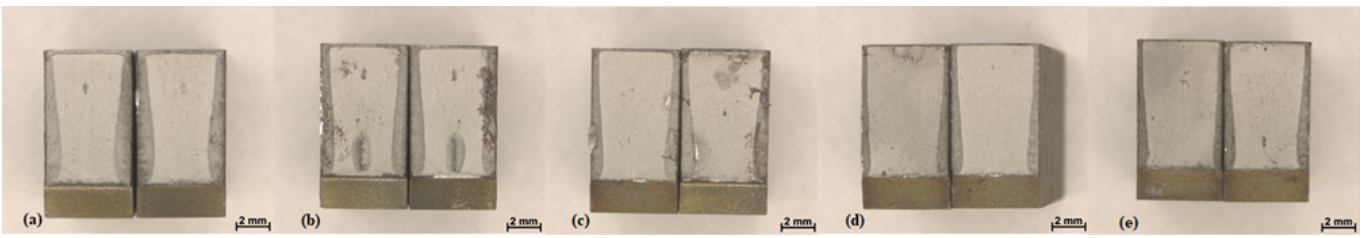

Table 5 - Percentage of ductile fracture using the ASTM E23 standard as a reference.

Temperature (°C)	% Qualitative	% Quantitative
Room	50.00	34.73
0.0	50.00	32.21
-20.0	40.00	26.28
-40.0	40.00	25.29
-60.0	20.00	9.68

Therefore, in order to study the fracture micromechanism in greater detail and obtain greater reliability, microscopic analyses of the fracture faces were conducted via SEM. The aim of this analysis was to confirm the fracture micromechanism observed through macroscopy on the fracture faces of the specimens tested under Charpy impact at the different temperatures.

The SEM micrographs of the fracture surfaces of the specimens after the tests, carried out at room temperature, -20°C and -60°C, are shown in **Fig. 8** to **Fig. 10**, respectively. The figures show the surfaces subdivided into three regions of the specimens (top, middle and bottom), noting that in the left column the magnification is 30X or 50X and in the right column the magnification is 1000X or 2000X.

It is noticeable in **Fig. 8** that the surface contains a typical feature of a predominantly ductile fracture—roughness. Another characteristic of a highly ductile fracture, dimples, are also evident on the surface. These micromechanisms are supported by the curve of absorbed energy as a function of temperature adjusted by the hyperbolic tangent method, as this would show a mainly ductile fracture.

The specimens tested at -20°C are the ones with a temperature closest to $DBTT_{EA}$ and whose fracture faces were considered mixed (as having brittle and ductile fractures), which is in line with the behavior expected of the material at the transition temperature. As shown in **Fig. 9**, where both cleavage fracture and shear fracture were considered to be present.

Fig. 10 shows micrographs of the fracture surface of the specimens after testing at -60°C. The surface characteristics show a predominant fracture resulting from the cleavage micro-mechanism, which is consistent with the region of this temperature in the curve of absorbed energy as a function of temperature adjusted by the hyperbolic tangent method.

3.3 Effect of chemical composition

A comparative analysis between the material under study and another type of tempered and quenched steel, the AISI 4340 steel studied elsewhere [32], and corroborated the prescribed effect of chemical composition on the impact fracture energy curve. In other studies, this effect is also consistent with the behavior of other steels [33]. The DBTT of AISI 4340 steel occurred at 0°C determined at 21.0 J. Its Mn, C, P and S content in % weight is 0.72, 0.42, 0.015 and 0.008, respectively [32]. As shown in **Table 1**, UHH-Q&T has a higher Mn content, inducing a rise in absorbed energy, but the higher C content encourages greater vigor instead. Therefore, partly due to this relationship, the absorbed energy of the material under study is lower (12.92 J).

3.4 Correlation between Charpy impact and fracture toughness

Both the Charpy test and the Pellini drop-weight test are still widely applied to structural materials. ASTM has standardized both tests, as well as a number of related approaches [16, 34-35]. Although these tests lack the mathematical rigor and predictive capabilities of fracture mechanics methods, these approaches provide an excellent qualitative indication of material toughness. The advantage of these qualitative methods is that they are less expensive and easier to perform than fracture mechanics tests [16, 34].

Fig. 8 - SEM images of details of the fracture face of the specimen tested by Charpy impact at room temperature.

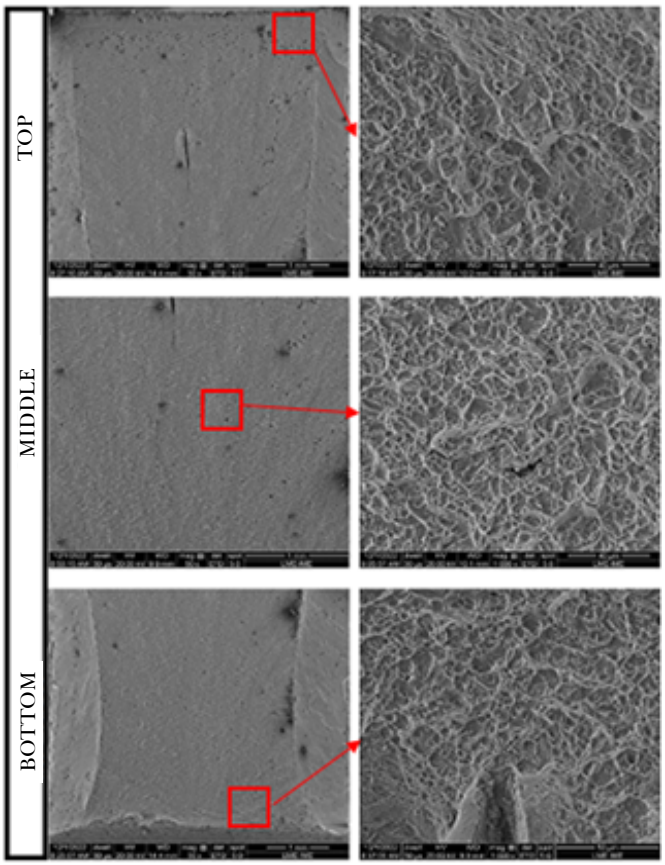

Some researchers [36-38] have correlated the absorbed energy obtained in the Charpy test with fracture toughness parameters such as K_{Ic}. Some of these empirical correlations work reasonably well, and the shipbuilding industry uses the Pellini drop-weight test to qualify steels for ship hulls. However, there are important differences between these tests and fracture mechanics tests that prevent simple relationships between qualitative and quantitative measures of toughness.

These differences include the fact that Charpy and drop-weight test specimens have an initial notch, while fracture mechanics specimens have significant fatigue cracks [16, 34].

When the material available does not allow Charpy impact specimens to be made to the standard size (10 x 10 x 55 mm), smaller ones can be used, as was the case in this study, but the results obtained with different specimen sizes cannot be compared directly. When Charpy specimens with dimensions smaller than the standard, i.e. sub-size, are required or specified, they can be selected in accordance with Annex *A3–Additional Impact Test Specimen Configurations* of the ASTM E23 standard [16].

Fig. 9 - SEM images of details of the fracture face of the specimen tested by Charpy impact at -20°C.

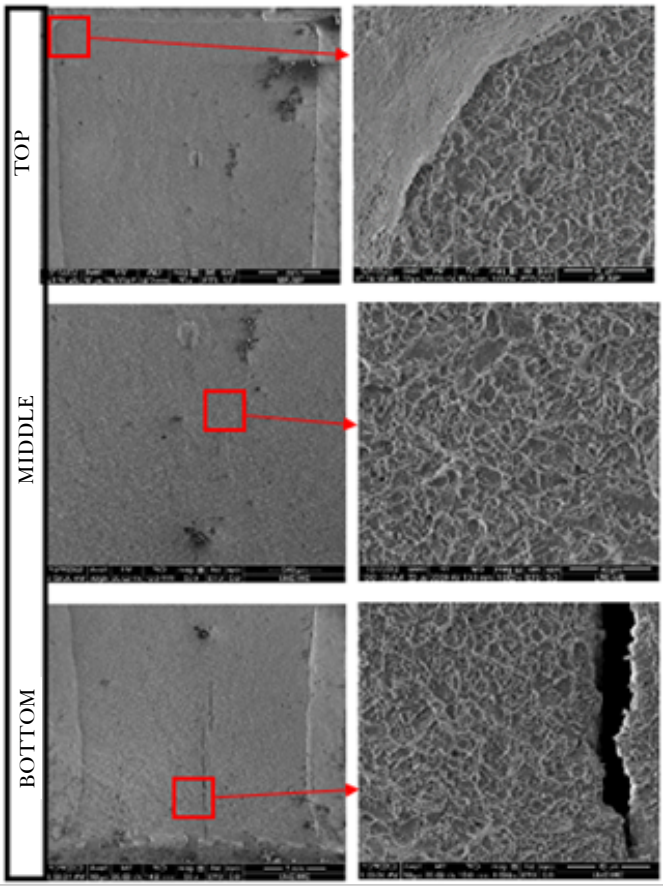

Varying, increasing or decreasing the thickness and/or width of the specimen tends to modulate the volume of the metal subjected to distortion and, as a result, also tends to change the energy absorbed.

However, any increase in size, particularly in thickness, also tends to increase the degree of restriction and, by tending to induce brittle fracture, can decrease the energy absorbed [16].

Fig. 10 - SEM images of details of the fracture face of the specimen tested by Charpy impact at -60°C.

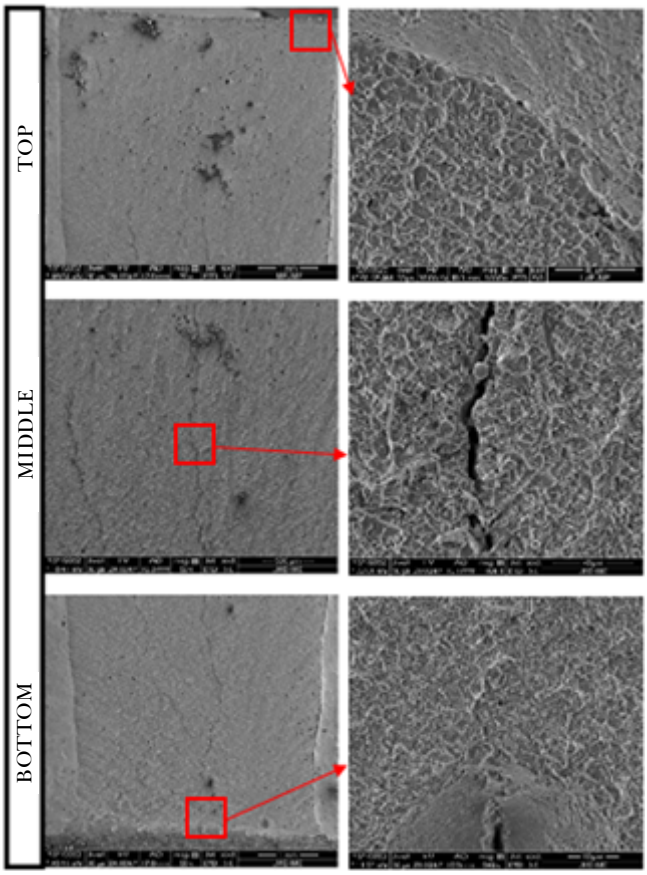

A general correlation between the absorbed energy values obtained with specimens of different sizes or shapes is not feasible, but limited correlations can be established for specification purposes based on special studies of specific materials and specimens [16].

4. Conclusions

From the methodology used in the Charpy impact test combined with fractographic analysis, it was possible to obtain a better understanding of impact tests and material behavior analysis, thus enabling the verification of energy absorbed as a function of temperature for specimens tested at different temperatures. It can be said that this is the most appropriate method for determining the DBTT of UHH-Q&T steel.

The tests showed that it is possible to obtain mechanical properties in terms of the toughness of a material by means of impact. Through this development, it was realized that temperature influences the toughness of the material, obtaining, for the specimen tested, a predominantly brittle structure at low temperatures and a dominant ductile structure at room temperature, certified by micrography. In this way, the correct material to use at different temperatures can be determined.

By evaluating the fracture faces of the specimens by SEM, it was possible to see that in the specimens tested in the transition zone there are regions where, by visual evaluation, it was considered that there was cleavage fracture, but in these there are also regions with alveoli resulting from plastic deformation of the material, typical of ductile fracture. The qualitative and quantitative criteria are therefore doubtful.

The results show that the DBTT based on 12.92 J of absorbed energy is -27.73°C. In addition, the temperature at which the zero ductility transition occurs is -41.83°C and the zero brittleness transition occurs at -13.64°C.

Acknowledgements

The authors would like to thank SSAB Special Steels for supplying the base material, the Mechanical Testing and Scanning Electron Microscopy Laboratories of the Materials Engineering Section of the Instituto Militar de Engenharia (IME) and the Materials Characterization Laboratory (LACAM) of the Universidade Federal do Pará (UFPA) for providing testing and microstructural characterization facilities for this work.

References

[1] U.S. **Military Specification, MIL-DTL-46100E (MR). Armor Plate, Steel, Wrought, High-Hardness**. U.S. Army Research Laboratory, APG, MD, 9 July 2008.

[2] RAPACKI, E.; FRANK, K.; LEAVY, B.; KEELE, M.; PRIFTI, J. **Armor** steel hardness influence on kinetic energy penetration proceedings. In: INTERNATIONAL SYMPOSIUM ON BALLISTICS, 15., Jerusalem, 1995.

[3] SSAB. Armor: The steel you want between you and risk. Sweden: SSAB, 2017.
[4] BACKMAN, M. E.; GOLDSMITH, W. The mechanics of penetration of projectiles into targets. **International Journal of Engineering Science**, [s. l.], v. 16, p. 1-99. 1978.
[5] PEREIRA, L. C., BLAS, J. C. G., GRIZA, S., DARWISH, F. A. I. Use of instrumented Charpy testing on the fracture toughness characterization of metallic materials. **Tecnologia em Metalurgia, Materiais e Mineração**, [s. l.], v. 18, p. 1-11. 2021.
[6] TANAKA, M.; UMEKAWA, S. On the breaking behaviour in Charpy impact bending tests. In: JAPAN CONGRESS FOR TESTING MATERIALS, 1., Kyoto, 1958.
[7] ONO, S. Micro-time structure of impact fracture concerning Charpy test. In: JAPAN CONGRESS FOR TESTING MATERIALS, 1., Kyoto, 1958.
[8] TAGAWA, T.; KAYAMORI, Y.; HIRA, H. Statistical scatter of fracture toughness in the ductile–brittle transition of a structural steel. **Eng. Fract. Mech**., v. 77, n. 16, p. 3077-3086, 2010.
[9] CHEN, S. L.; HU, J.; ZHANG, X. D. et al. High ductility and toughness of a micro-duplex medium-Mn steel in a large temperature range from -196°C to 200°C. **Journal of Iron and Steel Research International**, [s. l.], v. 22, p. 1126-1130, 2015.
[10] GOPALAN, A.; SAMAL, M. K.; CHAKRAVARTTY, J. K. Fracture toughness evaluation of 20MnMoNi55 pressure vessel steel in the ductile to brittle transition regime: Experiment & numerical simulations. **J. Nucl. Mater**., [s. l.], v. 465, p. 424-432, 2015.
[11] CHAO, Y. J.; WARD, J. D.; SANDS, R. G. Charpy impact energy, fracture toughness and ductile–brittle transition temperature of dual-phase 590 steel. **Mater. Design**, [s. l.], v. 28, p. 551-557, 2007.
[12] TANGUY, B.; BESSON, J.; PIQUES, R.; PINEAU, A. Ductile to brittle transition of an A508 steel characterized by Charpy impact test: Part I: Experimental results. **Eng. Fract. Mech**., [s. l.], v. 72, p. 49-72, 2005.
[13] HAUŠILD, P.; NEDBAL, I.; BERDIN, C.; PRIOUL, C. The influence of ductile tearing on fracture energy in the ductile-to-brittle transition temperature range. **Materials Science and Engineering: A**, [s. l.], v. 335, p. 164-174, 2002.
[14] ROSENFIELD, A. R.; SHETTY, D. K.; SKIDMORE, A. J. Fractographic observations of cleavage initiation in the ductile-brittle transition region of a reactor-pressure-vessel steel. **Metallurgical Transactions A**, v. 14, p. 1934-1937, 1983.
[15] TAKASHIMA, Y.; MINAMI, F. Prediction of Charpy absorbed energy of steel for welded structure in ductile--to-brittle fracture transition temperature range. **Quarterly Journal of the Japan Welding Society**, v. 38, p. 103-107, 2020.
[16] AMERICAN SOCIETY FOR TESTING AND MATERIALS. **ASTM E23**: Standard test methods for notched bar impact testing of metallic materials. U.S.: American Society for Testing and Materials, 2018.
[17] ZHANG, X.; QU, Y.; LI, R. Low temperature impact toughness and fracture analysis of EN-GJS-400-18-LT ductile iron under instrumented impact load. **Journal of Iron and Steel Research International**, [s. l.], v. 22, p. 864-869, 2015.
[18] SAMAL, M. K.; CHAKRAVARTTY, J. K.; SEIDENFUSS, M.; ROOS, E. Evaluation of fracture toughness and its scatter in the DBTT region of different types of pressure vessel steels. **Engineering Failure Analysis**, v. 18, p. 172-185, 2011.
[19] DIETER, G. E. **Mechanical Metallurgy**. 2. ed. New York: McGraw-Hill Book Company, 1981.
[20] LEACH, P. W.; WOODWARD, R. L. The influence of microstructural anisotropy on the mode of plate failure during projectile impact. **J. Mat. Sci**., [s. l.], v. 20, p. 854-858, 1985.
[21] MANGANELLO, S. J.; ABBOTT, K. H. Metallurgical factors affecting the ballistic behaviour of steel targets. **J. Mat**., [s. l.], v. 7, p. 231-239, 1972.
[22] SHOWALTER, D. D. et al. STANDARD, Australian Defence. DEF (AUST) 8030. Rolled Armour Plate, Steel (3-35 mm). **Army Research Laboratory,** Adelphi, 2005.
[23] HERZIG, N ; MEYER, L. W.; PURSCHE, F., HUSING, K. Relation between dynamic strength and toughness properties and the behavior under blast conditions of high strength steels. In: INTERNATIONAL SYMPOSIUM ON IMPACT ENGINEERING, 7., 2010. **Anais** […]. Warsaw: MABS, 2010. p. 278-284.
[24] BRITISH STANDARD. BS EN 10029: Hot-rolled steel plates 3 mm thick or above – tolerances on dimensions and shape. UK: British Standard, 2010.
[25] BRITISH STANDARD. **BS EN 10163-2**: Delivery requirements for surface condition of hot-rolled steel plates, wide flats and sections — Part 2: Plate and wide flats. UK: British Standard, 2004.

[26] SSAB. **General product information strenx, hardox, armox and toolbox – UK**. [s. l.]: SSAB, 2018.
[27] ERICKSONKIRK, M.; SHAIKH, A.; ERICKSONKIRK, M. Insights and observations arising from curve-fitting the Charpy V-notch and tensile data contained within the United States' light water reactor surveillance database. ASME 2008 PRESSURE VESSELS AND PIPING CONFERENCE. 2008. Chicago, 2008. p. 389-396.
[28] AMERICAN SOCIETY FOR TESTING AND MATERIALS. **ASTM E2142**: Standard test methods for rating and classifying inclusions in steel using the scanning electron microscope. West Conshohocken: American Society for Testing and Materials, 2015.
[29] FOLCH, L.; BURDEKIN, F. M. Application of coupled brittle-ductile model to study correlation between Charpy energy and fracture toughness values. **Eng. Fract. Mech**., [s. l.], v. 63, p. 57-80, 1999.
[30] ZHAO, Y. J.; SU, Y. M.; LIU, M.; HU, Z. L.; TANG, P. Ductile-to-brittle transition and impact fracture behavior of 3Mn–Si–Ni low carbon martensitic steel. **Strength of Materials**, [s. l.], v. 51, p. 291-299, 2019.
[31] TAKASHIMA, Y.; ITO, Y.; LU, F.; MINAMI, F. Fracture toughness evaluation for dissimilar steel joints by Charpy impact test. **Welding in the World**, [s. l.], v. 63, p. 1243-1254, 2019.
[32] DUARTE, A. S. **Metodologia básica para a produção de materiais de referência para a calibração indireta de máquinas pendulares de impacto Charpy**. 2006. Dissertação (Mestrado em Engenharia de Materiais) – Universidade Federal de Ouro Preto, Ouro Preto, 2006.
[33] ROE, G. J.; BRAMFITT, B. L. **Notch toughness of steels. ASM International, Metals Handbook**. Materials Park: ASM Handbook, 1990.
[34] AMERICAN SOCIETY FOR TESTING AND MATERIALS. **ASTM E208**: Standard test method for conducting drop-weight test to determine nil-ductility transition temperature of ferritic steels. West Conshohocken: American Society for Testing and Materials, 2020.
[35] AMERICAN SOCIETY FOR TESTING AND MATERIALS. **ASTM E436-03**: Standard test method for drop-weight tear tests of ferritic steels. West Conshohocken: American Society for Testing and Materials, 2021.
[36] TEERI, T.; KUOKKALA, V.-T.; SIITONEN, P.; KIVIKYTÖ-REPONEN, P.; LIIMATAINEN, J. Impact wear in mineral crushing. **Proceedings of the Estonian Academy of Sciences Engineering**, [s. l.], v. 12, p. 408-418, 2006.
[37] ZAMBRANO, O. A. A review on the effect of impact toughness and fracture toughness on impact-abrasion wear. **Journal of Materials Engineering and Performance**, Materials Park, v. 30, p. 7101-7116, 2021.
[38] WALLIN, K. A simple theoretical Charpy-V-K correlation for irradiation embrittlement. In: MARRIOT, D. L.; MAGER, T. R.; BAMFORD, W. H. (Eds.). **Innovative Approaches to Irradiation Damage and Fracture Analysis**. v. 170. New York: ASME – American Society of Mechanical Engineers, 1989. p. 93-100.

VOL.40 Nº3 2023
https://doi.org/10.22491/rmct.v40i3.11418.en

Study of the composition, structure, and effect of water absorption on the wall of bovine hooves from the Brazilian Northeast region

Wendell Bruno Almeida Bezerra[1]*, Ulisses Oliveira Costa[1], Fabio da Costa Garcia Filho[1], Sergio Neves Monteiro[1]
[1]Instituto Militar de Engenharia (IME).
Praça General Tibúrcio, 80, 22290-270, Praia Vermelha, Rio de Janeiro, RJ, Brasil,
***wendellbez@ime.eb.br**

ABSTRACT: Over thousands of years natural materials have evolved to complex and multifunctional hierarchical structures. An example of this, bovine hooves are keratinous materials differentiated from other types of hooves whose structure and composition are not yet as well-known as that of equine hooves. Thus, the present work aimed to investigate the influence of absorbed water on the structure and composition of bovine hooves from the Northeast region of Brazil. The hulls were evaluated using X-ray diffraction analysis (XRD), Fourier transform infrared spectroscopy (FTIR) and scanning electron microscopy (SEM). The effect of water on the amorphous keratin matrix of the hooves can be observed through DRX and FTIR analyses, as well as identifying different zones and dimensions of the tubules in the structure through SEM images. The results present a starting point for the correlation between structure and impact absorption mechanisms in these materials.

***KEYWORDS:** Keratin. Bovine hooves. Water absorption. Composition. Structure.*

RESUMO: Ao longo de milhares de anos, os materiais naturais evoluíram, desenvolvendo estruturas hierárquicas complexas e multifuncionais. Um exemplo disso, os cascos bovinos, são materiais queratinosos diferenciados de outros tipos de cascos cuja estrutura e composição ainda não são tão conhecidas como a dos cascos equinos. Dessa forma, o presente trabalho se propôs a investigar a influência da água absorvida na estrutura e composição de cascos bovinos oriundos da região Nordeste do Brasil. Os cascos foram avaliados através de análises de difração de raios X (DRX), espectroscopia no infravermelho por transformada de Fourier (FTIR) e microscopia eletrônica de varredura (MEV). Pode-se observar o efeito da água na matriz de queratina amorfa dos cascos através das análises de DRX e FTIR, bem como identificar diferentes zonas e dimensões dos túbulos na estrutura através das imagens de MEV. Os resultados apresentam um ponto de partida para a correlação entre a estrutura e os mecanismos de absorção de impacto nesses materiais.

***PALAVRAS-CHAVE:** Queratina. Cascos bovinos. Absorção de água. Composição. Estrutura.*

1. Introduction

Many biological materials have evolved in such a way as to have multifunctional structures and the ability to absorb considerable amounts of energy without fracturing. These include functions such as protection (*e.g.* mollusc shells, bones), defense and aggression (*e.g.* claws, teeth, fangs, horns and antlers), support (*e.g.* bones, mollusc shells and hooves) and chewing (*e.g.* teeth) [1]. These materials are made up of different structural components with different chemical and physical characteristics [2]. Notable among these are keratin-based components [3].

Keratin is made up of polypeptide chains. This component has variants that can be found both in mammals, constituting hair, nails, hooves, horns and the epidermal layer of the skin, and in reptiles and birds, in their claws, scales, feathers and beaks [4]. Initially, some of these materials attracted the most interest because of their ability to absorb a considerable amount of energy and resist impact (*e.g.* hooves and horns) [1, 3-5].

Keratins can be classified as types α and β. Both have a matrix-filament type structure, observed in each type in the form of: intermediate filaments (IFs) 7 nm in diameter in the case of α-keratin, and filaments 3 nm in diameter in β-keratin, both embedded in an amorphous keratin matrix. [4]. In this sense, water plays a fundamental role in the mechanical properties of structural biological materials. Similarly, the mechanical properties of α-keratin and β-keratin are influenced by water content.

In general, the presence of water defines the structural characteristics and physical properties of proteins and organic substances, acting as a plasticizer in biological materials, increasing their ductility and decreasing their toughness. In this way, without water, biological materials lose their original mechanical properties and become more fragile [2]. The same occurs with keratin: as humidity increases, stiffness and strength decrease, while tensile strength increases [4].

Through X-ray diffraction and experimental studies, previous works have revealed that matrix proteins can be considered to be sensitive to water, while IFs are crystalline and are not mechanically affected by humidity [6-10]. In general, this can be extended to keratinous materials, since IFs do not change in the different rigid keratins of mammals [6]. Different models have been proposed to explain how the interaction between water molecules and matrix proteins occurs.

According to the proposed models:

a. Water can act as a swelling agent, forming a cross-link with the chains, resulting in a reduction in the interaction between the chains and an increase in the intermolecular space [10];
b. Water can break/replace secondary bonds present between glycine/tyrosine-rich proteins in the matrix phase, such as hydrogen bonds, resulting in greater protein mobility [7,9];
c. Water can form a three-dimensional keratin-water molecule network that acts as a plasticizer, resulting in less rigidity and greater segmental mobility of the matrix's molecular structure [6,10].

Keratinous biological materials, which have different structures with keratin as their main component, have their properties directly linked to the sensitivity of this component. When dehydrated, these materials lose their original mechanical properties and become more fragile. Therefore, in order to correctly assess the mechanical properties of biological materials, it is extremely important to take into account the degree of hydration [2].

However, before we can apply biological structures to the manufacture of bioinspired materials, we need a thorough understanding of the relationship between structure and properties in these complex materials. Several studies have focused on this paradigm, in particular equine hooves and American wild sheep horns [5, 11,12]. In addition to these, some materials from other species have had their structures and properties analyzed, such as bovine hooves [13-16], but little focus is applied to the relationship between structure and dynamic behavior.

Based on the literature, the analysis of these characteristics in keratinous biological materials is proving useful in the development of bio-inspired systems and structures which are expected to perform better with subsequent improvements in materials processing and production technology.

The aim of this work is to study the relationship between composition, structure and the effect of water on keratinous biological materials, such as bovine hooves, in order to provide a starting point for the development of new bioinspired impact-resistant materials.

2. Materials and methods

The hooves of bovine species from northeastern Brazil were studied to analyze their composition and structure. The hooves of different animals were obtained from the municipal slaughterhouse in the city of Juazeiro do Norte, Ceará. The hooves were washed and then left to dry at room temperature, without specific humidity control. Figure 1 shows the bovine hoof with its respective anatomical regions, taken into account when preparing the samples.

Fig. 1 - Anatomical positions of the hooves and sampling regions. Source: Author.

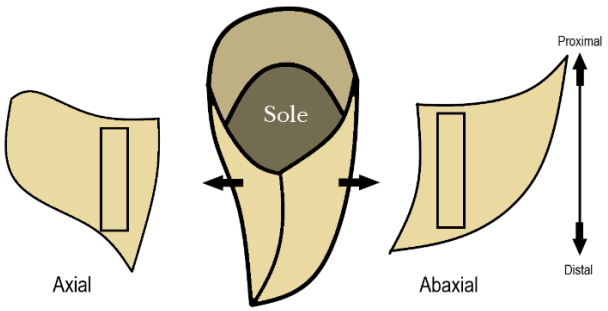

2.1 Water absorption

In order to assess the time required for the hooves to fully hydrate after immersion, water absorption tests were carried out. As there is no specific standard for natural materials, the tests were based on ASTM D570-98 (2018). Five (5) samples were prepared from two different regions of the abaxial wall of bovine hooves, thus characterizing two groups: abaxial-proximal (AB-P) and abaxial-distal (AB-D). The samples were weighed and immersed in deionized water and re-weighed after immersion periods of: five (5min), ten (10min), twenty (20min) and thirty (30min) minutes, and one (1h), two (2h), three (3h), four (4h), twenty-four (24h), forty-eight (48h), seventy-two (72h) and ninety-six (96h) hours. After the final immersion time, the samples were separated, weighed and their moisture content assessed, as described in previous studies [14,16]. The samples were then placed in an oven at 70ºC for a period of seven (7) days. The moisture content (MC %) can be determined using Equation 1:

$$MC\ \% = \frac{wet\ mass - dry\ mass}{wet\ mass} \times 100\% \qquad (1)$$

2.1 X-ray diffraction (XRD)

The samples were prepared from two different regions of the abaxial wall, namely abaxial-proximal (AB-P) and abaxial-distal (AB-D). One sample from each group was subjected to each of the two different hydration conditions: conditioned at room temperature (AD) and fully hydrated (100). In addition, the inner (IW) and outer (EW) wall surfaces were evaluated on the AB-D sample. Thus, the samples were named according to Table 1.

The analyses were carried out on an X-ray diffractometer, model X'Pert Pro Panalytical, available from the Military Engineering Institute (IME), using a CoKα radiation source (1.790307 Å). The parameters used were: 40 kV voltage, 40 mA current, 0.04 degree step. The spectra were obtained for values of 2θ from 5 to 50º, based on the literature found [18,19].

Using OriginPro 2019 software, the data obtained was subjected to noise removal using the Savitzky-Golay method, and the curves were adjusted with deconvolution of the halos in order to determine the position of the peaks more precisely.

Tab. 1 - Nomenclature of samples for XRD analysis under the different conditions studied

Region	Hydration	Surface	Nomenclature
Abaxial-distal (AB-D)	AD	External (EW)	**AB-D-AD-EW**
		Internal (IW)	**AB-D-AD-IW**
	100	External (EW)	**AB-D-100-EW**
		Internal (IW)	**AB-D-100-IW**
Abaxial-proximal (AB-P)	AD	External	**AB-P-AD**
	100	-	**AB-P-100**

Source: Author

2.2 Fourier transform infrared spectroscopy (FTIR)

In order to better understand the effect of hydration on the chemical structure of the hoof components, Fourier transform infrared spectroscopy (FTIR) analyses were carried out with different sample conditions. These were prepared from two different regions of the abaxial wall, called abaxial-proximal (AB-P) and abaxial-distal (AB-D). From each group of regions, two hydration conditions were prepared: drying at room temperature (sa) and fully hydrated (100).

The analyses were carried out on a PerkinElmer Frontier FT-IR/FIR device, in transmittance mode with KBr pellets, with a resolution of 4 cm^{-1}, using a wave number range of 4,000 to 400 cm^{-1}. The transmittance mode using KBr pellets was chosen in order to compare the spectra obtained with those reported for other keratinous materials and hoof keratin membranes [18,19].

2.3 Scanning electron microscopy (SEM)

In order to characterize the surface morphology of the hoof wall and its internal structure, scanning electron microscopy (SEM) analyses were carried out. Since the materials are not electrically conductive, they were subjected to a metallic surface coating using LEICA equipment, model EM ACE600, and the analyses were carried out on FEI equipment, model Quanta FEG 250, both available at the IME.

3. Results and discussion

3.1 Water absorption

Moisture content is known to be one of the factors affecting the mechanical properties of structural biological materials, especially hoof walls [14]. Therefore, in order to speed up the procedure for preparing samples for future work, water absorption tests were carried out on two different regions of the abaxial wall of bovine hooves.

Figure 2 shows the mean percentage increases in weight observed in the samples after the proposed immersion time intervals. Accelerated absorption was observed in the first few minutes with a subsequent reduction in the absorption rate, due to water saturation in the structure of the material [20]. Similar behavior has been observed in other structural biological materials [9,21]. In addition, it is possible to observe an asymptotic tendency of the points to plateau after three days (4,320 min) of immersion. In the case of oryx horns, Kitchener (1987) reports the total hydration of the material, represented by the plateau, after 3 days, while for equine hooves, complete hydration occurs after 5 days [9].

Despite the apparent trend for the abaxial-proximal wall to absorb more on average, no significant differences were observed between the two regions. After four days of immersion (5,760 min), mean values of 23.58 ± 2.37% were observed for the abaxial-proximal region (AB-P) and 21.28 ± 1.00% for the abaxial-distal region (AB-D).

Fig. 2 - Mean water absorption (%) for each region of the abaxial wall of bovine hooves: proximal and distal.

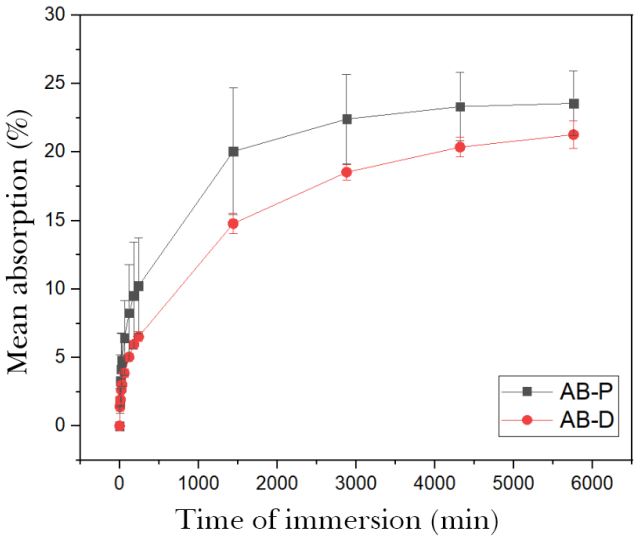

Previous works have studied the effect of atmospheric relative humidity on the moisture content of different hooves, especially single-digit hooves such as those of horses and donkeys [9,22]. In both cases, the curves of moisture content versus atmospheric relative humidity show an exponential increase in the level of hoof hydration with the increase in ambient relative humidity.

Baillie and colleagues (2000) proposed that the best way to simulate the levels of hydration present in hooves *in vivo* would be through immersion in an aqueous medium. In this way, it is expected that, due to the presence of tubules in the internal structure of the wall, there will be a direct effect of capillarity on the hydration obtained. However, in equine hooves, the formation of hydration gradients (*i.e.* greater hydration in the distal region) expected for this case was not observed [20]. On the contrary, a higher rate

of dehydration was observed in the distal region due to the presence of openings in the tubules.

The mean values and the respective standard deviations of the moisture contents obtained for the samples from the two groups studied are shown in the Table 2. In the literature, values can be found for bovine hooves ranging from 3.11 to 35.50 %w/w H_2O, depending on the hydration or dehydration conditions used [14,16]. The values found in this study are very close to those reported by Wang et al. (2020), of 28.05 and 27.15%. In addition, a significant difference (*i.e.* confidence interval = 95%) was observed in the moisture content values of the two regions studied, which is similar to that reported for equine hooves [9]. The moisture content of hooves dried at ambient humidity (AD) was 10.03 and 11.32% for the abaxial-distal (AB-D) and abaxial--proximal (AB-P) regions, respectively.

Tab. 2 - Mean moisture content of samples after hydration

Sample	Mean moisture content (%w/w H2O)	Standard deviation
AB-P-100	25.05	1.50
AB-D-100	22.52	0.80

3.2 X-ray diffraction (XRD)

The physical structure of keratins has been studied for a long time and is widely reported in the literature [4,8]. Through X-ray diffraction it is possible to identify three characteristic patterns: α pattern, β pattern and feather pattern, in addition to the amorphous pattern. In most mammals, the keratin found shows the α pattern [4], exhibiting two typical spacings: one related to the distance between the molecules that make up the α-helix, of 9.80 Å, and the other related to the step between the two molecules of the α-helix, of 5.15 Å [23].

The diffractograms obtained for the samples of the abaxial wall of the bovine hoof, from the proximal and distal regions under the two hydration conditions, are shown in Figure 3. By fitting the curves, it was possible to observe two characteristic halos in the different samples. The presence of halos rather than peaks is associated both with the fact that the hoof wall has an amorphous keratin matrix and with the fact that the intermediate filaments (IFs) have a crystallinity order at the nanometric level.

The first halo was found at Bragg angles (2θ) ranging from 10.28 and 10.93º. From these values, the interplanar spacings could be identified, as shown in 3, resulting in a mean spacing of 9.60 ± 0.24 Å. No significant variation was identified between the structure of the inner (AB_D_PI_AD) and outer (AB_D_PE_AD) hoof walls, or between the distal and proximal regions. The second halo was found at Bragg angles (2θ) of 22.59 to 24.79º. The spacings related to these angles are shown in Table 3. A mean spacing of 4.33 ± 0.18 Å was observed, very close to that reported for other keratinous materials, as shown in the same table.

Fig. 3 - Diffractograms obtained for samples from different regions of the hoof and under different hydration conditions.

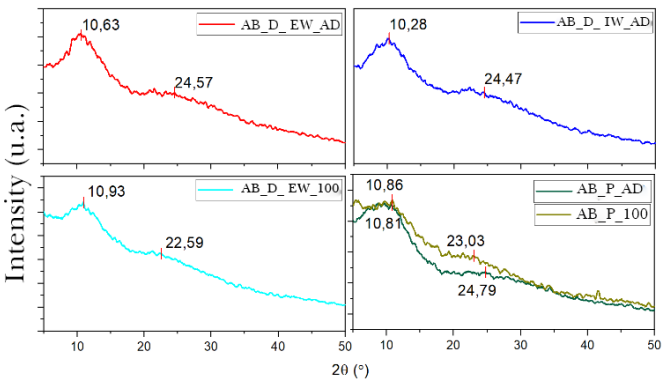

In order to avoid the inherent variability of natural materials, the same samples were evaluated in both hydration conditions, air-dried (AD) and immersed (100). In this way, comparing the two conditions allowed a better understanding of the influence of hydra-

tion on the physical structure of the hooves. There was a slight trend for the spacing related to the first halo to decrease: from 9.66 to 9.40 Å in the distal region (AB_D), and from 9.50 to 9.46 Å in the proximal region. Conversely, an upward trend was observed in the spacing related to the second halo: from 4.21 to 4.57 Å in the distal region (AB_D), and from 4.17 to 4.48 Å in the proximal region.

It is believed that these halos are directly associated with the spacings reported for the α-helix structure of keratin [8,19]. The findings reinforce the theory that water molecules can replace secondary bonds, such as hydrogen bonds, present between glycine/tyrosine--rich proteins in the matrix phase [7,9]. The introduction of water molecules into the structure generates an increase in the α-helix step distance, resulting in an increase in the spacings observed in both regions in the second halo, which suggests a decrease in the packing of the keratin crystal structure in the IFs.

Tab. 3 - Interplanar spacing of the samples analyzed in this study and keratinous materials reported in the literature

Material	d (Å)	Reference
AB_D_EW_AD	4.21	Present work (PW)
	9.66	
AB_D_IW_AD	4.22	
	9.99	
AB_D_EW_100	4.57	
	9.40	
AB_P_AD	4.17	
	9.50	
AB_P_100	4.48	
	9.46	
Wool	4.35	Wu and colleagues (2017)
Pure keratin	4.46	
Bovine hoof keratin	4.62	Valkov and colleagues (2020)
Hair keratin	4.48	Valkov and colleagues (2020)
Nail keratin	4.27	
α-keratin standard	5.15	Fraser, MacRae and Rogers (1972)
	9.80	

3.3 Fourier transform infrared spectroscopy (FTIR)

The composition of the bovine hoof wall and the effect of hydration on it can be assessed by studying the structure of the molecules that make up the material using infrared spectroscopy. The spectra obtained for the samples extracted from the proximal and distal regions of the abaxial hoof wall in the two hydration conditions, dry and hydrated, are shown in Figure 4. The presence of bands common to all the samples can be seen, with greater or lesser associated transmittance intensity. Of particular note are the bands found at frequencies between 3,600 and 3,200 cm^{-1}, related to N-H and O-H stretching vibrations; between 2,958 and 2,852 cm^{-1}, referring to C-H stretching vibrations; and 1,636 cm^{-1}, associated with the C=O and C-N stretching vibrations present in amides I [19].

Fig. 4 - Infrared spectra of the samples extracted from the different regions of the abaxial wall of bovine hooves, under the different hydration conditions studied

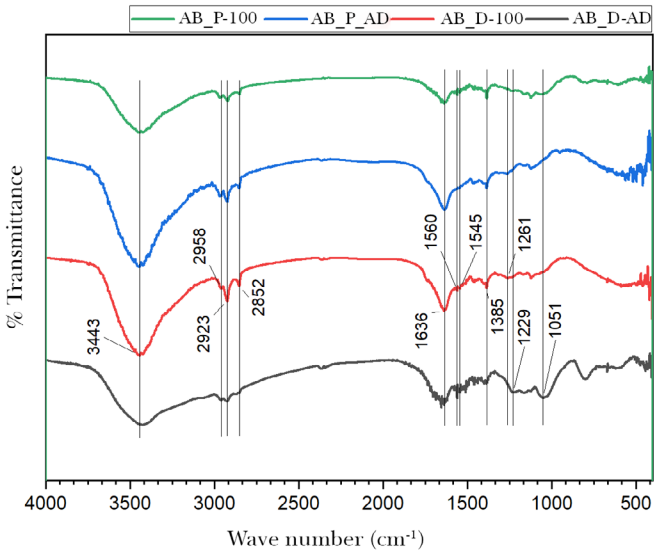

In addition, bands were observed at 1,560 and 1,545 cm^{-1} which are associated with the N-H angular deformation and C-N and C-C stretching vibration modes of amide II [19,24]. Table 4 summarizes the frequencies related to the main bands observed, the associated vibration modes and the values reported in the literature for other keratin structures.

The main difference observed between the proximal and distal regions of the hoof wall is related to the intensity of the band present at 1.051 cm^{-1}. This band is associated with the S-C bonds present in the cysteine that makes up keratin [24]. It is therefore believed that the greater intensity of the band observed in the distal region may be associated with a greater quantity of this amino acid in the structure.

In relation to the hydration condition, it was possible to observe a considerable increase in the intensity of the O-H band at 3.443 cm^{-1}, which is directly related to the level of humidity of the samples [19]. In addition, looking at the ratio between the intensities of the characteristic C=O and N-H bands, we can see a decrease in the intensity of the latter in relation to the former as the moisture content of the samples increases [25]. It is also possible to observe a change in the intensity ratio of the bands at 1,636 and 3,443 cm^{-1}, after the samples were hydrated. The higher intensity of the 1,636 cm^{-1} band observed in the hydrated samples may be associated with the more frequent occurrence of hydrogen bonds [26]. In the case of wild sheep horn [25], a variation in the position of the bands was also reported which was associated with an increase in moisture content, but this phenomenon was not observed in the present study.

Tab. 4 - Frequencies of the absorption bands observed in the samples studied and in other keratinous materials studied in the literature.

Material	Type of vibration	Wave number (cm^{-1})	Ref.
Bovine hoof wall	N-H and O-H stretching	3.600-3.200	Author
	C-H stretching	2.958-2.852	
	C=O and C-N stretching of amides I	1.636	
	N-H angular deformation and C-N and C-C stretching of amides II	1.560-1.530	
	Angular deformation of C-H and stretching of $-CH_3$	1.385	
	C-N stretching and C=O angular deformation of amides III	1.260-1.230	
	Characteristic of cysteine	1.070-1.040	
Goat hoof keratin	N-H and O-H stretching	3.650-3.250	[27]
	Characteristic of amides I	1.665-1.610	
	Characteristic of amides II	1.550-1.520	
Bovine hoof keratin	N-H stretching of amides A and O-H hydration	3.355-3.295	[19]
	C=O and C-N stretching of amides I	1.650	
	N-H angular deformation and C-N and C-C stretching of amides II	1.530	
	C-N stretching and C=O angular deformation of amides III	1.230	

Material	Type of vibration	Wave number (cm^{-1})	Ref.
Goat hoof wall	N-H and O-H stretching	3.400	[24]
	C-H stretching	2.960-2.870	
	CO stretching of amides I	1.655	
	CN stretching and NH angular deformation of amides II	1.540-1.520	
	Angular deformation of C-H and stretching of -CH3	1.387	
	CN stretching and NH angular deformation of amides III	1.238	
	Characteristic of -S-C	1.051	
	Characteristic of S=O	1.076	

3.4 Scanning electron microscopy (SEM)

In order to better understand the internal structure of the material, samples from different regions of the abaxial wall of bovine hooves were studied using scanning electron microscopy (SEM). The sanded samples from the distal, intermediate and abaxial regions of the hooves were observed and their micrographs are presented below.

Figure 5 shows micrographs taken at different magnifications of the cross-section of the proximal region of the bovine hoof wall. It is possible to see the opening of the tubule structure, some of which are selected and indicated by arrows. This structure is well known and has been reported in various keratinous materials, including bovine hooves [4,14,16,28-30]. One of the important factors to consider is the quantity of these components present in a given area, known as tubule density (mm^{-2}). The importance of this factor is mainly associated with the moisture content of the material, since the lower the tubule density, the greater the amount of intertubular material and, consequently, the higher the moisture content [28]. Figure 5 also shows tubules with various shapes, such as circular, oval and collapsed, similar to what has been reported in the literature [29].

Fig. 5 - Micrograph of the cross-section of the hoof wall in the proximal region, showing the presence of circular (C), oval (O), collapsed (Co) tubules and cracks in the intertubular material.

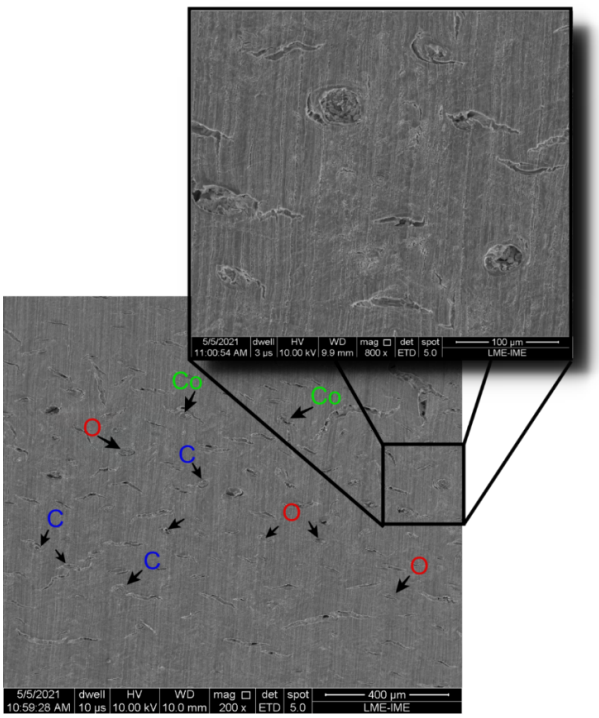

In all the regions studied, four distinct zones could be identified: lamellar, in the inner wall; internal; inter-

mediate, divided into two others with different tubule shapes and keratinocyte orientations; and external, with collapsed tubules. This division is well known and reported in the literature, but there is little information on the orientation of the keratinocytes in the intertubular matrix. Figure 6 shows the wall in total, with the lamellar zone highlighted by the square, 1.49 μm long in the distal region. The arrows indicate the orientation of the intertubular material, which could be identified by the direction of the cracks resulting from cutting the samples. In the case of equine hooves, the cracks follow the orientation of the contours of the keratin cells in the intertubular material [5]. This phenomenon also seems to occur in the bovine hooves studied here, as illustrated by the direction of the arrows. In this way, the internal zone can be identified, found immediately after the lamellar zone and characterized by the absence of tubules, followed by an intermediate region subdivided by the different orientations of the IFs [14,30]. The fourth and final zone is closest to the outer wall and appears to have mostly collapsed tubules.

Fig. 6 - Micrograph of the cross-section of the hoof wall in the distal region, showing the four zones observed along the wall and the orientation directions of the IFs in the intertubular material.

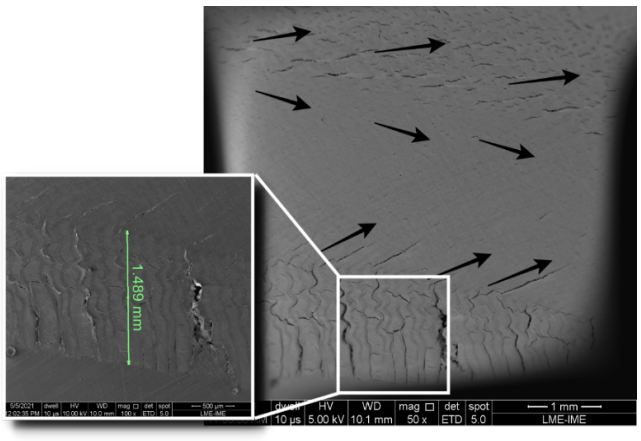

Figure 7 shows a micrograph of the cross-section of the hoof wall in the intermediate region, between the distal and proximal regions. It is possible to see two adjacent tubules with apparently different diameters, but elliptical in shape. Due to the rather irregular shape of the tubule on the left, it is believed that the central region of the tubule was torn off during sample preparation. The figure also shows the interface present in the intertubular material between what would be the two keratin cells. The proposed layered structure of the tubules can be seen in the delamination observed in the magnified region of Figure 7, which shows the diameter of the tubule (*i.e.* 5.65 μm). One can clearly see the separation of the layers adjacent to the tubule lumen, with a small bundle of intertubular material joining the layers.

Fig. 7 - Micrograph of the cross-section of the hoof wall in the intermediate region, showing the interface region between the keratin cells and the dimensions of one of the tubules observed in this region.

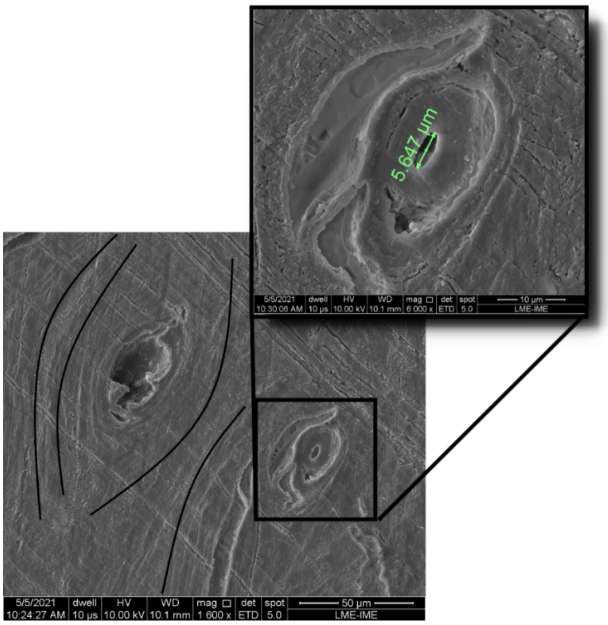

Similarly to what has been reported in previous studies for other hooves, a variation in the diameter of the tubules was identified along the hoof wall. Figure 8 shows a micrograph of a tubule observed in the distal region of the wall, with a diameter of 33.52 μm. In addition to the variation in diameter compared to the tubule in the intermediate region, a variation in shape can be seen, which is more spherical in the case of the distal region. These values are within the range of diameters found in the literature, which vary from 10 to 60 μm, if we consider the diameter of the outer layer of the tubule [14,29-31].

Figure 9 shows a micrograph of the region exactly adjacent to the one shown in 8. This figure shows the fibrils of the inner keratin cell layers, separated by the propagation of a crack. It is believed that the presence of this layered structure, with a well-defined interface between the cells, is related to a greater capacity for stress transfer and energy absorption [14]. This is due to the delamination, elongation and rupture mechanisms of the keratin fibrils present in the intertubular material [5].

Fig. 8 - Micrograph of a single tubule in cross-section of the wall in the distal region, showing the measured diameter

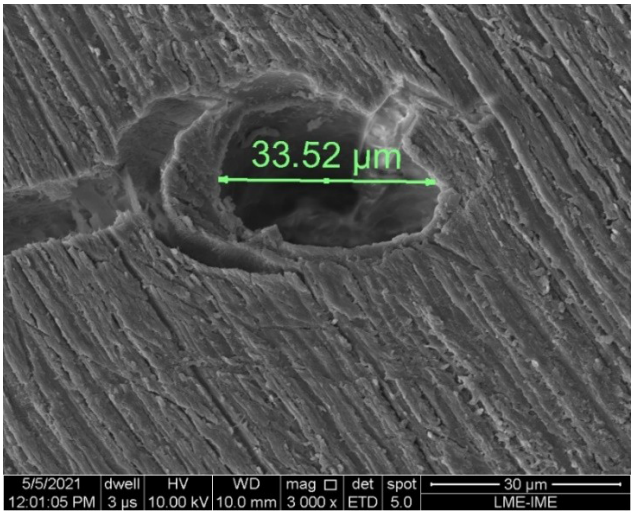

Fig. 9 - Micrograph of the cross-section of the hoof wall in the intermediate region, showing a crack and the IFs in the inner layers.

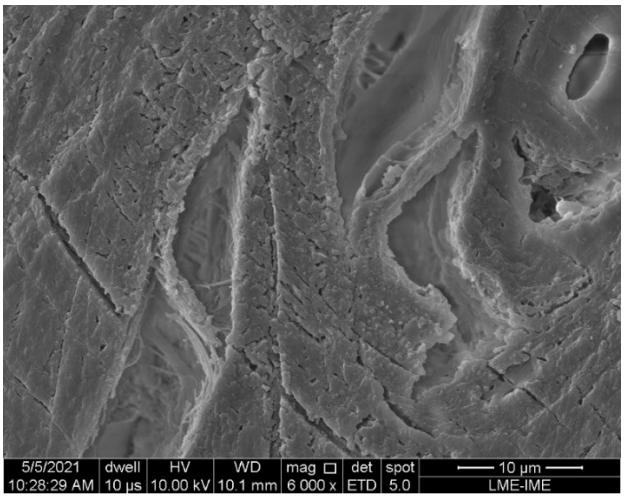

4. Conclusion

The samples extracted from the abaxial wall of bovine hooves had their structure and composition assessed using water absorption and moisture content tests, X-ray diffraction (XRD), Fourier transform infrared spectroscopy (FTIR) and scanning electron microscopy (SEM). The following conclusions were reached:

- In both regions studied (*i.e.* distal and proximal), the percentage by weight of water absorbed approaches a plateau after 3 days of immersion. This may indicate that an immersion interval of 4 days is sufficient to ensure total hydration of the hoof wall. In addition, no significant differences were observed in the water absorption of the different regions studied, but the moisture content after immersion was higher for the proximal region, similar to that reported for equine hooves.
- X-ray diffraction analysis showed the periodicity associated with the α-helix molecules of hoof keratin. Interpretation of the observed spacings showed that there was no significant difference between the outer and inner walls in the distal region, and there was a difference between the distal and proximal regions, with the spacing being smaller in the proximal region. Furthermore, in both regions, as the moisture content of the samples increased, there was a reduction in the observed spacings, which may be indicative of the interaction of water molecules with the α-helix structure of the keratin.
- Fourier transform infrared spectroscopy (FTIR) analysis enabled the identification of various absorption bands related to the chemical structures of amides A, I, II and III present in the α-keratins. In addition, varying the moisture content of the samples did not reveal any shift in the observed bands, only a change in the relative intensity of the bands.
- By observing the cross-section of the hoof wall in different areas, the internal structure of this material could be seen. Tubules of different shapes, from spherical to oval, and sizes, from 6 to 33 μm, could be identified in the structure. In addition,

four distinct zones were identified and compared to what has been reported in previous studies. It is believed that these zones, with IFs in different orientations, may contribute to greater energy absorption in the hoof wall.

Acknowledgments

The authors would like to thank IME for the resources used to carry out this work, as well as financing from CNPq, CAPES and FAPERJ.

References

[1] MCKITTRICK, J.; CHEN, P. Y.; TOMBOLATO, L.; NOVITSKAYA, E. E., TRIM, M. W.; HIRATA, G. A.; OLEVSKY, E. A.; HORSTEMEYER, M. F.; MEYERS, M. A. Energy Absorbent Natural Materials and Bioinspired Design Strategies: A Review. Materials Science Engineering C, v. 30, p. 331-342, 2010.
[2] MEYERS, M. A.; CHEN, P. Y. Biological Materials Science. Nova York: Cambridge University Press, 2014.
[3] MCKITTRICK, J.; CHEN, P. Y.; BODDE, S. G.; YANG, W.; NOVITSKAYA, E. E.; MEYERS, M. A. The Structure, Functions, and Mechanical Properties of Keratin. JOM, v. 64, p. 449-468, 2012.
[4] WANG, B.; YANG, W.; MCKITTRICK, J.; MEYERS, M. A. Keratin: Structure, Mechanical Properties, Occurrence in Biological Organisms, and Efforts at Bioinspiration. Progress in Materials Science, v. 76, p. 229-318, 2016.
[5] LAZARUS, B. S.; VELASCO-HOGAN, A.; GÓMEZ-DEL RÍO, T.; MEYERS, M. A.; JASIUK, I. A Review of Impact Resistant Biological and Bioinspired Materials and Structures. Journal of Materials Research and Technology. v. 9, p. 15705-15738, 2020
[6] FEUGHELMAN, M. Mechanical Properties and Structure of Alpha-Keratin Fibres: Wool, Human Hair and Related Fibres. Sydney: UNSW Press, 1997.
[7] FRASER, R. D.; MACRAE, T. P. Molecular Structure and Mechanical Properties of Keratins. Symposia of the Society for Experimental Biology, v. 34, p. 211-246, 1980.
[8] FRASER, R. D. B.; MACRAE, T. P.; ROGERS, G. E. Keratins: Their Composition, Structure and Biosynthesis, Charles C. Thomas. Springfield: [S. n], 1972.
[9] BERTRAM, J. E.; GOSLINE, J. M. Functional Design of Horse Hoof Keratin: The Modulation of Mechanical Properties through Hydration Effects. The Journal of Experimental Biology, v. 130, p. 121-136, 1987.
[10] FEUGHELMAN, M.; ROBINSON, M. S. The Relationship Between Some Mechanical Properties of Single Wool Fibers and Relative Humidity. Textile Research Journal, v. 37, p. 441-446, 1967.
[11] HUANG, W.; YARAGHI, N. A.; YANG, W.; VELAZQUEZ-OLIVERA, A., LI, Z.; RITCHIE, R. O.; KISAILUS, D.; STOVER, S. M., MCKITTRICK, J. A Natural Energy Absorbent Polymer Composite: The Equine Hoof Wall. Acta Biomaterialia, v. 90, p. 267-277, 2019.
[12] TOMBOLATO, L.; NOVITSKAYA, E. E.; CHEN, P. Y.; SHEPPARD, F. A.; MCKITTRICK, J. Microstructure, Elastic Properties and Deformation Mechanisms of Horn Keratin. Acta Biomaterialia, v. 6, p. 319-330, 2010.
[13] ZHANG, Q.; BIN, Li, C.; PAN, Y. T.; SHAN, G. H.; CAO, P.; HE, J.; LIN, Z. S.; AO, N. J.; HUANG, Y. X. Microstructure and Mechanical Properties of Horns Derived from Three Domestic Bovines. Materials Science and Engineering C, v. 33, p. 5036-5043, 2013.
[14] WANG, B.; ZHOU, B.; ZHANG, X.; WANG, B. Microstructure and Mechanical Properties of an Alpha Keratin Bovine Hoof Wall. Journal of Mechanical Behavior of Biomedical Materials, v. 104, 103689, 2020.
[15] CLARK, C.; PETRIE, L. Fracture Toughness of Bovine Claw Horn from Cattle with and without Vertical Fissures. The Veterinary Journal, v. 173, p. 541-547, 2007.
[16] BAILLIE, C.; SOUTHAM, C.; BUXTON, A.; PAVAN, P. Structure and Properties of Bovine Hoof Horn. Advanced Composites Letters. Journal, v. 9, 2000.
[17] ASTM D570-98 Standard Test Method for Water Absorption of Plastics, 2018.
[18] WU, M.; SHEN, S.; YANG, X.; TANG, R. Preparation and Study on the Structure of Keratin/PVA Membrane Containing Wool Fibers. IOP Conference Series: Materials Science and Engineering, v. 254, 2017.
[19] VALKOV, A.; ZINIGRAD, M.; SOBOLEV, A.; NISNEVITCH, M. Keratin Biomembranes as a Model for Studying Onychomycosis. International Journal Moleculary Science, v. 21, 2020.
[20] KASAPI, M. A.; GOSLINE, J. M. Exploring the Possible Functions of Equine Hoof Wall Tubules. Equine Veterinary Journal, v. 30, p. 10-14, 2010.

[21] KITCHENER, A. Effect of Water on the Linear Viscoelasticity of Horn Sheath Keratin. Journal Mater Science Letterring, v. 6, p. 321-322, 1987.
[22] COLLINS, S. N.; COPE, B. C.; HOPEGOOD, L., LATHAM, R. J.; LINFORD, R. G. Stiffness as a Function of Moisture Content in Natural Materials : Characterisation of Hoof Horn Samples. Journal Mater Science, v. 33, p. 5185-5191, 1998.
[23] FRASER, R. D. B.; MACRAE, T. P. The Structure of α-Keratin. Polymer (Guildf), v. 14, p. 61-67, 1973.
[24] KUI, H.; LIU, X.; LIU, J.; LIANG, W.; ZHANG, S.; QIAN, Z.; REN, L. The Passive Contact Stability of Blue Sheep Hoof Based on Structure, Mechanical Properties, and Surface Morphology. Frontiers in Bioengineering and Biotechnology, v. 8, p. 1-16, 2020.
[25] HUANG, W. Impact Resistant and Energy Absorbent Natural Keratin Materials: Horns and Hooves: [S. n.], 2018.
[26] PARKER, F. S. Amides and Amines. In Applications of Infrared Spectroscopy in Biochemistry, Biology, and Medicine. Boston: Springer, 1971. p. 165-172.
[27] KUMAR, S. L.; ANANDHAVELU, S.; SWATHY, M. Preparation and Characterization of Goat Hoof Keratin/Gelatin/Sodium Alginate Base Biofilm for Tissue Engineering Application. Integrated Ferroelectrics, v. 202, p. 1-12, 2019.
[28] VERMUNT, J. J.; GREENOUGH, P. R. Structural Characteristics of the Bovine Claw: Horn Growth and Wear, Horn Hardness and Claw Conformation. British Veterinary Journal, v. 151, p. 157-180, 1995.
[29] FRANCK, A.; COCQUYT, G.; SIMOENS, P.; DE BELIE, N. Biomechanical Properties of Bovine Claw Horn. Biosystem Engineer, v. 93, p. 459-467, 2006.
[30] WANG, B.; HUANG, Y.; ZHOU, B.; LI, W.; CHEN, H. Nanoindentation and Hierarchy Structure of the Bovine Hoof Wall. Materials (Basel), v. 14, 2021.
[31] ASSIS, B. M.; SILVA, L. A. F.; LIMA, C. R. O.; GOUVEIA, R. F.; VULCANI, V. A. S.; DE SANT'ANA, F. J. F.; RABELO, R. E. Microstructure and Hardness of Buffalo's Hoofs. Anatomia Histologia Embryologia, v. 46, p. 439-445, 2017.

VOL.40 Nº3 2023
https://doi.org/10.22491/rmct.v40i3.11622.en

Detection of Fake News in Virtual Social Networks: a review of methods based on propagation data

Argus Antonio Barbosa Cavalcante[1], Paulo Márcio Souza Freire[1], Ronaldo Ribeiro Goldschmidt[1], Claudia Marcela Justel[1]
[1]**Instituto Militar de Engenharia**
Rio de Janeiro, RJ, Brasil
argus@ime.eb.br

ABSTRACT: The popularization of virtual social media has significantly increased the intentional dissemination of false information, known as Fake News. This type of news can cause a wide range of negative impacts on society, reinforcing the need for developing computational methods that can detect this harmful type of news. Among the existing computational methods, those that use news propagation data have been highlighted given their relation with the disseminative nature of information on social media. Thus, this study describes a state-of-the-art review of Fake News detection methods based on news propagation data. By introducing the basic concepts related to these methods and describing and discussing their main characteristics, the authors intend to provide subsidies for the creation of new research in this area.

KEYWORDS: Virtual Social Networks. Disinformation. Fake News. Propagation data; Computational tools.

RESUMO: A popularização das redes sociais virtuais aumentou significativamente a divulgação intencional de informações falsas, as chamadas Fake News. Esse tipo de notícia pode causar uma grande variedade de impactos negativos à sociedade, o que reforça a necessidade do desenvolvimento de métodos computacionais que possam detectar esse tipo nocivo de notícia. Entre os métodos computacionais existentes, destacam-se aqueles que utilizam os dados de propagação da notícia, tendo em vista sua relação com a natureza disseminava das informações existentes nas redes sociais. Assim, este trabalho apresenta uma revisão do estado da arte dos métodos de detecção de Fake News baseados em dados de propagação da notícia. Ao introduzir os conceitos básicos relacionados a esses métodos, além de apresentar e discutir suas principais características, espera-se fornecer subsídios para a criação de novos trabalhos na área.

PALAVRAS-CHAVE: Redes Sociais Virtuais. Informações falsas. Fake News. Dados de propagação. Métodos computacionais.

1. Introduction

Although news dissemination has historically been linked to traditional means of communication, such as newspapers, magazines and television, recently virtual social networks (RSVs) have consolidated themselves as an important means of disseminating news to users [1]. Among the reasons for this change, we can highlight the relevance and popularity of RSVs today, as well as the existence of a simplified content publication process in these networks [2]. This process, combined with the wide variety of interaction mechanisms with the published content, ends up boosting the audience of the publications and consequently of the RSVs themselves.

In this context, in addition to the real news, based on the journalistic investigation of the facts and typically made by the press, one can also find several examples of false information intentionally disseminated, known as *Fake News* [2]. Several episodes in recent years have attracted attention to this type of information in RSVs, among which we can highlight:

- During and shortly after the occurrence of Hurricane Katrina in 2005, several fake news were disseminated with themes ranging from the origin and explanation of the atmospheric phenomenon, to what were the affected areas and the impacts generated on people's lives[1];
- On the occasion of the terrorist attacks on the Boston Marathon, which took place in the United States in 2013, false information was disseminated, generating fear and apprehension about the fact[2];

1 Cf.: https://www.theguardian.com/us-news/2015/aug/16/hurricane-katrina-new-orleans-looting-violence-misleading-reports

2 Cf.: https://www.bbc.com/news/world-us-canada-39930236

- In the 2016 American presidential elections, disputed by Republican candidate Donald Trump and Democratic candidate Hillary Clinton, *Fake News* was disseminated with the objective of distorting facts and opinions related to campaign themes in favor of one or another candidate[3]; - More recently, during the covid-19 pandemic, false information was disseminated with themes that covered the origin of the disease, the potential use and application of medicines, in addition to the effectiveness of vaccines[4].

Episodes like these can generate different impacts on society, such as discrediting the public image of people and institutions, problems involving public security, and even an eventual collective feeling of insecurity [3]. Its frequent occurrence attracts the attention of society, thus arousing the interest of academia and industry in understanding and analyzing the occurrence of this phenomenon.

Due to the large volume and speed of publications in RSVs, and also, given the difficulty of manually evaluating the veracity of the news, the use of computational methods to combat this type of content becomes increasingly common [2]. Among the main methods for detecting *Fake News*, those related to the use of news propagation data recently stand out for their intrinsic relationship with the dissemination nature of information in RSVs. These methods use data related to user interactions that occur from the publication of news, as in the case of sharing a post, a comment or other types of reaction to the published content [1].

Despite the promising results obtained by *Fake News* detection methods that use news propagation data, as far as it was possible to observe, there are still few state-of-the-art review works that explored [4] their main characteristics. Thus, this research intends to address some important aspects not addressed by previous works.

In addition to this introduction, the article contains three additional sections. *Section 2* presents a brief theoretical foundation of matters inherent to the theme of the review. *Section 3* presents the related works and the model used for their comparison. Finally, *Section 4* presents the conclusions of this review, in addition to some additional considerations.

2. Basic Concepts

2.1 Virtual Social Networks

In recent years, RSVs have become massively popular, causing millions of users to use them every day [5]. RSVs are composed of people, entities, companies, and organizations that connect and interact with each other, in a collaborative environment that offers several communication facilities for its users. Given the wide variety of existing RSVs, there was a segmentation of these networks according to the published content and the audience they intend to reach. For example, while TikTok's content[5] consists mainly of videos and is aimed at young audiences, Linkedin[6] is focused on the corporate world, being widely used by companies and professionals from the most varied industries.

Relationships in RSVs are established based on principles of social influence, similar to those existing in non-virtual social networks [6]. When people are connected in an RSV, it becomes possible to influence other people's behavior and decisions. This influence can be observed in several situations, such as, for example, in the opinions issued regarding products purchased, in the demonstration of political positions, in the information about activities carried out by a particular user, or even in a place visited by him. In the context of RSVs, people typically make decisions based on their inferences from what other

3 Cf.: https://www.washingtonpost.com/news/the-fix/wp/2018/01/03/how-hillary-clinton-might-have-inspired--trumps-fake-news-attacks/

4 Cf.: https://edition.cnn.com/2021/11/09/media/kaiser--covid-misinformation/index.html

5 Cf.: https://www.tiktok.com/

6 Cf.: www.linkedin.com

people have done. This behavior is known as *herding behavior* [6] and occurs in the form of a sequential decision-making process of the users of a network. The popularity of RSVs, added to the social influence among their users, reinforce the need to study *Fake News* on these networks.

2.2 False Information

The state of the art characterizes the different types of false information such as *Misinformation* and *Disinformation* [2]. The first type includes information that is accidentally false as a result of errors. In the second type, there is the information known to be false, intentionally disclosed. That is, intentionality is established as a fundamental criterion used to distinguish the two types of false information. In this context, for a news to be considered a *Fake News*, one must confirm its dissemination was intention.

It is worth mentioning that the *Fake News* found in the RSVs are part of a system composed of several participants, and which goes beyond these networks. Among the most relevant participants are the press, fact-checking agencies, publicly exposed people, the legislative and judicial branches, as well as the users of RSVs themselves [2]. Although not all types of false information are necessarily news, as previously mentioned, the press plays an important role in the system of spreading false information. In some situations, the traditional process of journalistic work is mischaracterized by false information, replacing the careful investigation of the facts and the impossibility of the parties involved to express their opinions (often of a contradictory nature). To complement the work of the press in the context of *Fake News*, fact-checking agencies emerged. These agencies also monitor the information disseminated in traditional media, but focus on those circulating in RSVs [1]. The information analyzed is typically in the form of articles, news or even speeches and statements coming mostly from public people, giving preference to matters of general interest that have recently gained prominence. As a result of their work, an evaluation of the information analyzed is obtained, based on the fact-checking process that is carried out by their teams.

Publicly exposed people, such as celebrities, politicians, social influencers and other prominent personalities, are commonly both targets and disseminators of false information, since information related to these people usually obtain greater reach, as they are more shared and discussed [7]. The legislative and judicial branches play a central role in this system. With the increase in the dissemination of false information in RSVs, the need has arisen to study and propose laws that can punish those responsible for its dissemination, especially when they cause some kind of damage to the parties involved. Both in the Brazilian judiciary and in other countries, there are currently discussions in this regard. In the absence of specific laws, the judiciary today uses general laws, such as, for example, the laws of material and moral damages arising from the possible aggression to the honor of victims of false information [8].

2.3 Automatic Fight against Fake News

In addition to the manual treatment that can be carried out by a fact-checking agency, another possibility has been widely explored recently, namely the use of computational resources to automatically detect *Fake News*, thus avoiding the need for manual detection or complementing it when necessary [1]. This alternative has been widely feasible, especially due to the advance in the use of computational methods through the application of data mining and machine learning techniques [9], in addition to the increase in the processing capacity of the computers that support its execution.

In the context of the automatic fight against *Fake News*, two main features are consolidated: the detection and intervention of *Fake News* [4]. In detection we have, in short, a binary classification problem. Considering the evaluation of a given news, the result will be true if it is *Fake News*, or false otherwise. In order to

avoid the harmful effects of the dissemination of *Fake News*, we have the intervention functionality, in which it becomes possible to interrupt the propagation of a particular news.

3 State of the Art

3.1 Selection of works

To analyze the state of the art of methods for detecting *Fake News* that use news propagation data, a set of criteria was defined for the selection of related works. Initially, the bases of articles to be consulted were defined. Due to its popularity in topics related to computing, the following were selected: Institute of Electrical and Electronics Engineers (IEEE)[7], *Association for Computing Machinery* (ACM)[8], and Science Direct[9]. Once the article bases were defined, an initial search question was identified consisting of the keywords related to the theme of propagating intentionally disseminated false information, resulting in *"Fake News"+ propagation*. In addition to the search question, the criterion of identifying the system of "qualis" classification of articles was used, privileging, whenever possible, those in the upper stratum. Papers written after 2015 were considered due to the lack of papers published before this cut-off date.

3.2 Related Works

This section will present the works selected for review in which computational methods were developed for the detection of Fake News based on news propagation data. Each work is briefly described, including the data used, the type of learning, datasets and best results obtained in the experiments carried out by these works. Additional details of these works can be found through their references:

- *News credibility evaluation on microblog with a hierarchical propagation model* [10]: the authors rely on the triad of news, user and community to detect *Fake News*, proposing, as part of their study, the creation of a hierarchical model that identifies sub-events within the news, to describe their details. The automatic detection problem is treated as a graph optimization problem, in which an optimal solution is proposed. Text content data, *hashtag* topics, links, among others, were used. This work is based on supervised learning. The *datasets* used are SW-2013 and SW-MH370. The best result obtained was 0.889 (Accuracy).
- *CSI: A hybrid deep model for Fake News detection* [11]: the detection process is divided into three parts: *Capture, Score and Integrate* (CSI). The first module is based on the response and text, through a recurrent neural network, *long short-term memory* (LSTM), to capture a temporal pattern of user activities on the article and the *doc2vec* representation of the text generated in this activity. The second uses a neural network to learn the characteristics of the source based on the behavior of users according to their interactions, generating a score through a graph. The two modules are integrated with the third to characterize, or not, the article as *Fake News*. User data was used, without specifying exactly which ones. This work is based on supervised learning. The *datasets* used are Twitter and Weibo. The best result obtained was 0.892 (Accuracy).
- *Tracing fake-news footprints: Characterizing social media messages by how they propagate* [12]: this method uses the proximity of the nodes and the social dimensions to infer a representation of the users of the social network to subsequently represent and classify the propagation paths of messages propagated by said users. Data from the news propagation structure were used. This work is

7 Cf.: https://ieeexplore.ieee.org/

8 Cf.: http://dl.acm.org

9 Cf.: https://www.sciencedirect.com

based on supervised learning. The *dataset* used is an adaptation of Twitter. The best result obtained was 0.9380 (F-Measure).

- *Fake news detection on social media using geometric deep learning* [13]: this explores patterns of propagation of Fake News using *Geometric Deep Learning* (generalization of *deep learning* techniques to non-Euclidean data such as graphs that use convolutional neural networks), using four types of information: user profile, user activity, network, and content. Profile settings data, language, profile description, geolocation, verified user, social connections between users, and others were used. This work is based on supervised learning. The *datasets* used are adaptations of Twitter15 and Twitter16. The best result obtained was 92.7% (ROC AUC).
- *Hierarchical propagation networks for Fake News detection: Investigation and exploitation* [14]: developed the concept of hierarchical network propagation for the detection of Fake News. To build this hierarchical structure, it is based on two levels: 1. Macro-level (topological and temporal analysis of the network) and 2. Micro-level (topological, temporal and linguistic analysis of the network). Data from the news propagation structure were used. This work is based on supervised learning. The *datasets* used are Politifact and GossipCop. The best result obtained was 0.863 (Accuracy).
- *Network-based Fake News detection: A pattern-driven approach* [15]: proposes to investigate the patterns of dissemination of Fake News. In general, these patterns can be classified into three groups: 1. News-related patterns, 2. Patterns related to news publishers and 3. Patterns of relationship between the disseminators of the news. Data from the news propagation structure were used.This work is based on supervised learning. The *datasets* used are Politifact and BuzzFeed. The best result obtained was 0.929 (Accuracy).
- *GCAN: Graph-aware co-attention networks for explainable Fake News detection on social media* [16]: uses the content of the original *tweet* and the sequence of corresponding *re-tweets* to detect the news as "*fake*" or "*not fake*". First, it extracts user information from their profiles and interactions, learning how to *embed* original content. It then uses convolutional (CNN) and recurrent (RNN) neural networks to learn the representation of the spread of *re-tweets*, building a graph that models the possible interactions between users. Finally, it establishes the correlation between the original tweet and its propagation, generating a binary prediction based on this correlation. Geolocation data, verified user, among others, were used. This work is based on supervised learning. The *datasets* used are Twitter15 and Twitter 16. The best result obtained was 0.9084 (Accuracy).
- *Graph neural networks with continuous learning for Fake News detection from social media* [17]: the authors consider that false and true information propagate differently on the internet. In addition to the flow information, they use eight attributes of the posts (verified Twitter user, user creation *timestamp*, number of followers, number of friends, number of lists, number of favorites, number of status and *timestamp* of tweets). It uses graph neural networks (GNN) to differentiate *fake* and *non-fake* news patterns. Verified user data, profile creation date, among others, were used. This work is based on supervised learning. The *datasets* used are from FakeNewsNet (Politifact and GossipCop). The best result obtained was 0.853 (Accuracy).
- Unsupervised Fake News Detection: A Graph--based Approach [18]: Method consisting of three steps: 1. Bi-click mining, based on news shared synchronously, generating a *Seed* set (heterogeneous graph – user and article vertices); 2. Bi-click mining of the remaining articles (without the restriction of synchronous sharing), using similarity of publication text and user information; and 3. Mining of the remaining articles (outside the bi-clicks), using similarity of the publication text and user information. Data from the news propagation structure were

used. This study was based on unsupervised learning. The *datasets* used are from FakeNewsNet (Politifact and GossipCop). The best result obtained was 0.800 (Accuracy).

- *Fake news detection in social networks via crowd signals* [19]: Motivated by a tool at the time, recently introduced in the Facebook social network, in this work the so-called *crowd signals* were used to detect *Fake News*. These signals are the explicit opinion of users indicating that certain content is *Fake News*. Its authors developed an algorithm that performs Bayesian inference capable of learning over time about the ability of users to opine on this type of content. User opinion data was used. This is based on semi-supervised learning. The *dataset* used is Facebook. The best result obtained was 0.9967 (Accuracy).
- *Fake news detection based on explicit and implicit signals of a hybrid crowd: An approach inspired in* meta-learning [20]: inspired by [19], this work also uses so-called *crowd signals* to detect *Fake News*. However, in contrast to the initial work, which uses the so-called explicit opinion of users, issued through a tool aimed at this purpose –, its authors explored the use of the implicit opinion of users, obtained through their behavior when interacting with this type of content. This work also combines the implicit opinion of users with that of machines (algorithms), forming the so-called hybrid crowd. Data on the implicit opinion of users, in addition to the number of interactions and the text of the news were used. This work is based on supervised learning. The *datasets* used are Gossip, Politifact, Gossip2, FakeNewsSet and FakeBR. The best result obtained was 0.9989 (Accuracy).
- *Early detection of Fake News on social media through propagation path classification with recurrent and convolutional networks* [21]: this work uses the classification of the propagation flow created by the news to perform early detection. This classification is carried out from the modeling of the news dissemination flow as a multivariate time series, in which each pair of values is a numerical vector representing the characteristics of the user who participated in the propagation process. User data such as their friendships and followers were used, as well as the age and geolocation characteristics of these users, among others. This work is based on supervised learning. The *datasets* used are Twitter 15, Twitter16 and Weibo. The best result obtained was 0.921 (Accuracy).
- *Propagation2vec: Embedding partial propagation networks for explainable Fake News early detection* [22]: the authors attribute different levels of importance to the elements of news propagation, reconstructing knowledge about the complete flow of this news based on partial flows of the propagation. The method uses hierarchical attention mechanisms to emphasize the most important information in these flows. User data such as: whether they are verified, their followers, friends, lists, favorites, *tweets*, among others, were used. This work is based on supervised learning. The *datasets* used are Politifact, Gossipcop. The best result obtained was 0.897 (Accuracy).
- *Detect rumors in microblog posts using propagation structure via kernel learning* [23]: initially creates a representation of propagation through trees to subsequently capture patterns that differentiate the types of rumors by evaluating the similarity of their structure (kernel-based method). Although it describes the detection of rumors, the output of this method also points out a news as "*fake*" or "*not fake*" *(non-rumor, false rumor, true rumor or unverified rumor*). User data such as their followers and friendships, account verification status, post history, among others, were used. This work is based on supervised learning. The *datasets* used are adaptations of Twitter15 and Twitter16. The best result obtained was 0.750 (Accuracy).

3.2 Comparative model

To proceed with the analysis of the state of the art, three criteria for comparison between the selec-

ted works were defined. These are: the propagation data used, the indication of the use of restricted access data, and whether they perform early detection of *Fake News*. The choice of these criteria aims to deepen the understanding of the main characteristics and limitations existing in the selected works.

There is a wide variety of propagation data used by the state of the art. In [4]'s work, a classification of these data was established considering the following categories: contribution, user, subject, temporality, and network. User's contribution concerns the different types of media (e.g., text, audio, or images) used during propagation. In relation to the user who propagates the news, their profile data and reputation are obtained, which may be linked to their ability to identify or publish *Fake News*. Another relevant aspect is the subject of the news, which aims to explore the relationship of the news in question with popular and controversial issues. Regarding the temporality criterion, data on the time of each of the news propagations are used, an important criterion from the point of view of the automatic detection of *Fake News*. Finally, we also have the network criterion, in which we intend to identify whether data from the relationships of each user who interacted with a given news item were used.

Based on the exposed classification, Table 1 summarizes the relationship of the selected works with the types of propagation data used. It is possible to observe that the most frequently used types are user data and their network of relationships, in addition to the temporality related to the interactions that occurred during the propagation of the news. The contribution data were also used, albeit in smaller numbers.

Although several propagation data are used by the state of the art, their practical application can be made unfeasible in the face of restrictions on access to these data. These restrictions are mainly due to the consolidation of the legal framework of data privacy [24], especially due to laws such as the *General Data Protection Regulation* (GDPR) and the General Data Protection Law (LGPD). Considering the large number of security incidents and the popularization of internet use around the world, there was a great debate about the need for laws to help combat cybercrime, which culminated in the creation of these laws. In response to this move, RSVs created their data privacy policies, ensuring proper handling and restriction of data access. These policies focus primarily on personal data (e.g., name, surname, photograph, and geographic location) and sensitive data (religion, racial origin, among other examples). Personal data can be used to identify a user, while sensitive data has the potential to discriminate against people. Thus, studies that depend on restricted access data to detect *Fake News* have a significant disadvantage compared to those that do not depend on this data.

Table 1 - Use of propagation data: C (Contribution), U (User), A (Network), T (Temporality) and R (Network).

Study	C	U	A	T	R
[10]		X	X		
[11]		X		X	X
[12]		X		X	X
[13]		X		X	X
[14]	X	X		X	X
[15]	X	X			X
[16]	X	X		X	X
[17]	X	X		X	X
[18]	X	X		X	X
[19]		X			
[20]	X	X		X	X
[21]	X	X		X	X
[22]		X		X	X
[23]		X		X	X

Table 2 presents a summary of the studies related to the use of restricted access data, and it is possible to observe that there is an equivalent distribution between the studies that depend on these data and those that do not.

A challenge posed to automatic *Fake News* detection methods, both for those using the propagation data or possibly other types of data, is the fact that the propagation of the news can take hours, days, weeks and even years to complete. From the moment the news is published, it can be permanently available. That is, users who may have access to this content can still interact with it and thus can create new cycles of news propagation. Considering that waiting longer makes it difficult to implement intervention actions aimed at avoiding the impacts of *Fake News*, some detection methods based on propagation data seek to perform detection in advance [1]. In these works, detection must be carried out in the early stages of propagation, that is, before this news has been widely disseminated. This criterion was also considered as part of the analysis of the state of the art.

Looking at Table 3, one can verify that the use of early detection by *Fake News* detection methods is still uncommon.

Table 2 - Use of restricted access data.

Study	Does it use Restricted Access Data?
[10]	Yes
[11]	Could not be determined.
[12]	No
[13]	Yes
[14]	No
[15]	No
[16]	Yes
[17]	Yes
[18]	No
[19]	No
[20]	No
[21]	Yes
[22]	Yes
[23]	Yes

Table 3 - Use of Early Detection.

Study	Does it perform Early Detection?
[10]	No
[11]	No
[12]	No
[13]	No
[14]	No
[15]	No
[16]	No
[17]	No
[18]	No
[19]	No
[20]	No
[21]	Yes
[22]	Yes
[23]	Yes

4 Final considerations

In recent years, the use of virtual social networks to disseminate news has become increasingly frequent. However, these networks are also used for the dissemination of Fake News, which are intentionally false information. In this article, a review of the state of the art was performed, focusing on works that use a particular type of data related to the propagation of news. Although popular, few reviews [4] have been made to specifically evaluate this particular type of data. In this context, this article updated the previous review work [4], highlighting the Fake News detection works that use propagation data. The result of this review points out some relevant observations that deserve to be highlighted. First, the spectrum of propagation data types used by the state of the art is broad. Regarding the use of restricted access data, the work is divided in a balanced way among those who depend on this data or not. Finally, the early detection of Fake News, which seeks to enable intervention actions after news detection, is still little explored.

References

[1] ZHOU, X.; ZAFARANI, R. A survey of Fake News: Fundamental theories, detection methods, and opportunities. *ACM Computing Surveys*, New York, v. 53, n. 5, p. 1-40, 2020.

[2] SHARMA, K.; QIAN, F.; JIANG, H.; RUCHANSKY, N.; ZHANG, M.; LIU, Y. Combating Fake News: A survey on identification and mitigation techniques. *ACM Transactions on Intelligent Systems and Technology*, New York, v. 10(3), n. 21, p. 1-42, Apr. 2019.

[3] WATTS, D. J.; ROTHSCHILD, D. M.; MOBIUS, M. Measuring the news and its impact on democracy. *Proceedings of the National Academy of Sciences*, Madison, v. 118, n. 5, e1912443118, 2021. DOI 10.1073/pnas.1912443118

[4] FREIRE, P. M.; GOLDSCHMIDT, R. R. Combate automático às Fake News nas mídias sociais virtuais. *Revista Militar de Ciência e Tecnologia*, Rio de Janeiro, v. 38 n. 2, p. 3-12, 2021.

[5] EASLEY, D.; KLEINBERG, J. *Networks, Crowds, and Markets: Reasoning About a Highly Connected World*. Cambridge: Cambridge University Press, 2010.

[6] EASLEY, D; KLEINBERG, J. *Networks, Crowds, and Markets*: Reasoning about a Highly Connected World. Cambridge: Cambridge University Press, 2010.

[7] KUMAR, S.; CHENG, J.; LESKOVEC, J. Antisocial behavior on the web: Characterization and detection. *In*: INTERNATIONAL CONFERENCE ON WORLD WIDE WEB COMPANION, 26., 2017, Perth. *Anais* […]. Republic and Canton of Geneva: International World Wide Web Conference Committee, 2017. p. 947–950.

[8] FLUMIGNAN, W. G. G. As Fake News à luz da legislação brasileira. *Revista Científica Disruptiva*, Recife, v. 2 n. 2, p. 145-161, 2020.

[9] GOLDSCHMIDT, R.; PASSOS, E.; BEZERRA, E. *Data Mining*. 2. ed. Rio de Janeiro: Elsevier Brasil, 2015.

[10] JIN, Z.; CAO, J.; JIANG, Y. G.; ZHANG, Y. News credibility evaluation on microblog with a hierarchical propagation model. *In*: IEEE INTERNATIONAL CONFERENCE ON DATA MINING, 14., 2014, Shenzhen. *Anais* […]. Piscataway: Institute of Electrical and Electronics Engineer, 2024. p. 230–239.

[11] RUCHANSKY, N.; SEO, S.; LIU, Y. CSI: A hybrid deep model for Fake News detection. *In*: INTERNATIONAL CONFERENCE ON INFORMATION AND KNOWLEDGE MANAGEMENT, 26., 2017, Singapore. *Anais* […]. New York: Association for Computing Machinery, 2017. p. 797–806.

[12] WU, L.; LIU, H. Tracing fake-news footprints: Characterizing social media messages by how they propagate. *In*: INTERNATIONAL CONFERENCE ON WEB SEARCH AND DATA MINING, 11., 2018, Marina Del Rey. *Anais* […]. New York: Association for Computing Machinery, 2018. p. 637-645.

[13] MONTI, F.; FRASCA, F.; EYNARD, D.; MANNION, D.; BRONSTEIN, M. M. Fake News detection on social media using geometric deep learning. Appleton: *ICLR*, 2019.

[14] SHU, K.; MAHUDESWARAN, D.; WANG, S.; LIU, H. Hierarchical propagation networks for Fake News detection: Investigation and exploitation. *Proceedings of the International AAAI Conference on Web and Social Media*, [*s. l.*], v. 14, n. 1, p. 626-637, 2019.

[15] ZHOU, X.; ZAFARANI, R. Network-based Fake News detection: A pattern-driven approach. *SIGKDD Explorations*, [*s. l.*], v. 21, n. 2, p. 48-60, 2019.

[16] LU, Y.-J; LI, C.-T. GCAN: Graph-aware co-attention networks for explainable Fake News detection on social media. *In*: ANNUAL MEETING OF THE ASSOCIATION FOR COMPUTATIONAL LINGUISTICS, 58., 2020 , Online. *Anais* […]. Kerrville: Association for Computational Linguistics, 2020. p. 505–514.

[17] HAN, Y.; KARUNASEKERA, S.; LECKIE, C. *Graph neural networks with continual learning for Fake News detection from social media*. Nova York: Cornell University, 2020.

[18] GANGIREDDY, S. C. R. P. D.; LONG, C.; CHAKRABORTY, T. Unsupervised Fake News detection: A graph-based approach. *In*: HYPERTEXT AND SOCIAL MEDIA, 31., 2020, Online. *Anais* […]. New York: Association for Computing Machinery, 2020. p. 75–83.

[19] TSCHIATSCHEK, S.; SINGLA, A.; GOMEZ RODRIGUEZ, M.; MERCHANT, A.; KRAUSE, A. Fake news detection in social networks via crowd signals. In: COMPANION PROCEEDINGS OF THE THE WEB CONFERENCE 2018, *Anais* […]. Republic and Canton of Geneva: International World Wide Web Conferences Steering Committee, 2018. p. 571-524.

[20] SOUZA FREIRE, P. M.; MATIAS DA SILVA, F. R.; GOLDSCHMIDT, R. R. Fake news detection based on explicit and implicit signals of a hybrid crowd: An approach inspired in meta-learning. *Expert Systems with Applications*, [*s. l.*], v. 183, 115414, 2021.

[21] LIU, Y.; WU, Y.-F. Early detection of Fake News on social media through propagation path classification with recurrent and convolutional networks. Thirty-Second AAAI Conference on Artificial Intelligence, 32., 2018, New Orleans. *Anais* […]. Palo Alto: AAAI Press, 2018. p. 354-361.

[22] SILVA, A.; HAN, Y.; LUO, L.; KARUNASEKERA, S.; LECKIE, C. Propagation2vec: Embedding partial propagation networks for explainable Fake News early detection. *Information Processing Management*, [*s. l.*], v. 58, n. 5 102618, 2021.

[23] MA, J.; GAO, W.; WONG, K. Detect rumors in microblog posts using propagation structure via kernel learning. In THE 55TH ANNUAL MEETING OF THE ASSOCIATION FOR COMPUTATIONAL LINGUISTICS, 55., 2017, Vancouverv. 1. *Anais […]*. Kerrville: Association for Computational Linguistics, 2017. p. 708–717.

[24] FINKELSTEIN, M.E.; FINKELSTEIN, C. Privacidade e lei geral de proteção de dados pessoais. *Revista de Direito Brasileira*, São Paulo, v. 23, n. 9, p. 284-301, 2019.

VOL.40 Nº3 2023
https://doi.org/10.22491/rmct.v40i3.11676.en

Development of a radio frequency magnetron sputtering system for the production of thin films

Austim Mota Gomide Pimenta[1] and Carlos Ferreira[1]
[1]Materials Engineering Teaching Section – SE/8, Military Institute of Engineering, Rio de Janeiro, Brazil,
austimpimenta@gmail.com
argus@ime.eb.br

ABSTRACT: This work describes the design, construction and characterization of a radio frequency magnetron sputtering system for thin film deposition. Target-materials with different electrical properties were used for system characterization: copper, indium oxide and silicon dioxide. The films were deposited on glass and silicon substrates, at room temperature, under a pressure of 8x10-4 Torr. The microstructure of the obtained thin films was investigated by X-ray diffraction and atomic force microscopy. Electrical and optical properties were obtained by Hall effect and transmittance measurements, respectively. The results showed that the assembled sputtering system allows the deposition of high quality films with high thickness uniformity. Linear dependence of the deposition rate on the work power was achieved for the deposited films, whose properties were well consistent with those reported in the literature. These results show the control of deposition parameters in the assembled system.

KEYWORDS: Instrumentation. RF Magnetron Sputtering. Thin Films. Structural Properties. Electrical Properties. Optical Properties.

RESUMO: Este trabalho descreve a concepção, a construção e a caracterização de um sistema de pulverização catódica com fonte de radiofrequência assistida por campos magnéticos para deposição de filmes finos. Materiais para alvo com propriedades elétricas distintas, foram usados para caracterizar o sistema: cobre, óxido de índio e dióxido de silício. Os filmes foram depositados em substratos de vidro e silício, à temperatura ambiente, com uma pressão de deposição da ordem de 8x10^{-4} Torr. A microestrutura dos filmes finos obtidos foi caracterizada por difração de raios x e microscopia de força atômica. As propriedades elétricas e óticas foram obtidas pelas medidas de efeito Hall e de transmitância, respectivamente. Os resultados mostraram que o sistema construído possibilita a deposição de filmes de alta qualidade e boa uniformidade de espessura. Para todos os materiais investigados, a taxa de deposição aumentou linearmente com a potência e as propriedades obtidas estavam de acordo com os valores reportados na literatura, mostrando o controle dos parâmetros de deposição no sistema construído.

PALAVRAS-CHAVE: Instrumentação. Pulverização Catódica. Filmes Finos. Propriedades Estruturais. Propriedades Elétricas. Propriedades Ópticas.

1. Introduction

Theoretical advances in the various fields of science impose the need to establish mastery of techniques and improvement of equipment assembly skills, in such a way that the branch of scientific instrumentation is essential for developing the various areas of science. In recent decades, thin film deposition techniques have stood out due to their applications, both in industry and in various fields of science [1]. The production of materials, in the form of thin films by sputtering, stands out for the ability to manufacture thin films of materials with complex compositions, at room temperature, regardless of their electrical, optical, and mechanical properties [2, 3, 4].

This study's objective is to present the design and construction of a system for the deposition of thin films by sputtering with a radio frequency source assisted by magnetic fields (RF Magnetron Sputtering), for the manufacture of thin films. To prove the success of the assembled system, thin films of materials with different electrical properties were deposited: copper, as an electrically conductive material, silicon dioxide, as an electrical insulating material, and indium oxide, with semiconductor properties. Finally, the thin films produced were characterized to prove their quality as well as the technical feasibility of the assembled equipment.

2. Materials and Methods

2.1 Development of the Magnetron Sputtering System Project

For the project assembly, a stainless-steel cylindrical bell jar, measuring 30 cm in diameter and 30

cm in height, was used for the deposition chamber. It was evacuated by a system consisting of a diffusion pump with a cryogenic trap to obtain high vacuum, a dry scroll vacuum pump to obtain primary vacuum, a valve with controlled opening for the pumping conductance during deposition, and a set of pressure gauges. The assembly of the projected deposition system was divided into stages:

- (i) Dimensioning and assembly of a cabinet to support the bell jar and gauges, using angle brackets of carbon steel, and aluminum plates to support the equipment and its closure. An aluminum plate was placed at the top of the cabinet to support the deposition chamber, and another aluminum plate was placed at the bottom to support the pumping system. Figure 1 illustrates the equipment structural design;
- (ii) Use of a 306L stainless-steel cylindrical disc to support the internal components of the deposition system (base plate);
- (iii) Design of the electrical power system, enabling the independent supply of the electronic equipment that comprise the deposition system and the performance of individual tests in each part of the electrical system, both in the vacuum pumping system and in the radio frequency and instrumentation equipment;
- (iv) Resizing and adaptation of the pre-existing vacuum system at the Laboratory of the Thin Film (LFF) of the Military Institute of Engineering (IME) (Figure 2);
- (v) Sizing and installation of the forced air-cooling system with cold water for the diffusion pump, and for the target material for deposition;
- (vi) Assembly and installation of a shutter to protect the substrates during the stage of removal of impurities affixed to the target surface, and in the stage of control of deposition rate and film thickness;
- (vii) Installation of a stainless-steel square as a substrate holder with 10 cm edge, with adjustable height, to accommodate four square substrates of 2.5 cm;
- (viii) Installation of a RFX 600 radio frequency generation source, and an ATX module of automatic impedance-matching for the substrate-cathode, both manufactured by Advanced Energy;
- (xix) Installation of a magnetron cathode, model MAK3, manufactured by MEIVAC, which holds 3-inch diameter targets;
- (x) Installation of a pressure gauge with capacitive membrane, manufactured by EDWARDS (Barocel® model 600A-100T-R12-N12X-4), to evaluate the base pressure of the system, and a cold cathode ionization gauge, manufactured by EDWARDS (Penning®, model 6 D145-08-00), for evaluation of the high vacuum;
- (xi) Installation of a pressure gauge with capacitive membrane, model 626ª01TDE manufactured by MKS, for pressure measurement during deposition;
- (xii) Installation of a needle valve, model SS-4-BK manufactured by Swagelok®, to control the flow of argon in the chamber during the purging and deposition stages.

The designed and assembled system is shown in Figure 3.

Fig. 1 - Schematic representation of the support cabinet in exploded-view drawing.

Fig. 2 - a) High vacuum system; b) Schematic of the vacuum system in exploded-view drawing.

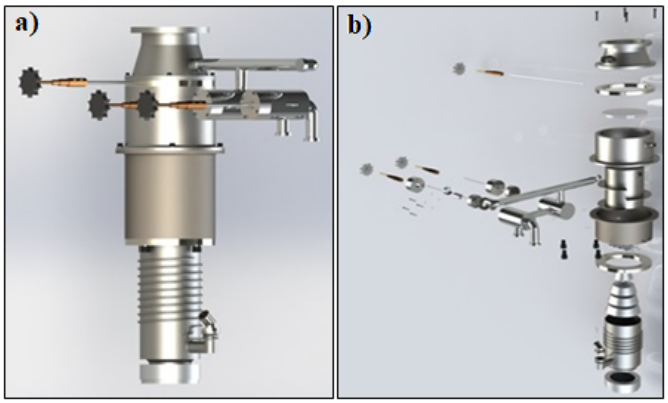

Fig. 3 - a) Design of the sputtering system; b) Photograph of the sputtering system assembled.

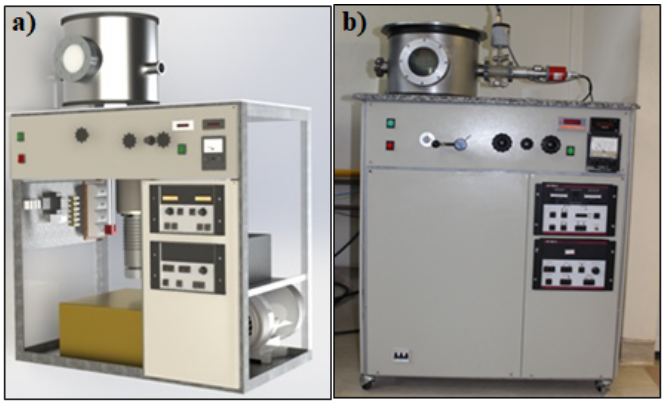

2.2 Characterization of the deposition system

To characterize the deposition system initially assembled, thin films deposited on glass slides and on monocrystalline silicon chips were produced.

Before sample production, the system was pumped up to a base pressure of $8x10^{-6}$ Torr, followed by the stage of obtaining an argon residual atmosphere. This step was performed with the following experimental procedure: a first purge was performed by injecting argon into the deposition chamber, using the needle valve to raise the pressure up to 3 mTorr. The pressure was maintained for about 60s; subsequently, the pressure was reduced to the base pressure by closing the needle valve. This procedure was performed at least three times to ensure that the argon residual atmosphere was obtained. Finally, the pressure was maintained at 3 mTorr to perform the deposition.

For the production of a full series of samples, copper, silicon dioxide, and indium oxide targets were used. The films were deposited on glass slides and with different power outputs to characterize the deposition system. Table 1 presents the deposition parameters used, kept constant during the production of the films, regardless of the type of target material used.

Table 1 - Parameters kept constant during depositions.

Parameters	Values
System Base Pressure	~$8x10^{-6}$ Torr
Plasma opening pressure	30 mTorr
Deposition pressure	1 mTorr
Target-substrate distance	75 mm
Deposition temperature	Ambient

After the production of the thin films, thickness was measured using the Veeco profilometer, model Dektak 150 of the LFF, and the Dektak 8 from the Materials Division (Dimat) of INMETRO. To obtain electrical resistivity, the LFF BioRad equipment model HL 5500 was used. For structural characterization of the deposited films, the X'Pert Powder diffractometer of PANalytical, from the Laboratory of X-ray Diffraction of IME, was used. For morphological analysis, a Witec atomic force microscopy (AFM), model Alpha 300 from Dimat/INMETRO, and the high-resolution scanning electron microscope, model HELIOS NANOLAB, FEI trademark installed at the Microscopy Center of INMETRO, were used.

3. Results

The copper target was the first material used to manufacture the films, followed by the silicon dioxide target, due to its opposite electrical properties. The other material used for the characterization of the deposition system was indium oxide, for its semiconduc-

tor characteristic. Tables 2 to 4 present the deposition parameters used, with the values obtained for thickness, deposition rate, and resistivity of films (since SiO_2 films are insulating, they could not be measured for resistivity). The deposition time was maintained at 10 min for copper depositions and 60 min for SiO_2 and In_2O_3 depositions. The deposition pressure was maintained at 1 mTorr for all depositions. Due to the insulating characteristic of silicon dioxide, it was necessary to apply higher power outputs to enable film production with deposition rates in the same range as those used in copper and In_2O_3 targets.

Table 2 - Thickness and resistivity of thin films of copper in function of deposition parameters.

Film	Power (W)	Thickness (Å)	Rate (Å/s)	Resistivity (μΩ.cm)
1	20	393	0.7	0.1
2	50	1366	2.3	1.6
3	80	2445	4.1	0.6
4	110	3850	6.4	3.6

Table 3 - Thickness and resistivity of thin films of SiO_2 in function of deposition parameters.

Film	Power (W)	Thickness (Å)	Rate (Å/s)
1	100	3396	0.9
2	150	6266	1.7
3	200	9125	2.5

Table 4 - Thickness and resistivity of thin films of In_2O_3 in function of deposition parameters.

Film	Power (W)	Thickness (Å)	Rate (Å/s)	Resistivity (μΩ.cm)
1	20	2265	0.6	131
2	50	5272	1.4	138
3	80	10152	2.8	195
4	110	14282	3.9	120

Figure 4 shows the behavior of the deposition rate in function of the power used to produce the films. Analyzing Figure 4, it is possible to observe the existence of a very strong linear correlation between the deposition rate of the three materials used and the work power. This result is well known in the literature [5-7] and attests to the control of this important deposition parameter in the assembled system.

Fig. 4 - Deposition rate of thin films manufactured in the sputtering system in function of power: a) copper; b) SiO_2, and c) In_2O_3.

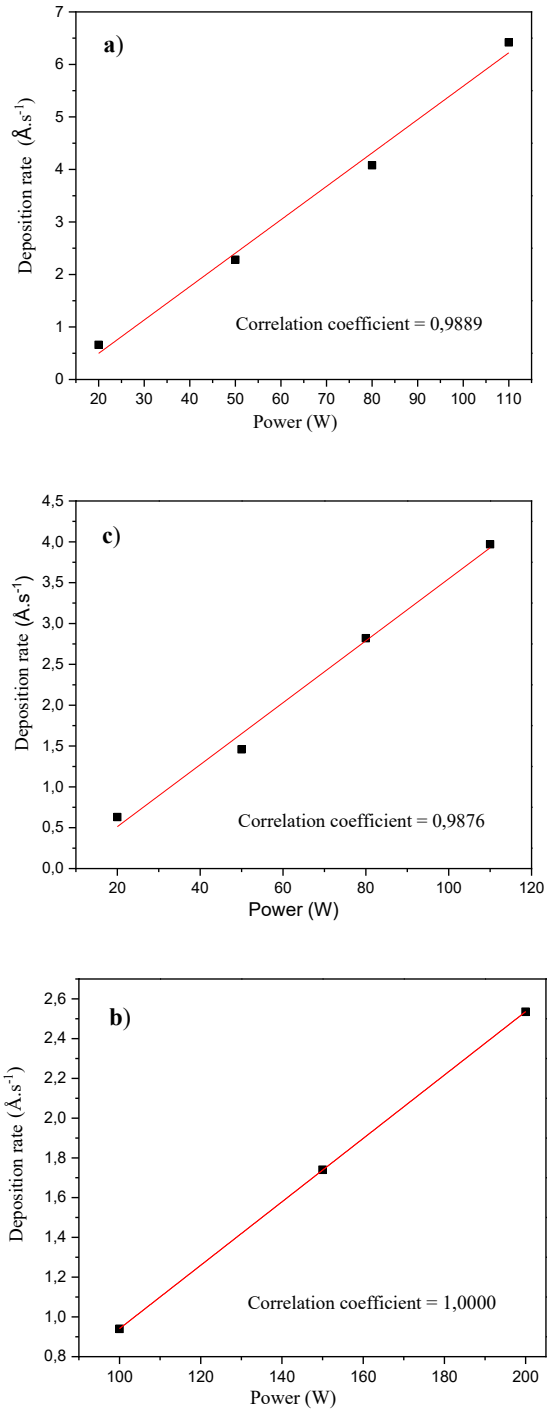

Figure 5 shows the diffractograms of the deposited films at different power outputs. It is important to highlight the absence of contaminating phases in the deposited films, which attest to this system capacity of depositing pure and good quality films.

In the case of copper films, it is observed that the films deposited with the powers of 50, 80, and 110W are crystalline and show a preferential growth in the direction (111), according to the crystallographic data JCPDS 00-004-0836 of copper. It is also observed that the thin film deposited with 110W has higher crystallinity than the others, while the copper thin film deposited with 20W is amorphous. The crystallinity resulting from the work power increase is possibly related to the greater number of atoms that reach the substrate per time interval, favoring the increase in the thickness of films and, consequently, the crystallinity. The amorphous characteristic of the film deposited with 20 W is due to the low deposition rate used (0.7 Å/s) resulting in a small thickness, when compared to other films.

Degrees
Deposition power (W)

Analyzing the diffractograms of SiO_2 films, it is possible to observe that all films are amorphous. This result is well known and related to the fact that the films were grown at room temperature [8,9].

The diffraction peaks of films In_2O_3 were identified with the crystallographic card JCPDS 00-006-0416. Analyzing the diffractogram of the film deposited with 50 W, there is a very strong crystallographic orientation in the direction (222). However, the film grown at 110 W showed higher crystallinity with a preferential growth in the direction (400). It is also noted that the power increase favored crystallinity, which is also reported by other authors as resultant of the greater kinetic energy of the molecules colliding with the substrate [9-11]. However, in this study, it is worth mentioning that such effect is much more due to the greater thickness of the films deposited with higher power outputs.

Fig. 4 - Diffractograms of thin films manufactured in the sputtering system: a) copper; b) SiO_2; c) In_2O_3 deposited with 50W; d) In_2O_3 deposited with 110W.

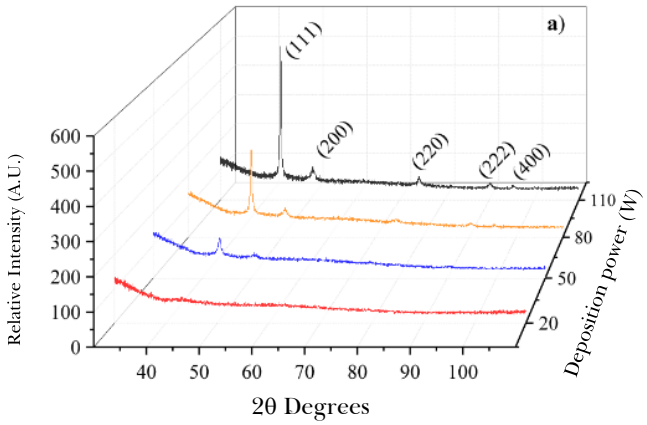

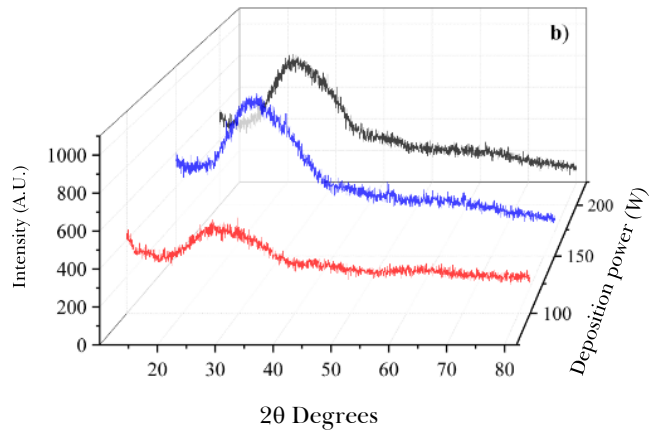

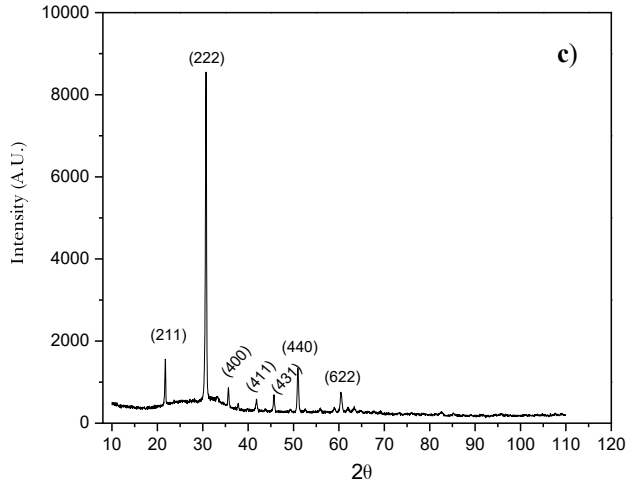

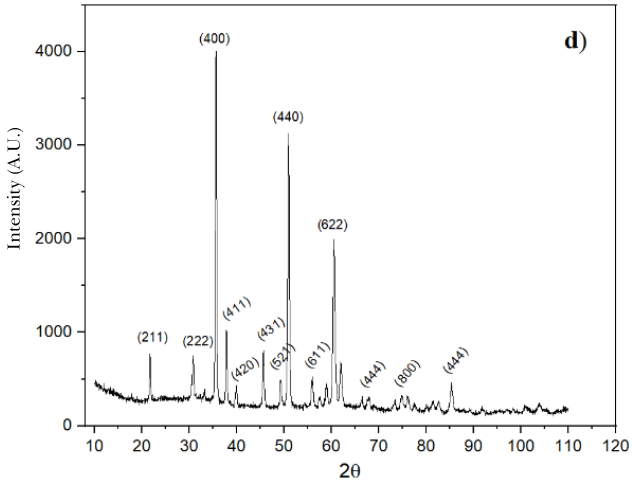

Figures 5 to 7 show atomic force microscopy (AFM) images of the deposited films surface. The roughness values obtained from the respective images are shown in Tables 5 to 7.

The AFM images show that the films are nanometric, and there is a small increase in grain size with power. This result is in accordance with the increase in crystallinity observed in Figure 4, for higher power outputs [12,13].

As for roughness, a small increase is observed in function of the deposition power, a fact that is related to the greater thickness of films deposited with higher power outputs.

Fig. 5 - AFM images of thin copper films deposited with: (a) 20W; (b) 50W; (c) 80W; (d) 110W.

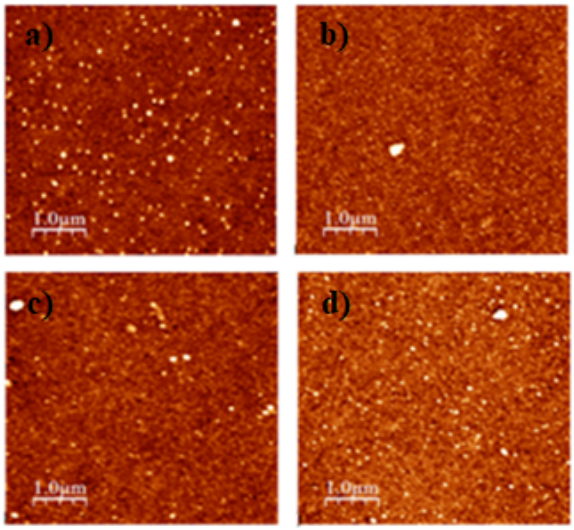

Fig. 6 - AFM images of thin SiO_2 films deposited with: (a) 100W; (b) 150W.

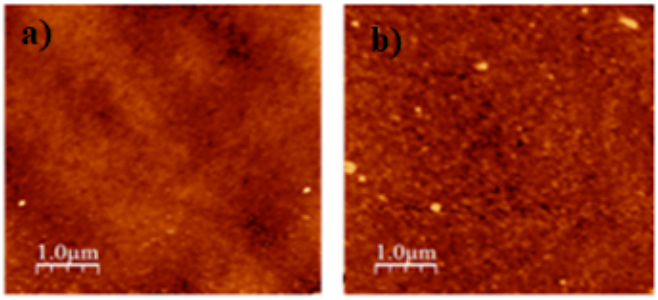

Fig. 7 - AFM images of thin films of In_2O_3 deposited with: (a) 50W; (b) 110W.

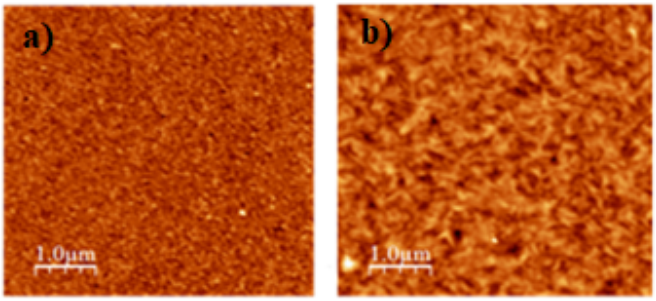

Table 5 - Roughness of thin copper films in function of deposition power.

POWER (W)	ROUGHNESS (nm)
20	1.58
50	1.71
80	1.85
110	1.36

Table 6 - Roughness of thin SiO_2 films in function of the deposition power.

POWER (W)	ROUGHNESS (nm)
100	0.65
150	0.94

Table 7 - Roughness of thin In_2O_3 films in function of the deposition power.

POWER (W)	ROUGHNESS (nm)
50	0.65
110	0.94

Figure 8 shows the variation in the resistivity of the copper and In_2O_3 films in function of the deposition power. The resistivity of the silicon oxide films was not measured, since the film was insulating. The measured values are in the same order of magnitude as the reported resistivity of the materials: 1.7 $\mu\Omega$.cm for copper [14], and 4.0 x 10^{-4} Ω.cm for In_2O_3 films [15, 16]. This result also contributes to attest to the good control of the deposition parameters in the assembled system.

The transmittance curves of SiO_2 and In_2O_3 films deposited in the different power outputs are shown in Figure 9. Since copper is a metal, the transmittance of the film was not measured.

By analyzing the transmittance spectra of In_2O_3 films, a variation in the position of the fundamental absorption edge of the films is observed in relation to the power. This result is well reported in the literature as a consequence of the formation of oxygen vacancies [17].

Analyzing the transmittance spectrum of the SiO_2 film deposited at 100W, it is noted that its behavior resembles the spectrum of silica with an absorbing edge at the end of the visible spectrum. This result is consistent with the amorphous characteristic of SiO_2 deposited with this power. However, the spectra of thin films produced at 150 and 200 W show that the fundamental absorption edges were extended to the near-ultraviolet region, which is a characteristic of SiO_2 crystalline (quartz). These results are consistent with the trend towards crystallization observed in the respective AFM images (Figure 6) of the films deposited with higher power outputs.

Fig. 8 - Electrical resistivity of thin films manufactured in the sputtering system in function of deposition power: a) copper; b) In_2O_3.

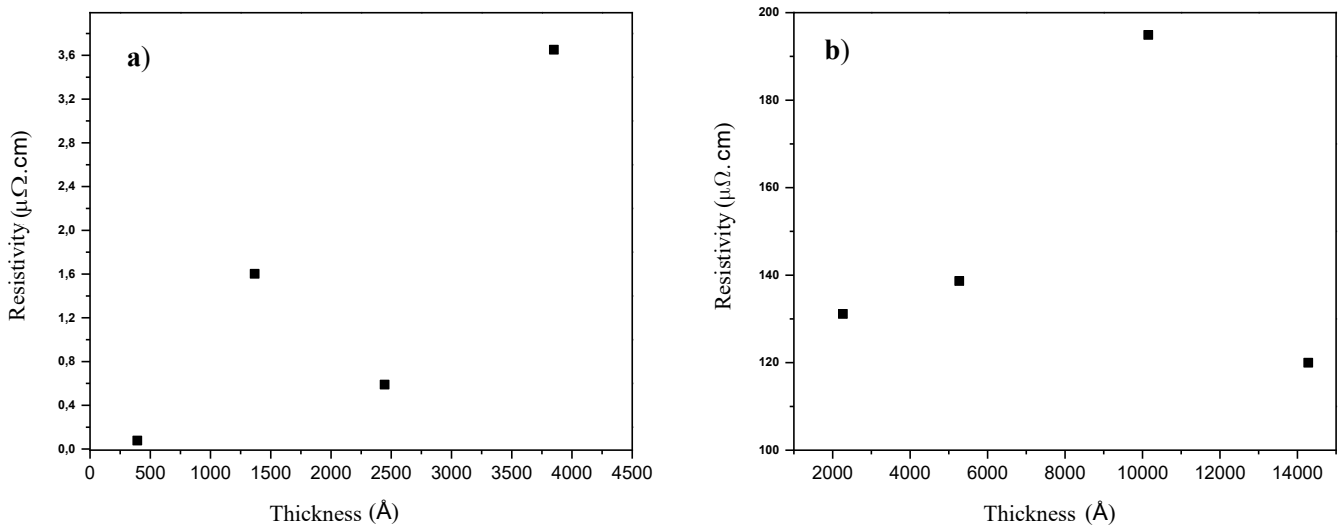

Fig. 9 - Transmittance spectra of thin films manufactured in the sputtering system at different power outputs: a) In_2O_3 thin films; b) SiO_2 thin films.

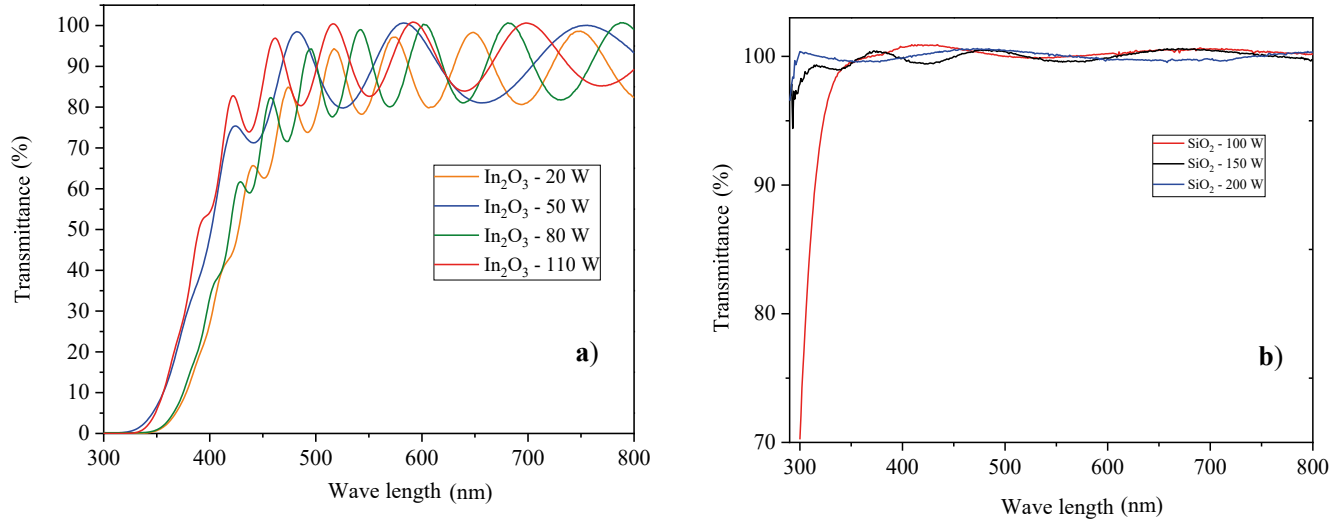

4 Conclusions

A radio frequency magnetron sputtering system was designed and assembled for the manufacture of thin films. This system is operational on the LFF-IME installations, having already performed more than 60 deposition cycles. The depositions of the three targets with different characteristics (conductor, semiconductor, and insulator) provided films of good quality, good thickness uniformity, and properties similar to those reported in the literature. The deposition rate of films varied linearly in relation to work power. These experimental results attest that the assembled system provides good control of deposition parameters.

Acknowledgments

The authors thank the War Arsenal of Rio de Janeiro (AGR) and the Mechanical Workshop of the Brazilian Center for Research in Physics (CBPF) for their readiness in modeling and machining for the assembly of the deposition system. The authors also thank the Materials Division of the National Institute of Metrology, Standardization and Industrial Quality (INMETRO), which collaborated for the characterization of the manufactured films, and the Coordination for the Improvement of Higher Education Personnel (CAPES), for the financial support.

References

[1] KELLY, P. J.; ARNELL, R. D. Magnetron sputtering: a review of recent developments and applications. Vacuum, Amsterdam, v. 56, n. 3, p. 159-172, 2000.
[2] GÜRAKAR, S.; HORZUM, T. Serin, Variation of structural and optical properties of TiO2 films prepared by DC magnetron sputtering method with annealing temperature, Materials Science & Engineering B, 262. Ancara: Universidade de Ancara, 2020.
[3] DEPLA, K.; STRIJCKMANS, R. de G. The role of the erosion groove during reactive sputter deposition, Surface & Coatings Technology, [s. l.], v. 258, p. 1011-1015, 2014.
[4] CRUZ, L. R.; LOPES, B. F. M.; MEDEIROS, R. A.; LIMA, R. M. C.; FERREIRA, C. L. Propriedades de filmes finos de ZnO:Al depositados sobre substratos de poliimida à temperatura ambiente para aplicações em dispositivos optoeletrônicos flexíveis. Cerâmica, [s. l.], v. 63, n. 366, p. 162-168, 2017.
[5] HELL, J.; HORKEL, M.; NEUBAUER, E.; EISENMENGER-SITTNER, C. Construction and characterization of a sputter deposition system for coating granular materials. Vacuum, Amsterdam, v. 84, 453–457, 2010.
[6] SINGH, M. M.; VIJAYA, G.; KRUPASHANKARA, M. S.; SRIDHARA, B.K.; SHRIDHAR, T. N. Deposition and Characterization of Aluminium Thin film Coatings using DC Magnetron Sputtering Process. Materials Today: Proceedings, Amsterdam, v. 5, n. 1, p. 2696-2704, 2018.
[7] BHORDE, A. et al. (400)-Oriented indium tin oxide thin films with high mobility and figure of merit prepared by radio frequency magnetron sputtering, Thin Solid Films, [s. l], v. 704, p. 137972, 2020.
[8] KARTHIKEYAN, S.; HILL, A. E.; PILKINGTON, R. D. The deposition of low temperature sputtered IN2O3 films using pulsed d.c. magnetron sputtering from a powder target. Thin Solid Films, [s. l], v. 550, p. 140-144, 2014.
[9] SCHURIG, P.; COUTURIER, M.; BECKER, M.; POLITY, A.; KLAR, P. Optimizing the Stoichiometry of Ga2O3 Grown by RF-Magnetron Sputter Deposition by Correlating Optical Properties and Growth Parameters, Phys. Status Solidi A, [s. l], v. 216, 1900385, 2019.
[10] MELLO, A. Filmes finos cristalinos de hidroxiapatita: Uma abordagem original com magnetron sputtering de Alvos Opostos. 2007. Tese (Doutorado) - Instituto Militar de Engenharia, Rio de Janeiro, 2007.
[11] CHOI, K H.; KANG, H. C. Structural and optical evolution of Ga2O3/glass thin films deposited by radio frequency magnetron sputtering. Materials Letters, [s. l], v. 123, p. 160-164, 2014.
[12] AMALATHAS, P.; ALKAISI, M. Effects of film thickness and sputtering power on properties of ITO thin films deposited by RF magnetron sputtering without oxygen. Journal of Materials Science: Materials in Electronics, [s. l], v. 27, 2016
[13] THILIPAN, G.; RAO, A. Influence of power on the physical and electrical properties of magnetron sputtered gadolinium oxide thin films for MOS capacitors. Materials Science in Semiconductor Processing, v. 121, 105408, 2021.
[14] QUADROS, H. B. Avaliação das características resistivas de filmes finos absorvedores de radiação eletromagnética. 2014. Trabalho (Conclusão de Curso em Engenharia Aeroespacial) - Universidade Federal de Santa Catarina, Santa Catarina, 2014.
[15] BERRY, P. M.; HALL, M. T. Thin films technology. New York: Van Nostrand Reinhold Company publication, 1968.
[16] CRUZ, L. R. et al. Análise comparativa das propriedades de óxidos transparentes condutores para aplicação em células solares de filmes finos de CdTe. Matéria, v. 22, n. 1, e11793, 2017.
[17] KALEEMULLA, S.; REDDY, A. S.; UTHANNA, S.; REDDY, P. S. Physical properties of In2O3 thin films prepared at various oxygen partial ressures, Journal of Alloys and Compounds, [s. l.], v. 479, n. 1–2, p. 589-593, 2009.

VOL.40 Nº3 2023
https://doi.org/10.22491/rmct.v40i3.11766.en

Impacts of airport closure due to weather conditions on flight delay and CO_2 emission costs

Reinaldo Moreira Del Fiaco[1], Marcelo de Miranda Reis[1] e José Carlos Cesar Amorim[1]
[1]Instituto Militar de Engenharia (IME)
Praça General Tibúrcio, 80, 22290-270, Praia Vermelha, Rio de Janeiro, RJ, Brasil
***reinaldo.moreira@ime.eb.br**

ABSTRACT: The costs of congestion or delay for airlines and passengers directly impact the means necessary for the resilience of operations and arrival at the destination. They also directly affect the emission of polluting gases caused by aircraft in the terminal control area where the airport is located. Climate predictions show a trend of worsening weather conditions favorable to air operations. This article aims to develop a method for identifying operational bottlenecks and calculating the time aircraft spend in a specific airspace control area during adverse weather conditions. For this purpose, data collected through the ADS-B system and airspace division published on navigation charts will be used. In addition, the article includes a bibliometric study to identify the most used keywords in the literature review. Finally, an analysis of additional CO_2 emissions caused by operational delays will be performed. In the case of the terminal area of Viracopos Airport in Campinas/SP, the results show that the waiting time resulted in 52 minutes more time that the aircraft remained in the airspace or 9.27 tons of additional CO_2 emitted due to flight delays and cancellations.

KEYWORDS: Air Traffic Control. ADS-B. Operational Efficiency. Flight Delay. Emissions.

RESUMO: Este artigo aborda os impactos do congestionamento e atrasos em voos comerciais, tanto para as empresas aéreas quanto para os passageiros. Além disso, destaca a relação direta entre esses custos e as emissões de gases poluentes causados pelas aeronaves na área de controle terminal em que o aeroporto está localizado. Com o objetivo de identificar gargalos operacionais e calcular o tempo de permanência das aeronaves durante condições meteorológicas adversas, o artigo propõe um método que utiliza dados coletados por meio do sistema ADS-B e cartas de navegação. O estudo também inclui uma análise bibliométrica para identificar as palavras-chave mais utilizadas na revisão bibliográfica do estudo. Por fim, é feita uma análise da emissão adicional de CO_2 causada pelos atrasos operacionais. Como exemplo, o estudo analisa a área terminal do Aeroporto de Viracopos em Campinas/SP e mostra que o tempo de espera resultou em 52 minutos a mais no tempo em que as aeronaves permaneceram no espaço aéreo ou 9,27 toneladas de CO_2 a mais emitido devido ao atraso e cancelamento dos voos. O método proposto pode ser utilizado para identificar áreas que requerem atenção para garantir a segurança e a eficiência do tráfego aéreo, especialmente em condições meteorológicas adversas.

PALAVRAS-CHAVE: Controle do Espaço Aéreo. ADS-B. Eficiência Operacional. Atrasos de Voos. Emissões.

1. Introduction

On an airway, capacity is restricted when there is an increase in traffic density. Scarpel and Pelicioni [1] state that, across the globe, the increase in aircraft movement is reaching airports' demand absorption capacity. Even after the covid-19 pandemic, the International Air Transport Association (IATA) [34] expects that by the end of 2023 the global movement of aircraft will have reached 103% of traffic compared to 2019. And the situation of operational capacity worsens when there are restrictions due to weather conditions, which is a trend for this decade, according to Lui *et al.* [22].

The cost of this congestion or delay for airlines and passengers directly affects the means necessary for the resilience of operations and arrival at destination [1].

The Air Force Command Instruction (ICA) 100-12 Rules of the Air defines a Terminal Control Area (TMA) as a Controlled Airspace in which, within its dimension, the Air Traffic Service (ATS) of approach and arrival is provided for aircraft in the vicinity of one or more aerodromes [30]. In Brazil, this is managed by the Department of Airspace Control (DECEA), an agency linked to the Air Force Command and the Ministry of Defense. The difficulty of controlling a TMA is that aircraft are flying low, with low speeds, close to each other, performing different types of procedures and on different routes, which causes an increase in the workload of the flight controller and in the pilots' attention. Finally, when there is bad weather or other event of operational disruption at the aerodrome(s) of the TMA immediacy [25], this means

the aircraft will be receiving air traffic control for a longer period, being in the so-called waiting procedure or reducing the speed, thus increasing several operational costs, one of them being the emission of polluting gases.

There are several studies related to performance optimization of the Brazilian Airspace Control System (SISCEAB), as well as of other countries, aimed at developing more direct routes and at sector demand (capacity), concerning care to avoid residential areas that increase noise pollution, predictability, training, technical infrastructure, operational safety, and cost-benefit ([3], [4], [1], [4], [6], [10], [11], [14], [16], [18], [19], [28], [29]). Air Traffic Control is, therefore, a widely debated topic, mainly due to a set of rules and circumstances that further increase the complexity of air transport, and that worsen when they encounter conditions not controlled by man, such as meteorological conditions.

On the other hand, there is still a difficulty in obtaining data, and in the quality of data offered on aircraft movement. Airlines interested in optimizing their operational network and, consequently, in reducing costs, invest in *Flight Operational Quality Assurance* (FOQA), generally applied within the engineering sector, which covers a set of monitoring, analysis, and simulation methods with data obtained from *Flight Data Recorders* (FDR) ([40], [41]). However, the data obtained are mostly used to forecast maintenance and operational safety expenses, and are not shared since such information could be used by other companies in statistical modeling to obtain advantages over the pricing of their airline tickets [41]. Specifically, the Makron Platao® *software* from Atech®, one of the companies of Embraer™ Group, responsible for supplying the systems that serve the Brazilian Airspace Control, can simulate several scenarios for training purposes, but not to identify from a real scenario the time of delays and other statistical information. In addition, data obtained by the Sagitario® air traffic control system are not available, serving for tactical use and reporting to verify the congestion capacity and post-operational saturation of the Air Navigation Management Center (CGNA) [42]. The National Civil Aviation Agency (ANAC) provides information on the percentage of flight delay and cancellation, based on the scheduled flight start time, actual flight start time, scheduled landing time, and actual landing time [35], without information on the route, at what time of the flight there was an operational delay and aircraft performance.

Publicly available is the capture of flight data (*timestamp*, UTC time, *callsign*, position, altitude, speed, and direction) that are transmitted through devices of an *Automatic Dependent Surveillance-Broadcast* (ADS-B) system coupled to commercial aircraft and a few general aviation aircraft. These data can be obtained by self-developed receivers or through companies that market this information, such as FlightRadar24™ and FlightAware™.

Given this, there is an opportunity to develop a method for verifying operational bottlenecks and the length of stay of aircraft in a given airspace control area, using data obtained through ADS-B and the division of airspace published in navigation charts, when there are bad weather conditions, which is the objective of this article. In addition, a bibliometric study is presented through a simultaneous occurrence analysis, to verify which are the most used keywords and their relationships in the literature review for this study. Finally, it will also be analyzed what is the additional CO_2 emission caused due to operational delays. Pejovic *et al.* [10], in their study on London Heathrow Airport, also attest to the lack of weather closure information from the aerodrome or the English regulatory agency.

The study will be applied in the terminal area of Viracopos Airport, in Campinas/SP, which is the fourth airport in Brazil with the highest number of landings and takeoffs, as it is a relief and alternative airport in Congonhas, Guarulhos, and Belo Horizonte. In addition, in the last 5 years (2017-2022) flights from destinations to SBKP averaged 5,000 flights per month, and with an average of delays of more than 30 minutes of 6.05%, delays of more than 60 minutes of 2.52%, and average cancellations of 3.23% [35].

Finally, the congestion of the Airspace, whether due to weather conditions or any other reason, also

implies the cost of defense that will require investment in personnel and modernization of procedures and materials for the re-balancing of the sector, as happened in the event that became known as the 2006 Air Blackout [39].

2. Bibliographic review

2.1 Bibliometric review

According to Carvalho *et al.* [16], flight delays return significant economic problems to society, hence the frequency of this theme in the scientific literature on air transport and the need to carry out a systematic review on the subject.

From the term *weather conditions affect airports operation* on the ScienceDirect® database, 5,377 results related to research articles were found, of which 400 were analyzed for this literature review. Of these, through an empirical analysis of the authors, 28 ([1], [3], [4], [5], [6], [7], [8], [9], [10], [11], [12], [13], [14], [15], [16], [17], [18], [19], [20], [21], [22], [23], [24], [25], [26], [27], [28], [29]) are correlated to the objective of this research. A bibliometric review was carried out, with analysis of co-occurrences, using VOSviewer®. This software allows for the visualization of relationships of the keywords in these publications, so that this bibliographic review could be guided by the use of these results in the research.

For Marques *et al.* [2], concurrency analysis is a quantitative method of cataloging keywords based on graph theory, with a set of objects that are repeated in different sources.

With this software, two visualizations were extracted and 79 relationships between keywords were generated, in 6 sets. Figure 1 shows the result of this analysis with the network visualization.

In set 1 are the keywords *airport*, *aircraft engines*, *air pollutants*, *aviation emissions*, and *air quality*, in which the word that is most repeated in 'with' searches is *airport*; therefore, this word is the most common among these keywords, as well as among all keywords of the bibliographic reference. In set 2, the most repeated keyword is *climate change*, which is related to the words: *airport closure*, *London Heathrow*, *weather delay*, *sustainable development*, and *disaster risk*. In set 3, *resilience* appears as the most repeated and is related to *severe weather event*, *aviation*, *modal substitution*, and *delay*. In set 4, the word that occurs the most is *risk assessment*, related to *urban clusters*, *China*, *location selection*, and *environmental risks*. In set 5, the word *efficiency* appears together with *performance*, *seaport*, *privatization*, and *developing countries*. Finally, in set 6 is *disruptive weather*, with the keywords *sea-level rise* and *adaptation*.

Figure 1 - Results of keyword occurrences.

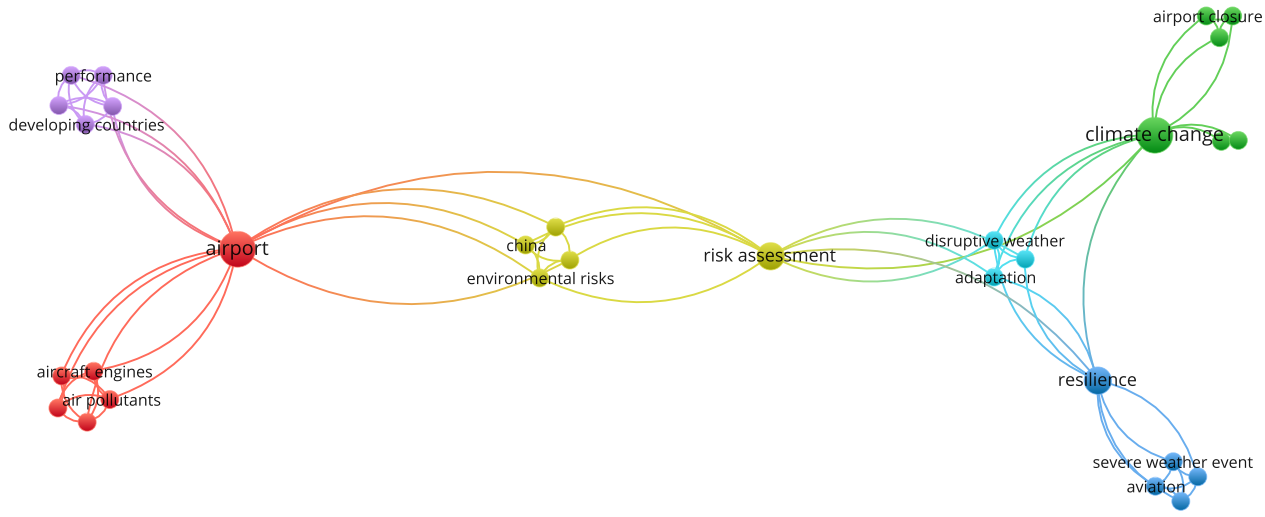

Figure 2 shows the results of occurrence visualization by overlap, in which keywords are shown according to the year they were found in publications. This shows that words related to weather, air quality, and resilience are more recent.

Carvalho *et al* [16] conducted a systematic review on the relevance of flight delay research, identifying the main methods used among 123 articles. It was found that, between 2001 and 2013, the use of descriptive statistics and regression models was more applied. From 2013 to 2017, network analysis methods began to be applied. And from 2017 to 2019, more studies using machine learning were identified. These authors conclude that there is a trend towards the evolution of hybrid models for prescriptive and predictive analysis of air transport.

2.2 Operational effects during adverse weather conditions

Airport congestion is caused by poor weather conditions, lack of airport infrastructure capacity, increased demand for air transport, and time lost waiting between landing and takeoff procedures [1] [4] [16] [10].

A good practice of the agency that provides air traffic service is to make a daily analysis of the forecast of weather conditions and air traffic movement. This practice is called *Early Warming Model* (EWM) in the literature [1] [17] [18]. In Brazil, such practice is part of the Air Traffic Flow Management, provided by the Air Navigation Management Center (CGNA) of the Airspace Control Department (DECEA) [31]. The EWM consists of a regression analysis that projects the number of daily movements so that measures are taken, such as the number of personnel employed in air traffic control and airports, and the flight crew schedule at airports where the weather will be bad and those that can receive flights as an alternative.

Postorino *et al* [4] used discrete event simulation models, based on the AnyLogic™ *software*, to estimate unexpected events, in magnitude and duration, that affect the operations of an airport, evaluating the dynamics of each process and its impact within the transport system, which is dynamic and stochastic. The authors describe the dynamics of air transport in two layers. The first would be an isolated activity, with a certain performance; whereas the second would be the *output* of the first layer, connecting the whole system and showing how a propagation of efficient and inefficient activities are part of the results which, in themselves, represent the system.

As a case study, the authors used the airport in Bologna, Italy. With a capacity of 24 movements per hour, open 24 hours, this airport receives an average of 107 landings and 109 departures per day.

The study considered the arrival and departure of 20 flights per hour, taking actual data from FlightRadar24™, and considered the airport's capacity in relation to the number of stairs; catering, water, cleaning, fuel, and luggage transport trucks, and pushback tractors, so to discover the number of flights that would be delayed, the total and average delay for takeoff, and the variation in time between arrival and departure of the aircraft at the airport. As a result of 20 rounds of random simulation, the authors found that, with the different disruption events, 50% of flights would depart with a delay, 11.5% would depart with more than 1.5 hours of delay, and one aircraft would depart with more than 4 hours of delay. The authors suggest that new studies can estimate the environmental impact of CO_2 and noise emissions, and how this impact would be felt by different stakeholders.

To make weather forecasting at airports more accurate, Larraondo *et al* [7] developed a new method of analysis with machine intelligence through Numerical Weather Prediction (NWP). The algorithm for his model was developed in Python and is available as a free software in the author's GitHub™ repository (https://github.com/prl900/AeroCirTree).

This system makes use of the National Oceanic and Atmospheric Administration (NOAA) database, seeking weather information from the Global Forecast System and the METAR Code database distributed by the WMO Global Telecommunication System (GTS). As a scenario, they used the airports of Berlin Tegel (EDDT), Heathrow (EGLL), Barcelona (LEBL), Charles de Gaulle (LFPG) and Milano Malpensa (LIMC), using 8,760 METAR information from each airport in the years

2011, 2012 and 2013. To compare the method effectiveness, they used linear prediction models and the circular regression tree model, known as Lund Method. Results show the method proposed by Larraondo *et al* [7] is more effective in the long term, and the linear method is more effective in the short term, adjusting to small variations in the long term; on the other hand, the Lund Method in the medium term is more advantageous than the machine learning created by the authors for the accuracy of weather forecasting at airports.

Figure 2 - Result of keyword occurrences by year of publication.

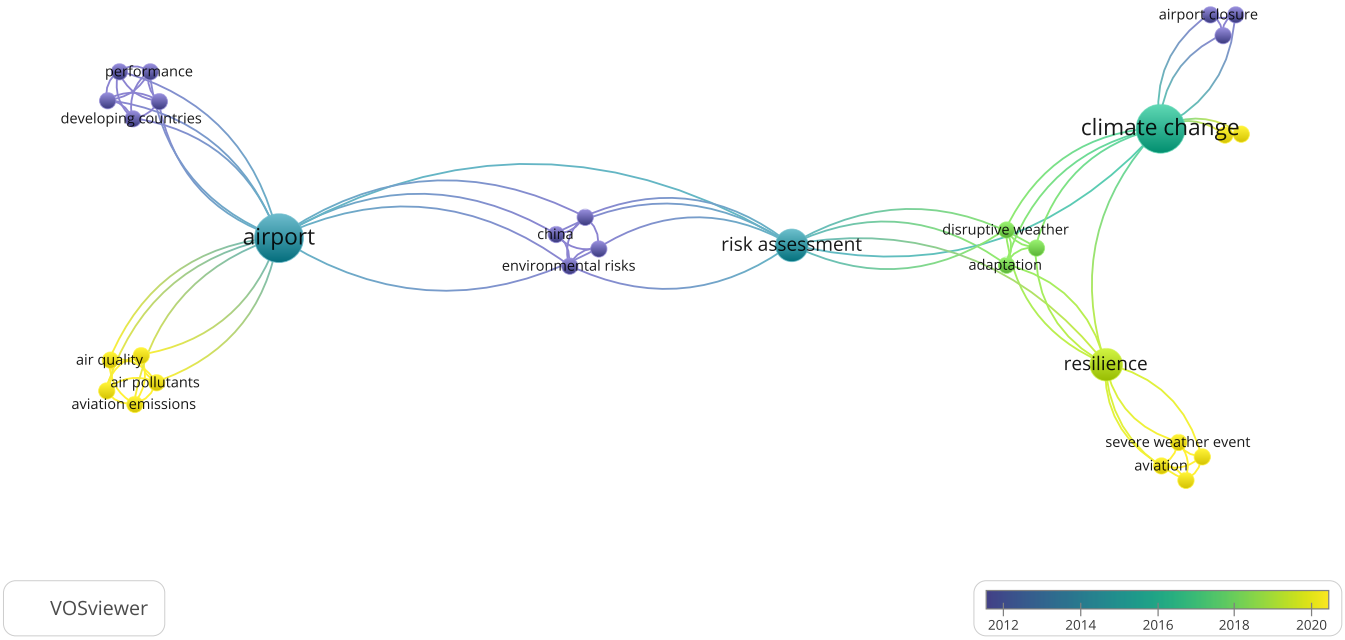

To find the meteorological impact on the performance of landings for domestic flights in Brazil, Oliveira [11] used the history of planned and performed flights, meteorological data and estimated by a logit model to analyze how the various weather conditions affect the probability of flight delays. Results show that there is significant evidence about the delay of flights due to weather events, but visibility and ceiling conditions resulted in a negative coefficient, while conditions such as rain and wind gusts are more significant for delays.

3. Method

3.1 Obtaining aerodrome closure time information

To achieve our goal, the first step is to find out at what times the airport was closed due to adverse weather conditions. Through the REDEMET API, a DECEA weather information service [32], it is possible to obtain the history of the METAR Code, which provides information on day, date, time, airport, wind speed and intensity, vertical visibility, cloud cover and cloud height, present weather, present weather phenomena, air temperature and dew point phenomena, and on-site atmospheric pressure in hPa. The following is an example of a METAR Code from Viracopos Airport (SBKP), in Campinas/SP. Decoding is done through ICA 105-16 [33].

2022081003 - METAR SBKP 100300Z 02008KT 7000 -RA BKN007 OVC013 18/17 Q1017=

In the METAR code shown, the information is August 10, referring to 3 hours in Greenwich Mean Time (Z), the wind is 020° with 08 kt of intensity, visibility of 7,000 feet, with decreasing rain (-RA), cloudy (BKN)

at 700 feet, covered (OVC) at 1,300 feet, with air temperature of 18°C and dew point temperature of 17°C, and the pressure to adjust the altimeter is 1017 hPa.

To find out the hours when the airport was closed and to make the descriptive statistics of the sum of these results, an algorithm was developed in Python (see appendix) that informed the time (timestamp) when the aerodrome did not operate in Visual Flight Rule (VFR), Special VFR, procedures under Instrument Flight Rule, ILS operation, LNAV, LNAV (Performance A and B), LNAV (Performance C and D), and RNP 0.3. The restriction of visibility for each of these types of procedures depends on air traffic standards and what is published in the approach and takeoff charts of each aerodrome.

3.2 Airspace delimitation and flight data

According to Campos [37], for statistical sampling in transport surveys, the best day of the week to be observed is Thursday. Thus, this was the day chosen for the calculations, after obtaining the results of the aerodrome closure times. From then on, the files in kml and csv for each flight performed on a Thursday would be obtained on the FlightRadar24™ platform. These files provide information on timestamp, UTC time, callsign, altitude, speed and direction, and it is then possible to calculate the time traveled by the aircraft at the entrance of the TMA area until the final approach of the runway.

DECEA [34] publishes data of the Repetitive Flight Plans, in which the scheduled flights for a given day are shown. With this information, the flights scheduled on a day when the aerodrome was not closed due to meteorological reasons were compared with a day when it was closed, thus allowing for the estimate of time difference for aircraft length of stay until exit of terminal area, after takeoff, or until landing.

The airspace boundaries in csv format were obtained from the GEOAISWEB directory, which is maintained by DECEA. Alternatively, it could be obtained through a Letter of Route (ENRC). Having the coordinates of the area vertices and the altitudes in relation to sea level, one could reproduce the geographical space through the second algorithm developed (see repository https://github.com/embarquetec/adatfm).

This algorithm imports the flight path and identifies the moment when the aircraft passes through one of the edges of the generated map. Then, the time flown between each zone of the airspace is subtracted. Figure 3 shows the airspace boundaries and flight trajectory. Table 1 shows the outputs generated to determine the time at which the aircraft passes through each zone of airspace or phase of flight, e.g., takeoff, cruise, descent, and landing. The results also show an error, which is a correction for more that corresponds to the time for the capture of aircraft position information by the Automatic Dependent Surveillance – Broadcast (ADS-B) system – and the confirmation of the aircraft position. These time points are subtracted from the total time.

Figure 3 - Reproduction of the airspace limitation with the flight path of the aircraft.

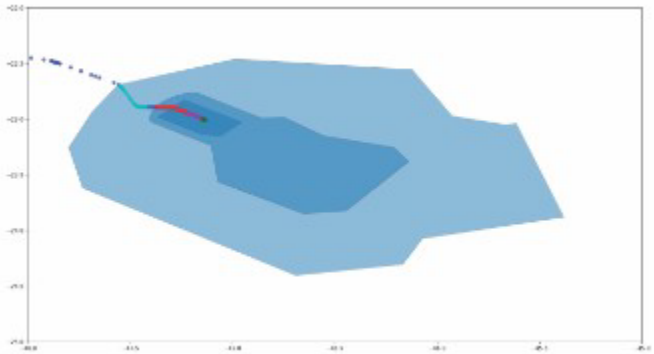

Table 1 - Flight identification outputs

Outputs	Description
code	IATA Flight Identification Code
departure_iata	Departure airport IATA code
arrival_iata	Destination Airport IATA Code
takeoff_time	Departure time

Outputs	Description
takeoff_time_error	Takeoff time error
level_off_time	Time it reaches cruise level
level_off_time_error	Error of the time when it reaches the cruise level
descent_init_time	Time when the descent of the cruise phase begins
descent_init_time_error	Error of the time when the descent of the cruise phase starts
touchdown_time	Time of landing
touchdown_time_error	Landing time error
flight_time	Total flight time
flight_time_error	Total flight time error
before_takeoff_ground_duration	Time the aircraft remained on the ground prior to takeoff
before_takeoff_ground_duration_error	Time the aircraft remained on the ground prior to takeoff
climb_duration	Climb duration time
climb_duration_error	Climb duration time error
cruise_duration	Cruise flight time duration
cruise_duration_error	Cruise flight time duration error
descent_duration	Descent duration
descent_duration_error	Descent duration time error
after_landing_ground_duration	Taxi time after landing
after_landing_ground_duration_error	Taxi time after landing error

Outputs	Description
air_space_1_entry	Airspace Entry Time
air_space_1_entry_error	Airspace Entry Time Error
air_space_1_exit	Airspace Departure Time
air_space_1_exit_error	Airspace departure time error
inside_ air_space_1	Time within airspace
inside_air_space_1 error	Time within airspace error
total_time_inside_air_space	Flight time within selected airspace sections
total_aircraft_fuel_inside_air_space	Total fuel within the selected airspace
total_passenger_CO2_inside_air_space	Total CO_2 emitted within the selected airspace
total_cost_CO2	Total cost of CO_2 emitted according to the current quotation

To find the total cost of CO_2 emitted according to the current price, the market value of BRL 383.62 per ton is used, considering the closing of the futures market on November 1, 2022 [38].

3.3 Calculation of pollutant emissions

The calculation of CO_2 emission uses the International Civil Aviation Organization (ICAO) API [38] for the calculation of the individual passenger emission. This method uses a fixed variable multiplying by the total fuel with the passenger load factor divided by the number of seats for the economy category (Y) with the passenger quantity factor stipulated for each continent.

$$CO_2 per\ pax = 3{,}16\ \text{x}\ \frac{(tf\ x\ pfc)}{(nys\ x\ plf)} \quad (1)$$

Wherein:
= Total fuel;
= Load factor for passenger;
= Number of seats for category Y;
= Passenger quantity factor by region.

The values of the total fuel consumed in each section flown are obtained through the return of the ICAO API [38]. For this, the average of the history of all flights of the airlines that pass this information to the ANAC Database is used.

4. Case Study

The scenario chosen was that of Campinas/Viracopos International Airport (SBKP). Campinas is the fourth airport in Brazil with the highest number of landings and takeoffs, with 109,230 movements recorded at the end of 2022, losing to Guarulhos (192,280 movements), Congonhas (130,820 movements) and Brasília (117,736 movements) [36]. The city of Campinas is located in a mountainous region, in addition to the Capivari, Jaguari, Capivari-Mirim and Atibaia rivers, which favor the conditions for the formation of a cluster of water droplets that are suspended in the atmosphere. It is this fog that restricts visibility for landings and takeoffs, causing delays and cancellations.

According to ANAC data [35] of percentages of delayed and canceled flights originating in SBKP from December 2017 to September 2022, there are, on average, 5,027 flights per month, with an average delay of more than 30 minutes of 7.03%, with delays of more than 60 minutes of 2.36%, and with an average cancellation of 2.81%. Regarding flights from destinations to SBKP, we have an average of 5,000 flights, with an average of delays of more than 30 minutes of 6.05%, delays of more than 60 minutes of 2.52%, and an average of cancellations of 3.23%.

4.1 Aerodrome closure data

Table 2 shows the restrictions by cloud ceiling and visibility for the operation by flight rule and type of procedure.

Table 2 - Operating conditions by flight rule and procedure for Viracopos Airport

Procedures	Conditions
VFR	Ceiling > = 1,500 ft
	Visibility > = 5,000 ft
Special VFR	Ceiling > = 1,000 ft
	Visibility > = 3,000 ft
ILS	Ceiling > = 200 ft
	Visibility > = 800 ft
LNAV	Ceiling > = 357 ft
	Visibility > = 1,100 ft
LNAV (Performance A and B)	Ceiling > = 430 ft
	Visibility > = 800 ft
LNAV (Performance C and D)	Ceiling > = 430 ft
	Visibility > = 1,500 ft
RNP 0.3	Ceiling > = 339 ft
	Visibility > = 1,000 ft
RNP 0.15	Ceiling > = 339 ft
	Visibility > = 800 ft

September 15 and 22, 2022 were stipulated. Table 3 shows the number of hours the aerodrome did not operate for each type of procedure.

Table 3 - Time that each procedure remained unavailable for operation

Procedure	Time (hr) day 09/15	Time (hr) day 09/22
VFR	00:00	18:00
Special VFR	00:00	08:33
ILS	08:00	04:48
LNAV	00:00	03:00
LNAV (Performance A and B)	00:00	03:33
LNAV (Performance C and D)	00:00	03:33
RNP 0.3	00:00	3:00
RNP 0.15	16:00	21:12

4.2 Airspace delimitation and flight data

For landing and takeoff procedures at Viracopos Airport, the aircraft pass through CTR Campinas (3), TMA São Paulo 2 (2) and TMA São Paulo 1 (1). Figure 4 shows the sections of the air spaces delimited for this study.

Figure 4 - Delimitation of the airspace of the study.

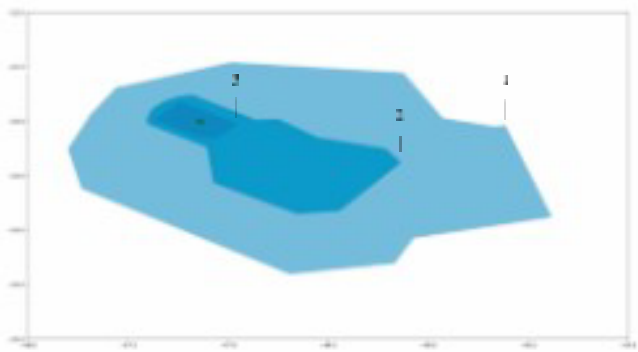

Within this delimitation, we have the *Standard Terminal Arrivals* (STAR) procedures entitled RNAV LOLED 1A (Figure 5), RNAV TIMRU 3B – UTLOT 3B (Figure 6) and RNAV VURAV 2A (Figure 7).

Figure 5 - STAR RNAV LOLED 1A procedures.

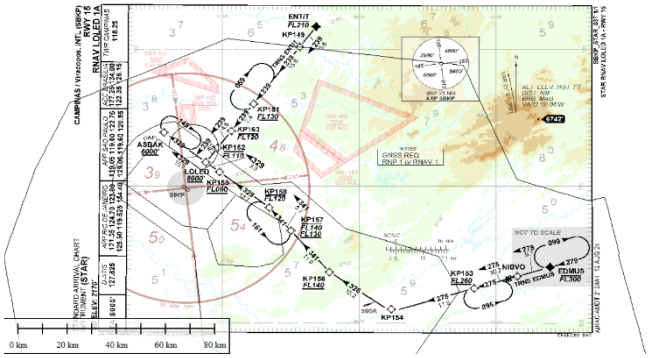

Figure 6 - STAR RNAV TIMRU 3B – UTLOT 3B Procedure.

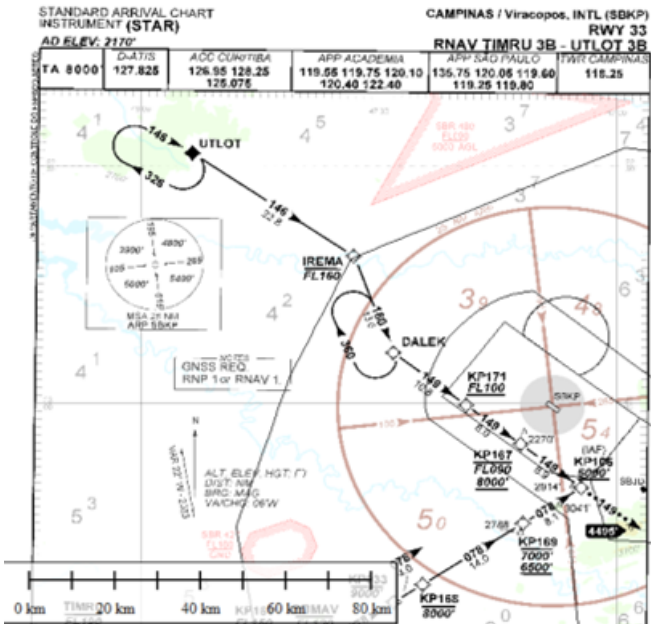

From the analysis of the DECEA Repetitive Flight Plans database and the FlightRadar24™ flight database, the same flight numbers and respective routes were segregated for comparison. There were 44 flights analyzed (AD4025, AD4276, AD4385, AD4942, AD4326, AD2942, AD2874, AD4047, AD4099, AD4708, AD4242, AD4386, AD2954, AD4027, AD4638, AD4310, AD4871, AD4555, AD2030, AD4805, AD2953, AD2021, G31771, AD4449, AD4033, G31712, AD4885, AD4285, AD4341, AD4361, AD4853, AD4872, AD4451, AD2740, AD4356, AD4789, AD4424, AD2697, AD4034,

AD2824, AD4340, AD2736, AD4763, AD4322). Of these, no flights were delayed on 09/15 and 6 flights were delayed on 09/22, and no flights were diverted to another airport.

Figure 7 - STAR RNAV VURAV 2A procedure.

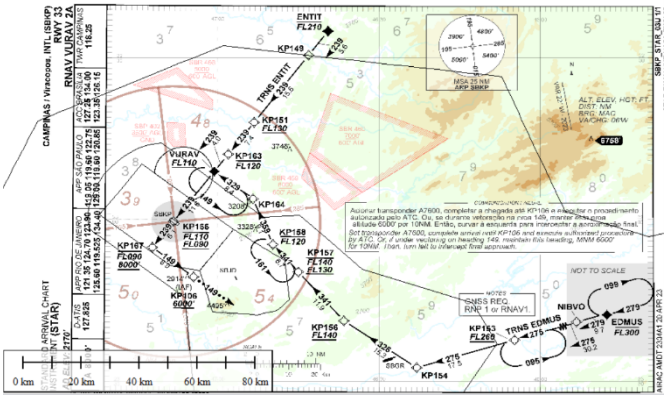

4.3 Application result

Figure 8 shows the route of flights with delays. In it, one can observe the orbit procedures that generated the delay. The time for each orbit procedure depends on the performance of the aircraft, but each leg of the procedure takes around 1 minute, and should consider the time for the aircraft to enter the procedure and other deviations. The darker the color of the route, the longer the aircraft were on that path.

The figure shows that, in the area of TMA São Paulo 1, the most congested areas are at the limits of the terminal, mainly in the orbit procedure on the DALEK fixed (*see* Figure 6) with 00:30:53 h and 13 aircraft, and in the orbit of the KP151 fixed (see Fig. 2) with 00:12:52 h and 3 aircraft.

Table 4 shows the total flight hours per day, within each airspace, and the sum of the flight hour. The difference between the routes between the day that there was no delay and the day that there was an extra flight was 00:52:29.

Figure 8 - Compiled flights on 09/22.

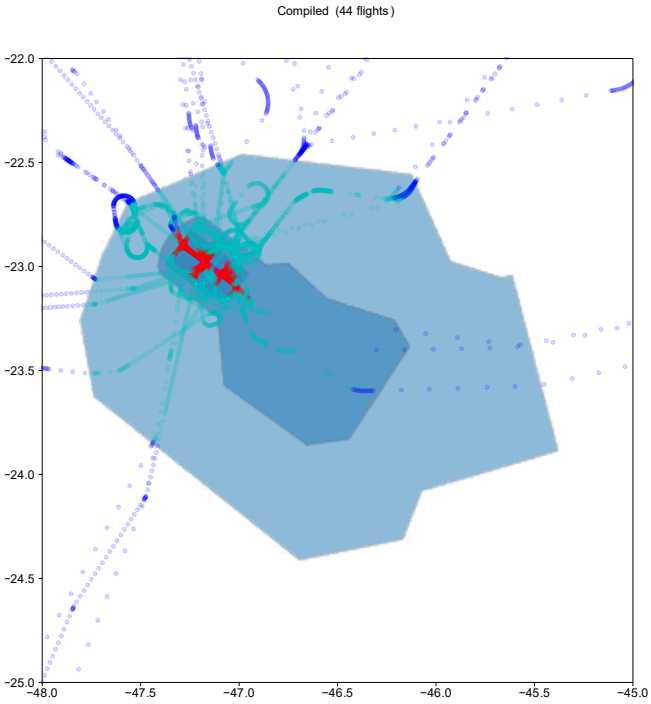

Table 4 - Flight time within each section of airspace

Outputs	Time (hr) day 09/15	Time (hr) day 09/22
inside_tma_sao_paulo_1	06:49:21	07:05:35
inside_tma_sao_paulo_1_error	00:25:39	00:29:38
inside_tma_sao_paulo_2	00:55:01	01:13:34
inside_tma_sao_paulo_2_error	00:00:11	00:00:14
inside_ctr_campinas	00:43:13	01:07:01
inside_ctr_campinas_error	00:13:04	00:15:24
total_time_inside_air_space	07:48:41	08:41:10

4.4 Result of pollutant emission

According to the ICAO manual [38], flights within the South American continent are considered 82.6% and 77.27%. On the verified routes, the aircraft used are the A76, A32N, 73G and E95 models, for the A76 the occupancy of 53 passengers is considered, and for the other aircraft, 87 passengers are considered. The total fuel spent on each flight leg was obtained through the ANAC database.

Table 5 shows the result in which the delays identified in the sample generated the consumption of 9,278.74 kg/CO_2 more emitted into the atmosphere and with a cost of BRL 3,559.47 more in the used quotation of tons of CO_2.

Table 5 - Total emission in kg/CO_2 and cost

Outputs	day: 09/15	day: 09/22
total_aircraft_fuel_inside_air_space	44,587.86 kg	49,637.34 kg
total_passenger_CO2_inside_air_space	81,933.04 kg/CO_2	91,211.78 kg/CO_2
total_cost_CO2	R$ 31,430.80	R$ 34,990.27

5. Final considerations

The relevance of this research is proven by the bibliometric occurrence analysis, in which keywords related to severe meteorological events, air transport resilience, and emission of polluting gases appear in more recent publications.

Based on the data presented in Table 4, one can conclude there was an increase in the total flight time within the internal airspace of TMA São Paulo 1 and TMA São Paulo 2, as well as the internal airspace of Campinas traffic control, between 09/15 and 09/22. In addition, the values presented for errors in the different control areas also increased compared to the same period. In particular, the total flight time within TMA São Paulo 1 increased from 06:49:21 on 09/15 to 07:05:35 on 09/22, while the total flight time within TMA São Paulo 2 increased from 00:55:01 to 01:13:34 in the same period. Similarly, the total flight time within Campinas traffic control increased from 00:43:13 to 01:07:01. Based on these results, it is possible to identify areas that require attention to ensure the safety and efficiency of air traffic in the region.

The application of an airspace congestion weather forecasting and analysis system would also contribute to ATFM measures taken with information obtained through the Severe Weather Avoidance Plan (SWAP), whose activation is already aimed at mitigating air traffic disruption from the analysis of weather conditions.

The results show the difference in consumption between the same routes without the flight delay and in a day of operation with some delayed flights. This difference resulted in a consumption of approximately 5 tons more fuel or approximately 11 tons more kg/CO_2 emitted into the atmosphere. This shows the importance of investing in infrastructure, technologies, and pilot training so that aircraft can operate with increasingly restricted visibility and without causing damage to flight operational safety.

The impact of aircraft dwell time for each bedside was not considered in this model; this analysis would be interesting for future research on this topic. Another method would be the use of the Corsia methodology, which uses the power of the engines during the landing and takeoff cycles, in which the aircraft power regime is different.

References

[1] SCARPE, R. A..; L. C. Pelecioni. A data analytics approach for anticipating congested days at the São Paulo International Airport. Journal of Air Transport Management, v. 72, 2018, p. 1-10.

[2] MARQUES, F. B.; Y.; MACULAN, C. M. S. Co-ocorrência de palavras-chave em dados abertos da Capes: teses e dissertações em Ciência da Informação. Múltiplos Olhares em Ciência da Informação, [S. l.], n. Especial, 2021. @the

[3] SANTA, S. L. B.; RIBEIRO, J. M. P.; MAZON, G.; SCHNEIDER, J.; BARCECELOS, R. L.; GUERRA, J. B. S. O. A. A Green Airport model: Proposition based on social and environmental management systems, Sustainable Cities and Society, v. 59, 2020.

[4] POSTORINO, M. N.; MABTECCHINI, L.; MALANDRI, C.; PAGANELLI, F. A methodological framework to evaluate the impact of disruptions on airport turnaround operations: A case study, Case Studies on Transport Policy, v. 8, Issue 2, 2020.
[5] OUM, T. H.; ZHANG, A.; ZHANG, Y. A note on optimal airport pricing in a hub- and-spoke system, Transportation Research Part B: Methodological, v. 30, Issue 1, 1996.
[6] SIVAKUMAR, S. A novel Integrated Risk Management Method for Airport operations, Journal of Air Transport Management, v. 105, 2022.
[7] LARRAONDO, P. R.; INZA, I.; LOZANO J. A. A system for airport weather forecasting based on circular regression trees, Environmental Modelling & Software, v. 100, 2018.
[8] CHEN, Z.; LI, H.; REN, H.; XU, Q.; HONG, J. A total environmental risk assessment model for international hub airports, International Journal of Project Management, v. 29, Issue 7, 2011.
[9] LIN, M. H. Airport pricing and capacity: Schedule versus congestion delays, Research in Transportation Economics, v. 90, 2021.
[10] PEJOVIC, T.; NOLAND, R. B.; WILLIAMS, V.; TOUMI, R. A tentative analysis of the impacts of an airport closure, Journal of Air Transport Management, v. 15, Issue 5, 2009.
[11] OLIVEIRA, M.; EUFRÁSIO, A. B. R.; GUTERRES, M. X.; MURÇA, M. C. R.; GOMES, R. A. Analysis of airport weather impact on on-time performance of arrival flights for the Brazilian domestic air transportation system, Journal of Air Transport Management, v. 91, 2021.
[12] TOKUSLU, A. Estimation of aircraft emissions at Georgian international airport, Energy, v. 206, 2020.
[13] LIN, M. H.; ZANG, A. Hub congestion pricing: Discriminatory passenger charges, Economics of Transportation, v. 5, 2016.
[14] ZHOU, L.; CHEN, Z. Measuring the performance of airport resilience to severe weather events, Transportation Research Part D: Transport and Environment, v. 83, 2020.
[15] PLANDA, B.; SKORUPSKI, J. Methods of air traffic management in the airport area including the environmental factor, International Journal of Sustainable Transportation, v. 11, Issue 4, 2017.
[16] CARVALHO, L.; STERNBERG, A.; GONÇALVES, L. M.; CRUZ, A. B.; SOARES, J. A.; BRANDÃO, D.; CARVALHO, D.; OGASAWARA, E. On the relevance of data science for flight delay research: a systematic review, Transport Reviews, v. 41, Issue 4, 2021.
[17] WANG, Y.; ZHANG, Y. Prediction of runway configurations and airport acceptance rates for multi-airport system using gridded weather forecast, Transportation Research Part C: Emerging Technologies, v. 125, 2021.
[18] SCHULTZ, M.; REITMANN, S.; ALAM, S. Predictive classification and understanding of weather impact on airport performance through machine learning, Transportation Research Part C: Emerging Technologies, v. 131, 2021.
[19] ASHLEY, K.; SAVAGE, I. Pricing congestion for arriving flights at Chicago O'Hare Airport, Journal of Air Transport Management, v. 16, Issue 1, 2010.
[20] RHODES, S. L. The effect of the environment on aviation weather safety: Meteorological assessment for the new Denver airport,
[21] Environmental Impact Assessment Review, v. 13, Issue 1, 1993.
[22] GONG, S. X. H.; CULLINANE, K.; FIRTH, M. The impact of airport and seaport privatization on efficiency and performance: A review of the international evidence and implications for developing countries, Transport Policy, v. 24, 2012.
[23] LUI, G. N.; HON, K. K.; LIEM, R. P. Weather impact quantification on airport arrival on-time performance through a Bayesian statistics modeling approach, Transportation Research Part C: Emerging Technologies, v. 143, 2022.
[24] JOHNSON, T.; SAVAGE, I.; Departure delays, the pricing of congestion, and expansion proposals at Chicago O'Hare Airport, Journal of Air Transport Management, v. 12, Issue 4, 2006.
[25] BURBIDGE, R. Adapting aviation to a changing climate: Key priorities for action, Journal of Air Transport Management, v. 71, 2018.
[26] WANG, S.; CHU, J.; LI, J.; DUAN, R. Prediction of Arrival Flight Operation Strategies under Convective Weather Based on Trajectory Clustering, Aerospace, v. 9, Issue 4, 2022.
[27] KETABDARI, M.; TORALDO, E.; CRISPINO, M. Numerical Risk Analyses of the Impact of Meteorological Conditions on Probability of Airport Runway Excursion Accidents. Computational Science and Its Applications – ICCSA 2020. ICCSA 2020. Lecture Notes in Computer Science, v. 12249. Springer, Cham, 2020.

[28] TASZAREK, M.; KENDZIERSKI, S.; PILGUJ, N. Hazardous weather affecting European airports: Climatological estimates of situations with limited visibility, thunderstorm, low-level wind shear and snowfall from ERA5. Weather and Climate Extremes, v. 28, 2020.
[29] KAEWUNRUEN, S.; SRESAKOOLCHAI, J.; XIANG, Y. Identification of Weather Influences on Flight Punctuality Using Machine Learning Approach. Climate, v. 9, Issue 127, 2021.
[30] ADLER, N.; YAZHEMSKY, E. The value of a marginal change in capacity at congested airports, Transportation Research Part A: Policy and Practice, v. 114, Part A, 2018.
[31] DECEA – Departamento de Controle do Espaço Aéreo. ICA 100-12 – Regras do Ar. Ministério da Defesa, Brasília, 2016.
[32] DECEA – Departamento de Controle do Espaço Aéreo. ROCA 21-74 – Regulamento do Centro de Gerenciamento da Navegação Aérea. Ministério da Defesa, Brasília, 2018.
[33] DECEA – Departamento de Controle do Espaço Aéreo. API-REDEMET: O que é? online, s.d. Disponível em: <https://ajuda.decea.mil.br/base-de-conhecimento/api-redemet-o-que-e/>.
[34] DECEA – Departamento de Controle do Espaço Aéreo. ICA 105-16 – Códigos Meteorológicos. Ministério da Defesa, Brasília, 2017.
[35] IATA – International Air Transport Association (IATA). Air Passenger Numbers to Recover in 2024. ONLINE, 2022. Available at: <https://www.iata.org/en/pressroom/2022-releases/2022-03-01-01/>.
[36] ANAC – Agência Nacional de Aviação Civil. Percentuais de atrasos e cancelamentos. online, s.d. Disponível em: < https://www.anac.gov.br/acesso-a-informacao/dados-abertos/areas-de-atuacao/voos-e-operacoes-aereas/percentuais-de-atrasos-e-cancelamentos>.
[37] DECEA – Departamento de Controle do Espaço Aéreo. Anuário Estatístico de Tráfego Aéreo 2021. ONLINE, 2022. Disponível em: < http://portal.cgna.decea.mil.br/files/uploads/anuario_estatistico/anuario_estatistico_2021.pdf>.
[38] CAMPOS, V. B. G. Planejamento de Transportes: Conceitos e Modelos, Ed. Interciência, 2013.
[39] INVESTING.com. Crédito Carbono Futuros – Dez 22 (CFI2Z2). ONLINE. Disponível em: <https://br.investing.com/commodities/carbon-emissions>.
[40] PRAZERES, D. L.; GUEDES, E. P. A Participação da Administração Privada na Exploração da Infraestrutura Aeroportuária Brasileira. Caderno do IX Simpósio de Transporte Aéreo – SITRAER. Manuais, 2010 p. 386-397, Tr. 41.
[41] CORRADO, S. J.; PURANIK, T. G.; FISCHER, O. P.; MAVRIS, D. N. A clustering-based quantitative analysis of the interdependent relationship between spatial and energy anomalies in ADS-B trajectory data,
[42] Transportation Research Part C: Emerging Technologies, v. 131, 2021.
[43] SILVA, L. C.; MURÇA, M. C. R. A data analytics framework for anomaly detection in flight operations, Journal of Air Transport Management, v. 110, 2023.
[44] DECEA – Departamento de Controle do Espaço Aéreo. CIRCEA 100-77 – Padronização na Utilização do TATIC e SAGIATIO Integrados no Âmbito do SISCEAB. Ministério da Defesa, Brasília, 2017.
[45] DECEA – Departamento de Controle do Espaço Aéreo. AIC A 20/19 - Severe Weather Avoidance Plan (SWAP). Ministério da Defesa, Brasília, 2019.

VOL.40 Nº3 2023
https://doi.org/10.22491/rmct.v40i3.11859.en

Synthesis and characterization of nanoparticles of $CsFeO_2$ using the sol-gel/combustion method

Camila Oliveira Baptista[1]*, Bruno Cardoso[1], Danúbia de Carvalho[1], Claudio de Oliveira[1], Ronaldo de Biasi[1], André Ben-Hur Figueiredo[1]
[1]Instituto Militar de Engenharia, Seção de Engenharia de Materiais
Praça General Tibúrcio, 80, 22290-270
Praia Vermelha, Rio de Janeiro, RJ, Brasil
***camilabaptista@ime.eb.br**

ABSTRACT: Magnetic nanoparticles have many important applications in the technological, environmental, and medical fields due to their special properties (such as superparamagnetism). The main objective of this research is to obtain a magnetic ferrite. The solgel/combustion method was used to produce nanoparticles of cesium ferrite ($CsFeO_2$). Fourier transform infrared spectroscopy characterized the samples, indicating a ferrite phase at the peaks at 343 and 318 cm^{-1} and the metal-oxygen bond vibrations of the atoms in tetrahedral and octahedral sites.

KEYWORDS: Nanoparticles. Superparamagnetism. Cesium ferrite. Sol-gel/combustion. Fourier transform infrared spectroscopy.

RESUMO: As nanopartículas magnéticas possuem diversas aplicações de grande importância nas áreas tecnológica, ambiental e médica devido a propriedades especiais como o superparamagnetismo. O principal objetivo desta pesquisa consiste na obtenção de uma ferrita magnética. Foi utilizado o método de sol-gel/combustão para produzir nanopartículas de ferrita de césio ($CsFeO_2$). A espectroscopia no infravermelho por transformada de Fourier (FTIR) caracterizou as amostras, permitindo a observação da indicação da fase ferrita nos picos de 343 e 318 cm-1, bem como das vibrações da ligação Metal-O dos átomos em sítios tetraédricos e octaédricos.

PALAVRAS-CHAVE: Nanopartículas. Superparamagnetismo. Ferrita de césio. Sol-gel/combustão. Espectroscopia infravermelha por transformada de Fourier.

1. Introduction

Current developments in nanoscience and nanotechnology have led to the discovery of numerous applications of magnetic nanoparticles in fields such as biomedicine, diagnostics, molecular biology, biochemistry, catalysis etc. Nanoparticles of magnetic oxides are mainly composed of Fe_2O_3 (hematite) [1].

Nanomaterials are a relevant topic of research due to their unique properties resulting from their small size. Ferrite nanoparticles notably stand out due to significant changes in their magnetic behavior as particle size decreases.

Nanometer-scale magnetic ceramic particles exhibit behaviors distinct from those of larger particles of the same material. By enhancing their properties, these particles can improve existing materials or even enable the development of entirely new materials. This has spurred extensive research focused on understanding the properties of magnetic nanoparticles, especially those in the ferrite family, a group of metal oxides.

The first commercial ferrite products were developed in 1945 by Kato and Takesi [2]. Since then, efforts have focused on manufacturing increasingly smaller and highly reliable components [3].

Cesium, the least electronegative element, has only one stable isotope, which was used in the synthesis of cesium ferrite ($CsFeO_2$).

Several techniques, including combustion, sol-gel/combustion, and coprecipitation, can be used to prepare ferrite nanoparticles [4,5,6]. As such, the primary objective of this work is to obtain a magnetic ferrite. $CsFeO_2$ nanoparticles were synthesized using the sol-gel/combustion method and characterized via Fourier-transform infrared spectroscopy (FTIR), a fast instrumental technique that detects several functional groups in compounds.

1.1 Theoretical Basis

In order to understand the properties of ferrite, it is necessary to analyze the crystal structure of these materials. Metal oxides have the structure of the mineral spinel ($MgAl_2O_4$), in which the ions O^{2-} with atomic radius of 0.13 nm form a facecentered cubic lattice. Ions of smaller atomic radius occupy tetrahedral sites (Mg^{2+}) called sites [A] and octahedral sites [Al^{3+}], called sites [B] [7].

Ferrite has a spinel-like crystal structure, as shown in Figure 1, represented by the chemical formula $M^{2+}Fe_2^{3+}O_4^{2-}$, where M are divalent metals such as Mn^{2+}, Co^{2+}, Ni^{2+}, Cu^{2+}, Fe^{2+}, Zn^{2+}, and the occupation of tetrahedral and octahedral sites by divalent ions influences the magnetic properties of these materials [8].

Figure 1 - structure of the spinel.

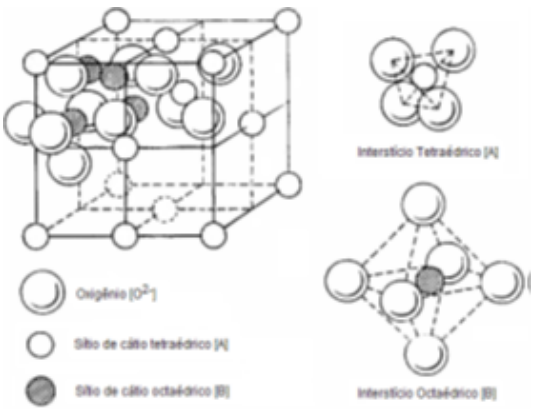

Source: [6]

Since not all available sites are occupied, there are three different configurations that the structure can take: normal spinel, partially inverted spinel and inverted spinel. The normal spinel is defined as the configuration in which only the divalent metal ions (M^{2+}) occupy the sites [A] while Fe ions^{3+} occupy the sites [B]. In the configuration with M^{2+} and Fe^{3+} at sites [A] and [B], with the ratio ranging from 0 to 1, the spinel is classified as partially inverted. In the configuration in which the Fe ions^{3+} occupy the site [A] and half of the site [B], while the M ions^{2+} occupy the other half of the site [B], the spinel is called inverted [7]. The occupation of the sites affects the magnetic behavior of the material.

This behavior is influenced not only by the crystalline structure but also by the macroscopic structure. One notable phenomenon observed in nanoparticles is superparamagnetism. Materials exhibiting this property do not retain magnetic memory, meaning that once they are removed from a magnetic field, no residual magnetization remains, provided the temperature is above the blocking temperature.

2. Development

The synthesis of $CsFeO_2$ powder using the sol-gel/combustion method [8] involved the following steps:

1. Preparing solutions of the chemical precursors $Cs(NO_3)_2.6H_2O$ and $Fe(NO_3)_3.9H_2O$ in distilled water at appropriate concentrations;
2. Preparing a solution of citric acid ($C_6H_8O_7.H_2O$)in distilled water at a molar concentration of 0.75 M;
3. Combining solutions 1 and 2 to obtain a homogeneous mixture;
4. Placing the solution obtained in step 3 on a hot plate at 60 ºC and subjecting it to continuous stirring for approximately 4 hours to form a gel;
5. Heating the gel to 80 ºC while maintaining stirring until it becomes transparent;
6. Increasing the temperature of the transparent gel to 200 ºC to induce a self-combustion process, which occurs for about 20 minutes;
7. Dividing the material obtained in step 6 into several batches and subjecting them to heat treatments at 700 ºC for 30 minutes, 1 hour, and 2 hours.

The infrared vibrational spectra were obtained using a Nicolet iS10 spectrophotometer via attenuated total reflectance (ATR-FTIR), with KBr as a dispersing agent, in the range of 400 to 300 cm^{-1}, at a resolution of 4 cm^{-1}, 32 scans, available at IPqM.

3. Results

In the infrared vibrational spectrum of the $CsFeO_2$ sample, as shown in Figure 2, ferrite phase indication is observed at peaks of 343 and 318 cm^1, as well as the vibrations of the metal-oxygen bond, of atoms in the tetrahedral and octahedral sites [9,10].

Figure 2 - FTIR spectrum of cesium ferrite after a 1-hour heat treatment.

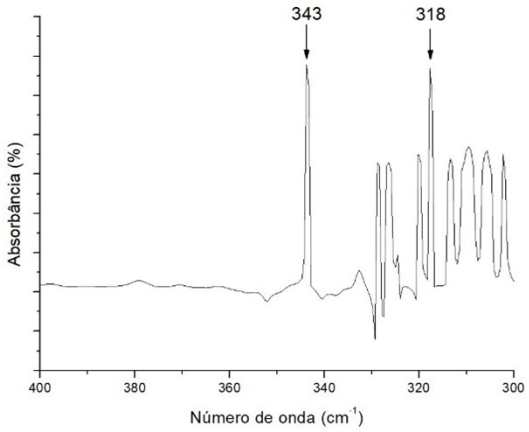

Source: [own elaboration].

4. Conclusion

This work shows that the sol-gel/combustion method is promising for obtaining cesium ferrite in the form of nanometric powder. The spectrum obtained by FTIR characterization demonstrates the success in synthesis with the observation of characteristic ferrite phase peaks and spinel-like structures.

Given the above result, the goal of this work was achieved, which was to obtain a magnetic ferrite.

Acknowledgements

The authors thank FAPERJ, CAPES and CNPQ for their financial support.

References

[1] MATERÓN, E. M.; MIYAZAKI, C. M.; CARR, O.; JOSHI, N.; PICCIANI, P. H. S.; DALMASCHIO, C. J.; DAVIS, F.; SHIMIZU, F. M. Magnetic nanoparticles in biomedical applications: A review. *Applied Surface Science Advances*, [*s. l.*], v. 6, p. 100-163, 2021. DOI: 10.1016/j.apsadv.2021.100163.

[2] KATO, Y.; TAKESI, T. Japan Patent, 98844, 1932. *In*: OHIAI, T. Current Status os Soft Ferrite in Japan. *Journal Physical IV*, France, v. 7, n. C1, p. C1-27-C1-30, 1997.

[3] GAMA, A. M.; LANGDRAF, F. J. G.; GOUVÊA, D.; RODRIGUES, D.; JANASI, S. R. Efeito das condições de sinterização na microestrutura e nas propriedades magnéticas das ferritas Mn-Zn. *In*: CONGRESSO ANUAL DA ABM- INTERNACIONAL, 57, 2002, São Paulo. *Anais*. São Paulo: ABM, 2002. p. 832-841.

[4] MONTEIRO, E. S. *Nanopartículas de ni-zn utilizadas como absorvedoras de micro-ondas*. 2016. Dissertação (Mestrado em Ciência dos Materiais) – Programa de Pós-Graduação em Ciência dos Materiais, Instituto Militar de Engenharia, Rio de Janeiro, 2016.

[5] CARP, O.; PATRON, L.; RELLER, A. Coordination compounds containing urea as precursors for oxides – a new route of obtaining nanosized $CoFe_2O_4$. *Materials Chemistry and Physics*, [*s. l.*], v. 101, n. 1, p. 142-147, 2007.

[6] ZHANG, S.; DONG, D.; SUI, Y.; LIU, Z.; WANG, H.; QIAN, Z.; SU, W. Preparation of core shell particles consisting of cobalt ferrite and silica by sol-gel process. *Journal of Alloys and Compounds*, [*s. l.*], v. 415, n. 1-2, p. 257-260, 2006.

[7] CULLITY, B. D.; GRAHAM, C. D. *Introduction to Magnetic Materials*. 2. ed. New Jersey: Wiley, 2009.

[8] HUANG, Y.; TANG, Y.; WANG, J.; CHEN, Q. Synthesis of MgFe2O4 nanocrystallites under mild conditions. *Materials Chemistry and Physics*, [*s. l.*], v. 97, n. 2-3, p. 394-397, 2006. DOI: 10.1016/j.matchemphys.2005.08.035.

[9] RAJASHEKHAR, K.; VINOD, G.; KUMAR, K. M.; NAIK, J. L. Impact of erbium (Er) doping on the structural and magnetic properties of Ni-Cu ($Ni_{0.1}Cu_{0.9}Fe_2O_4$) nanoferrites. *Journal of Magnetism and Magnetic Materials*, [*s. l.*], v. 555, p. 169-323, 2022. DOI: 10.1016/j.jmmm.2022.169323.

[10] MOUHIB, Y.; BELAICHE, M.; ELANSARY, M.; FERDI, C. A. Effect of heating temperature on structural and magnetic properties of zinc ferrite nanoparticles synthesized for the first time in presence of Moroccan reagentes. *Journal of Alloys and Compounds*, [*s. l.*], v. 895, p. 162-634, 2022.

VOL.40 Nº3 2023
https://doi.org/10.22491/rmct.v40i3.12299.en

Advancements in gunshot signal detection using acoustic sensors

José Antonio Apolinário Junior[1], apolin@ime.eb.br, Orcid 0000-0003-1426-9636
Lucas Rafael de Aguiar Silva[1], lucas.silva@ime.eb.br, Orcid 0009-0007-8139-4644
[1] Instituto Militar de Engenharia (IME) – SE/3

ABSTRACT: The detection of impulsive acoustic signals and their classification as gunshots plays a crucial role in systems designed to pinpoint the origin of gunshots fired by snipers or regular shooters. With significant applications in the military context, gunshot detection systems face substantial challenges related to their use in operational environments, which often involve multipath propagation and environmental noise. Moreover, these systems need to be capable of real-time operation. This article addresses modern methods for detecting and classifying the acoustic components of gunshot signals, proposing modifications to enhance their performance and evaluating them using a diverse dataset of real-life gunshot signals. The results are compared to determine the most suitable method for hardware implementation. The text provides valuable insights for developing gunshot detection systems in challenging environments.

KEYWORDS: Gunshot Signals. Sniper. Detection. Classification. Direction of Arrival.

RESUMO: A detecção de sinais acústicos impulsivos e sua classificação como disparos de arma de fogo desempenham um papel crucial em sistemas destinados a localizar a origem de tiros por caçadores ou atiradores em geral. Com aplicações de relevância no contexto militar, os sistemas de detecção de tiros enfrentam desafios substanciais relacionados ao seu uso em ambientes operacionais, que frequentemente envolvem propagação multipercurso e ruído ambiental. Além disso, esses sistemas precisam ser capazes de operar em tempo real. Este artigo aborda métodos modernos para a detecção e classificação das componentes acústicas dos sinais de tiro, propondo modificações visando aprimorar seus desempenhos e avaliando-os com uma diversificada base de sinais de tiros reais. Os resultados obtidos são comparados para determinar o método que se mostra mais adequado para uma implementação em hardware. O texto fornece insights valiosos para o desenvolvimento de sistemas de detecção de tiros em ambientes desafiadores.

PALAVRAS-CHAVE: Sinais de Tiro. Caçador. Detecção. Classificação. Direção de Chegada.

1. INTRODUCTION

Contemporary conflicts are intrinsically related to the application of technology on the battlefield. The Ukraine War exemplifies military applications that encompass missiles, drones, radars, and cyberwarfare [1]. Still, conventional military assets ubiquitously and lethally persist in security force ranks. This study highlights a notoriously silent threat: snipers [2].

Snipers have the mission of penetrating enemy defenses by refined camouflage techniques, eliminating strategic targets, and causing confusion in enemy troops [2]. Snipers carry a mystical aura the media has highlighted, including as in movies such as *Pacific Rim* (2001, which tells the story of a Soviet soldier named Vasily Zaitsev at the Battle of Stalingrad) [3] and *American sniper* (2014, based on the autobiography of Chris Kyle, an American sniper who achieved notorious feats in the Iraq War) [4]. Other notable examples include Finnish Simon Häyhä (known as "White Death") and Lyudmila Pavlichenko (known as "Lady Death"), born in the Kiev Province (then Russian Empire) [5].

The main tactics against sniper action consist of moving the troops out of the enemy's angle of sight and shooting at them in to force them to change positions [2]. However, these actions require knowledge of the original direction of the shot [6]. Thus, research carried out more than a decade ago at the Military Institute of Engineering Digital Signal Processing Laboratory [7-13] stands out as it aimed to improve the algorithms to estimate enemy snipers' direction of arrival. This takes place by processing the acoustic components of a firing signal: the shock wave (SW) in the case of a supersonic projectile and the explosion of the propellant charge muzzle blast (MB).

Armies around the world apply the available commercial solutions to obtain this direction. Examples

include the American Boomerang III (Raytheon), the Turkish TRV-SD 500 (Transvaro), and the French Pillar V (Metravib Defence) systems [14-16].

The estimation of the direction in which snipers fired their shots requires the previous detection of their shots, which comprises two steps: detecting impulsive signals and classifying them into SW or MB, when applicable [6]. This study aims to evaluate the performance of gunshot signal detection algorithms, propose adaptations to improve their results, and indicate the best option for practical applications. It analyzed four methods: cross-correlation [7], energy spectral analysis [17], signal-to-noise ratio (SNR) [18], and neural networks [19].

Once an impulsive signal is detected, it is necessary to determine whether it comes from a firing signal (classify it as SW or MB) or not. SW constitute acoustic waves generated by the Mach effect in the trajectory of the supersonic projectiles from a rifle, for example [20]. On the other hand, MB corresponds to the acoustic wave formed by the difference in pressure between the external environment of the weapon and the gas within the weapon that undergoes heating by projectile charge activation [20]. A relevant piece of information about SW is that it has an "N" shape and a duration from 0.3 to 0.5 ms, whereas MB lasts from 3 to 5 ms [20].

2. FUNDAMENTAL CONCEPTS

2.1 Geometry of the problem

The typical geometry of detecting sniper shots consists of three elements: shooter, target, and microphone array. An array of microphones is used to estimate the direction of arrival. Figure 1 shows the arrangement of these elements and indicates the SW and MB wavefronts generated by the trigger.

The typical configuration of a shot may differ from Figure 1 due to the absence of either SW or MB, which occur when objects or barriers prevent acoustic waves from reaching the microphone array [6]. The SW component may also be absent if the microphones are positioned behind the shooter and thus out of the shockwave field of view.

Figure 1 - Typical geometry of the detection problem of a supersonic projectile.

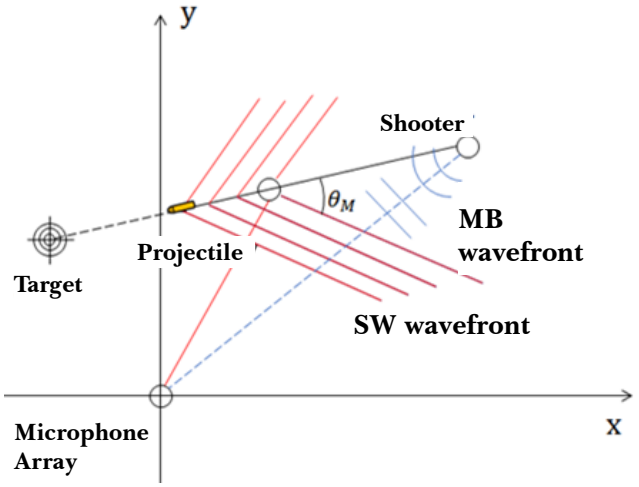

2.2 Impulsive Signal Detection

The first stage of the processing addressed in this study consists of verifying whether the time window of the analyzed acoustic signal corresponds to an impulsive signal. Detection involves ascertaining whether a specific parameter obtained by applying an algorithm (e.g., the peak cross-correlation of the acquired signal window with a known SW model) exceeds a certain threshold. Training occurs by varying the threshold in a range of values, forming a receiver operating characteristic (ROC) [21].

This curve is constructed from the following performance measures: true (TPR) and false positive rates (FPR). TPR and FPR, expressed by Equations (1) and (2) [21], respectively, are best understood by a confusion matrix, as in Table 1.

$$TPR = \frac{TP}{TP + FN} \quad (1)$$

$$FPR = \frac{FP}{FP + TN} \quad (2)$$

In the ROC curve for the FPR × TPR axis system, the closer the curve gets to the point (FPR, TPR) = (0.1), the better the detector performance. Since in practice this point is usually unable to be obtained,

the point of operation is chosen based on operational criteria.

Table 1 - Confusion matrix

		Truth Condition	
		Present	**Absent**
Test Result	Positive	TP	FP
	Negative	FN	TN

2.3 Classification of Shooting Signals

The classification of an impulsive signal involves deciding which components emerge in an audio window, whether they are SW, MB, or NS (non-shooting window, i.e., the impulsive signal fails to characterize a shot). This typification requires extracting parameters from the signal and applying a classification criterion to these parameters. This study used the following four features: the peak of cross-correlation with a model, the linear predictive coding (LPC) and Mel-frequency cepstral coefficients (MFCC), and the normalized signal energy [7] [17] [18] [19].

Table 2 - Feature vector

Features	Indices
Cross-correlation with the SW/MB AGLC Model	1 and 2
Cross- correlation with the SW/MB FAL Model	3 and 4
Cross- correlation with the SW/MB M2 Browning Model	5 and 6
Cross-Correlation with IA2 SW/MB Model	7 and 8
LPC coefficients (20)	9 to 28
MFCC coefficients (26)	29 to 54
Normalized signal power (Z)	55

Table 2 shows the distribution of the classification features. The weapons are detailed in Section 3.1. Each method extracts a number of parameters. Processing (detection and classification) was performed on Matlab® Classification Learner or Neural Pattern Recognition, in which the input of both consists of an array with the features of a set of windows and the output is a function that performs the sorting.

3. METHODOLOGY

The detection and classification of impulsive signals, such as SW or MB, involve several initial steps, from acquiring audio signals to training algorithms to automatically achieve the goals of this study. Next, we describe the used weapons, the composition of the signal dataset for training and testing, its preparation before the application of the algorithms, and the analyzed methods, highlighting details of the original algorithms and the implemented adaptations.

3.1 Signal dataset and weapons

The AGLC, the FAL, the IA2, and the M2 Browning [22–25] are weapons used by Brazilian Army snipers (which constituted the signal dataset), all of which can perform supersonic firing. Some technical characteristics of each of these weapons are shown in Table 3.

Signals were sampled by a ECM8000 Behringer [26], used in previous arrangements to acquire audio from the main dataset in this study.

A 96-kHz sampling frequency was used to process the audio signals. Signals that had initially been acquired at 44.1 kHz were resampled on Matlab®.

The signals were collected from four shooting ranges: Centro de Avaliação do Exército (CAEx) 2011, Centro de Instrução de Operações Especiais (CIOpEsp) 2010, CAEx 2014, and Centro de Instrução Almirante Milcíades Portela Alves (CIAMPA) 2010. Table 4 shows the distribution of shooting signals for training.

Table 3 - Characteristics of some weapons used by Brazilian snipers

Weapon	AGLC	IA2	FAL	M2 Browning
Caliber	.308" or 7.62 mm	7.62 mm	5.56 mm	.50" or 12.7mm
Initial velocity (m/s)	820	840	780	930
Range (m)	800	1800	300	300
Manufacturer	IMBEL	IMBEL	IMBEL	General Dynamics

Table 4 - Distribution of SW and MB during training for each base

Dataset	Weapon (distances)	Number of Signals
CAEx 2011	AGLC (300 to 700 m)	28 SW and 28 MB
	FAL (300 to 500 m)	20 SW and 20 MB
	IA2 (300 to 500 m)	21 SW and 21 MB
	.50 BMG (300 to 500 m)	16 SW and 15 MB
CIOpEsp	AGLC (200 m)	5 SW and 5 MB
	PSG1 (200 m)	3 SW and 3 MB
CAEx 2014	AGLC (540 to 1062 m)	43 SW and 43 MB
CIAMPA 2010	FAL (31 to 74 m)	23 SW and 10 MB

All signals were divided into 20-ms windows and a 50% superposition to obtain windows containing SW, MB, or NS. The distribution of these windows for training and testing is shown in Table 5. In training, a number of SW, MB, and NS windows were separated to avoid classification bias and maintain balanced quantities. In testing, 60 complete audios of the shooting dataset were used (12 from CAEx 2014, 40 from CAEx 2011, five from CIOpEsp 2010, and nine from CIAMPA 2010), simulating the large intervals of time in which snipers will fire no shots in the battlefield. This resulted in a discrepant number of NS windows relative to the other classes.

Table 5 - Window Distribution

Window Type	Training	Test
SW	159	60
MB	144	60
NS	313	36476

Previously described shot signals [27] available for download on the internet were used to evaluate the performance of the most efficient method to process the signals available at the Military Institute of Engineering Digital Signal Processing Laboratory

in comparison to another dataset. At this second base, three different weapons were used: .45-," .40-," and 9-mm automatic pistols with 12 shots in nine positions, totaling 324 shots [27]. The projectiles of these pistols are not supersonic, so the recorded audio only features MB.

3.2 Preparation of the dataset

As the acquisition of the firing signals occurred under several environments and microphone gain values, the energy of each signal was normalized after the DC level was removed (if present). To reduce the influence of noise (especially on the MB components of the signals, which, have the lowest SNRs due to shooters' further distances), a median filter [9] was applied to enhance the impulsive portions of the audio signals.

3.2 Methods

The four methods in this study will be detailed below. Training for each method involves two steps: a detection threshold (e.g., obtained by constructing a ROC curve and choosing an operating point) and generating a criterion or function (e.g., by a machine learning algorithm) that classifies windows into SW, MB, or NS. Both steps are shown in Figure 2. The testing of each method involves a detection threshold and a classification criterion obtained in training with audio signals divided into windows containing shots (SW, MB, or both) or no shots (only ambient noise).

Figure 2 - General flowchart of detection and classification.

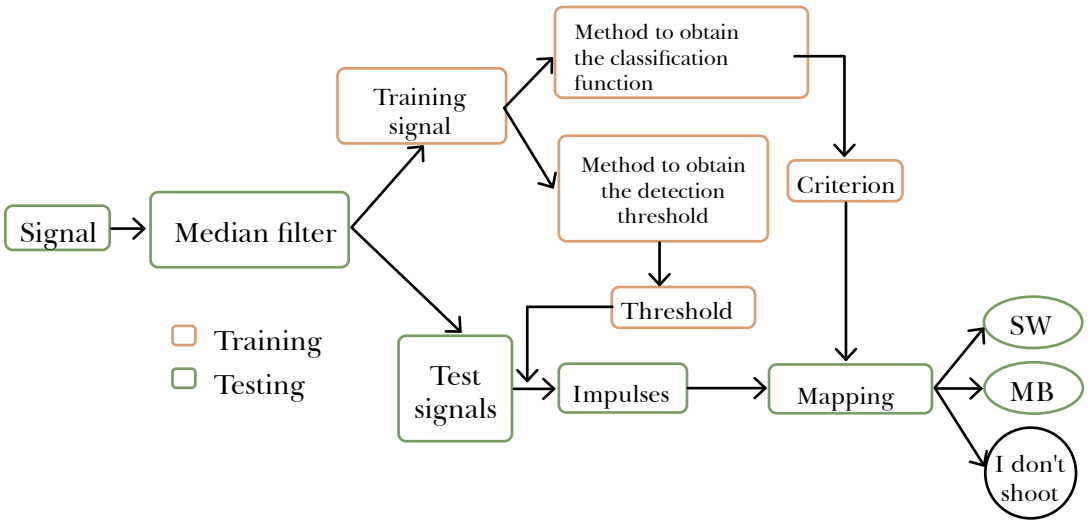

3.2.1 Cross-Correlation Method

In the original version of this method, detection is performed by applying the generalized cross-correlation algorithm to each window, indicating an impulsive signal if the value from the cross-correlation peak exceeds a threshold. In detection training, as in Figure 3, the cross-correlation of each training signal window with an AGLC SW model (reference signal) is computed. The cross-correlation peaks are separated and converted into a confusion matrix. Obtaining several confusion matrices by varying the threshold generates an ROC curve that enables the choice of the operating point. In our experiments, the operating point chosen was TPR > 90%.

Figure 3 - Delimitation of the detection threshold in the Cross-Correlation Method.

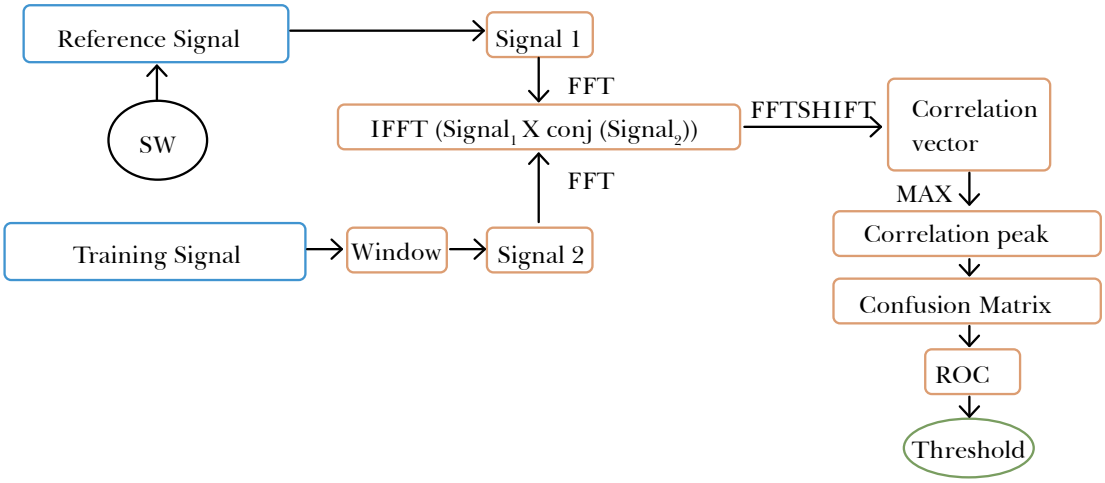

Source: [7]

The method in [7] exclusively uses the SW of the AGLC rifle as a reference signal and includes no algorithm to distinguish SW, MB, and NS. The SW and MB components of the four weapons in Table 3 were used in this study, i.e., the first eight parameters (cross-correlation peaks) of the trait vector in Table 2. The modified version of this method uses the nonlinear function on Matlab® Classification Learner as a classification algorithm according to support vector machine kernel (SVM Kernel).

3.2.2 Energy spectral analysis

Obtaining the detection threshold of this method involves computing the energy E_{win} from the short-time Fourier transform of the $x(n)$ windowed signal, i.e., $X(k)$ corresponds to the DFT matrix of the product $x(n)$ by a window $w(n)$, in which "n" is the discreet time and "k" is the index (the *bin* frequency) of the DFT. E_{win} obtains the impulsive signal detection function for each D_{win} window, according to Equations (3) and (4) [17]. If D_{win} exceeds the threshold, it is assumed that the window sign is impulsive [17]. To obtain this threshold, a ROC curve was constructed to enable the choice of the operating point (in our experiments: TPR > 90%).

$$E_{win} = \sum_{k} |X(k)|^2 \qquad (3)$$

$$D_{win} = \frac{E_{(win+1)} - E_{(win-1)}}{3} \qquad (4)$$

This method dispenses with classification training as it is simply based on the two conditions described by Equations (5) and (6) [17].

$$S1: E_{(f>1600Hz)} > 2E_{(f<1600Hz)} \qquad (5)$$

$$S2: Impulse(i) - Impulse\ (i-1) > 0.2 \qquad (6)$$

Table 6 indicates how the classification in this method occurs according to conditions S1 and S2 [17].

Table 6 - Classification by the Energy Spectral Analysis Method

		S1	
		True	False
S2	True	SW	NT
	False	NT	MB

3.2.3 SNR Analysis

In this method, the detection threshold is obtained by the normalized energy of the signal (Z) [18]. If the Z value of a window exceeds the threshold, it contains an impulsive signal. Let $x(n) = hs(n) + r(n)$, in which $r(n)$ is noise (considered Gaussian white), $s(n)$ is the impulsive sign in case of $h = 1$ (the presence of an impulsive signal). If $h = 0$, that window showes

no impulsive signal [17]. Thus, the signal energy of the window normalized by the noise energy in that window (parameter *Z*) is given by Equation (7) [18].

$$Z = \frac{1}{\hat{\sigma}_r^2} \sum_{n \in Window} x^2(n), \qquad (7)$$

in which $\hat{\sigma}_r^2 = \sum_{n \in Window} r^2(n)$ is an estimate of the energy of the noise.

Detection training in this method begins by obtaining the parameter $a = WT$, in which W is the bandwidth of SW or MB signals and T is the sampling period. Next, the lowest SNR value of the SW and MB windows is determined. With a, it is used to compute P_m (probability of missing an impulsive signal) and P_{fa} (probability of indicating that a window without impulse is impulsive), according to Equations (8) and (9), in which Γ is the Gamma function, γ is the lower incomplete Gamma function, Q_a is the Generalized Marcum Q function, and λ it is the decision-maker [18].

$$P_{fa} = FP = 1 - \frac{\gamma(a, \frac{\lambda}{2})}{\Gamma(a)} \qquad (8)$$

$$P_m = FN = 1 - Q_a(\sqrt{2\gamma}, \sqrt{\lambda}) \qquad (9)$$

Next, the odds charts of P_{fa} and P_m due to λ are obtained. The graph of P_m is a growing function with the increase of λ, whereas the graph of P_{fa} is a decreasing function [18]. The operating point chosen for this study was $P_{fa} < 2\%$.

To train the classification, 18 parameters (eight cross-correlation peaks and 10 LPC coefficients) were used as input on Matlab® Classification Learner. The function generated by the SVM Kernel was chosen as a classification criterion due to its better performance for this method.

3.2.4 Classification Using Neural Networks

Originally, this method failed to clearly distinguish detection from classification. To improve it, we chose to incorporate the detection mechanism in the SNR method [18]. Matlab® Neural Pattern Recognition was used to train the classification. Input considered a 55-element vector composed of eight cross-correlation peaks, 20 LPC coefficients, 26 MFCC coefficients, and 1 Z parameter. The output of this application was modeled by a function simulating a two-layer feed-forward neural network: a hidden layer with 10 neurons (sigmoid activation function) and a a three-neuron exit layer (softmax activation function). Scaled conjugate gradient was used as the algorithm for training. The neural network architecture of this method is shown in Figure 4.

Figure 4 - Feed-forward network structure used in by the Neural Network Method.

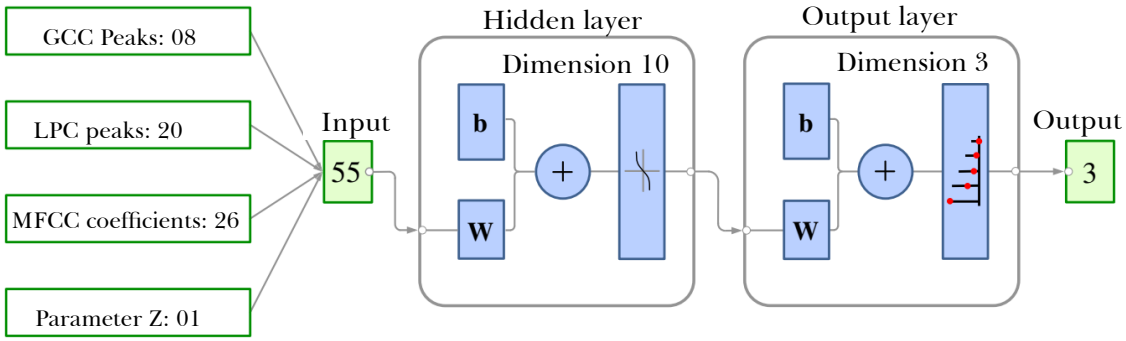

4. EXPERIMENTAL RESULTS

Table 7 shows the analysis of the training results, highlighting the TPR and FPR metrics for each method in the detection and classification stages.

Table 8 shows the runtimes. This research conducted all processing, including training and testing, on Matlab® using a computer equipped with an Intel® Core™ i5-8250U processor with a CPU @1.60GHz 1.80GHz and 8GB RAM with no SSD.

Energy spectral analysis showed the shortest runtime in windows with pulses as its classification algorithm dispenses with obtaining new parameters. Neural networks obtained the second-best runtime

despite its greater number of parameters. This result stems from the robustness of the classification algorithm of this method, which is simpler than the SVM Kernel approach, a nonlinear technique.

Table 7 - Training Result

Method	TPR	FPR
Cross-Correlation	93.79 %	6.21 %
Energy Spectral Analysis	90.03 %	4.70 %
SNR	97.27 %	5.25 %
Neural Networks	95.83 %	2.28 %

Tabela 8 - Runtime

Method	Window without impulse	Window with impulse
Cross-Correlation	2.26 ms	6.49 ms
Energy Spectral Analysis	3.65 ms	3.82 ms
SNR	1.13 ms	11.72 ms
Neural Networks	1.02 ms	4.80 ms

Table 9 shows the test results. Cross-correlation detected all SWs but with a relatively lower detection of MBs than the other methods. The neural network detected and classified the largest number of MBs.

Table 9 - Gross Results (correct windows)

Method	SW (60)	MB (60)	NS (36476)
Cross-Correlation	60	17	36471
Energy Spectral Analysis	56	31	36461
SNR	53	48	36471
Neural Networks	55	54	36457

Table 10 shows the classification errors during the test. It shows that SNR and neural network analysis had fewer total errors than the other methods.

Table 10 - Gross errors (wrong windows)

	Cross--Correlation (48)	Energy Spectral Analysis (67)	SNR (19)	Neural Networks (30)
SW → MB	0	1	7	5
SW → NS	0	2	0	0
MB → SW	0	3	2	1
MB → NS	43	26	10	5
NS → SW	0	1	1	4
NS → MB	5	34	4	15

Table 11 shows the results of a suggested authorial coefficient, as per Equation (10), that prioritizes MB TPR over the SW TPR. This choice is justified by the sniper's direction estimation algorithm using MB information as its input data. In this perspective, neural networks obtained the best result.

$$Coefficient = \frac{3TPR_{SW} + 5TPR_{MB}}{8} \quad (10)$$

Table 11 - Coefficient Equation (10)

Method	TPR_{SW}	TPR_{MB}	Coefficient
Cross-Correlation	1	0.283	0.552
Energy Spectral Analysis	1	0.516	0.697
SNR	0.933	0.8	0.849
Neural Networks	0.916	0.9	0.906

Table 12 shows the results by error rate coefficient, given by Equation (11) [21], in which N = 36596 (the total number of windows), in which SNR performed better in the face of errors.

$$Error\ Rate = \frac{FN + FP}{N} \quad (11)$$

Table 12 - Error rate

Method	FN	FP	Error Rate
Cross-Correlation	43	5	0.13 %
Energy Spectral Analysis	25	35	0.16 %
SNR	17	5	0.06 %
Neural Networks	11	19	0.08 %

Table 13 shows the results of each algorithm in the application of the F1 score coefficient, as per Equation (12). This coefficient is important in analyzing data sets with large discrepancies in the number of samples between classes [21], as in the test signals.

$$F1 = \frac{2TP}{2TP + FP + FN} \quad (12)$$

Table 13 - F1 Score Coefficient

Method	TP	FN	FP	F1 (%)
Cross-Correlation	36818	43	5	99.9348
Energy Spectral Analysis	36806	25	35	99.9185
SNR	36844	17	5	9.9701
Neural Networks	36836	11	19	99.9592

These results suggested neural networks as the most appropriate method to detect and classify firing signals. It classified MB well and showed a low computational complexity as it training took place offline.

Table 14 shows the results from applying neural networks (considered the most appropriate for the application in the dataset in [27]). In this context, the rural situation refers to the shooting signals from the datasets in this study (rural environment), whereas the urban setting refers to the shooting dataset in [27]. Even when used in a set of firearms unlike those in training, highlighting the absence of supersonic characteristics in the projectiles and a high degree of multipath typical of urban environments, the method could separate the MB, achieving a TPR higher than 70% for all weapons in [27].

Table 14 - Test results at the urban dataset [27] with training at the rural dataset

	Caliber.45	Caliber.40	Caliber 9 mm
MB→MB	**80**	**79**	**92**
MB→NS	**28**	**29**	**16**
NS→MB	**4**	**5**	**17**
TPR	**74.07%**	**73.15%**	**85.18%**

Table 15 shows the results of the training and testing under several training/test configurations.

Table 15 - Test results with different types of training and test scenarios

Training	Test	TPR
Rural	Rural	95.83 %
	Urban	77.47 %
Urban	Rural	90.56 %
	Urban	88.88 %
Mixed	Rural	90.56 %
	Urban	85.18 %

5. Conclusion

This research [28] aimed to replicate and compare algorithms to detect and classify impulsive signals into three categories: SW, MB, or NS. For this, it developed routines on Matlab® to train and test each of the four chosen methods. To improve classification results, it suggested modifications to the cross-correlation and neural networks methods.

This study focused on real-time military applications to meet possible needs in the fight against snipers. Automating detection and classification procedures can effectively integrate software and hardware requirements to estimate shooters' direction of arrival. By having information about the direction of fire, soldiers can enjoy greater protection against lethal threats as they can better seek cover or neutralize snipers.

This study sought to compare and optimize algorithms to detect shot signals. As the cross-correlation method based on [7] lacked a clear methodology to distinguish SW from MB, we used more reference signals and a classification scheme based on RBF SVM

Kernel. However, the method still faced difficulties to clearly differentiate the SW components. Spectral energy analysis, as in [17], obtained no good results in classifying shots since its effectiveness depended on the characteristics of the weapon and the geometry of the environment (relative positions of the shooter, target, and microphone). The SNR in [18] robustly detected impulsive signals but lacked improvement in MB component classification, the most relevant information for the considered applications. Finally, the neural networks in [19] failed to clearly distinguish detection from classification. To improve it, this research suggested the detection process in [18], in which the methodology in [17] served to obtain the classification criterion. This study considered this method, with the suggested adaptations, as the most appropriate for the purpose of this study, resulting in a higher MB success rate of the four methods.

This study used two-layer feed-forward neural networks on Matlab® Classification Learner. A possible extension of this study on the state of the art of methods to detect and classify shot signals could investigate deep and convolutional neural networks to process shot signal spectrograms. This approach can open new perspectives to improve these methods and apply them in practical combat situations.

The use of the method we found the most effective for recordings from rural environments, such as shooting ranges and instruction camps, in a second dataset containing shots from an urban environment, brought new perspectives on the applicability of this technique. Despite the good results from training in a rural environment, the use of this method in urban scenarios offers additional challenges and requires specific training with signals in the latter context. Using a hybrid training for rural and urban settings reduced TPR from 3.7 (urban setting) to 5.3% (rural setting) when compared to training and testing in the same setting.

REFERENCES

[1] PALAVENIS, D. The use of emerging disruptive technologies by the Russian Armed Forces in the Ukrainian War. **Air Land Sea Application Center**. Hampton, 1 out. 2022. Disponível em: https://www.alssa.mil/News/Article/3170285/the-use-of-emerging-disruptive-technologies-by-the-russian-armed-forces-in-the/. Acesso em: 7 jun. 2025.

[2] SOUZA, G. L. **História Militar**: o emprego do caçador. Trabalho de Conclusão de Curso (Bacharelado em Aperfeiçoamento Militar) – Escola de Aperfeiçoamento Militar, [*s. l.*], 2020. Disponível em: http://bdex.eb.mil.br/jspui/handle/123456789/6570. Acesso em: 7 jun. 2025.

[3] Círculo de fogo. Direção: Jean-Jacques Annaud. Produção de Mandalay Pictures. Estados Unidos: Paramount Pictures, 2001.

[4] Sniper Americano. Direção: Clint Eastwood. Produção de Village Roadshow Studios e Malpaso Productions. Estados Unidos: Warner Bros, 2014.

[5] SLAWSON, L. The Top Ten Deadliest Snipers in History. **Owlcation**, September 15th, 2023. Disponível em: https://owlcation.com/humanities/Top-Ten-Deadliest-Snipers-in-History. Acesso em 9 jun. 2025.

[6] FREYTAG, J. C.; BRUSTAD, B. M. A survey of audio forensic gunshot investigations. *In*: AES International Conference: Audio Forensics in the Digital Age, 26., 2005, Denver. **Anais** […]. Denver: Audio Engineering Society, p. 131-134, 2005.

[7] FREIRE, I. L.; APOLINÁRIO JR., J. A. Gunshot detection in noisy environments. *In*: International Telecommunication Symposium (ITS), 7., 2010, Manaus. **Anais** […]. Manaus: ITS, p. 1-4, 2010.

[8] SERRENHO, F. G. **Estimação robusta da direção de chegada de sinais de tiros a partir de VANT de asa rotativa**. 2020. Dissertação (Mestrado em Engenharia Elétrica) – Instituto Militar de Engenharia (IME), Rio de Janeiro, Brasil, 2020.

[9] BORZINO, A. M. C. R. *et al*. Signal enhancement for gunshot DOA estimation with median filters. *In*: *IEEE Latin American Symposium on Circuits and Systems (LASCAS)*, 6., 2015, Montevideo. **Anais** […]. Montevideo, 2015.

[10] BORZINO, A. M. C. R.; APOLINÁRIO JR., J. A.; CAMPOS, M. L. R. Robust DOA estimation of heavily noisy gunshot signals. *In*: IEEE International Conference on Acoustics, Speech, and Signal Processing (ICASSP), 2015, Brisbane. **Anais** […]. Brisbane: IEEE, 2015. p. 449-453.

[11] FREIRE, I. L.; APOLINÁRIO Jr., J. A. GCC-based DoA estimation of overlapping muzzleblast and shockwave components of gunshot signals. Latin American Symposium on Circuits and Systems (LASCAS) 2., 2011, Bogota. **Anais** […]. Bogotá: IEEE, 2011. https://doi.org/10.1109/LASCAS.2011.5750273.
[12] BORZINO, A. M. C. R. **Processamento de sinais de áudio proveniente de disparo de arma de fogo e Aplicações**. 2016. Tese (Doutorado em Engenharia de Defesa) – Instituto Militar de Engenharia (IME), Rio de Janeiro, Brasil, 2016.
[13] BORZINO, A. M. C. R.; APOLINÁRIO JR., J. A.; CAMPOS, M. L. R. Consistent DOA estimation of heavily noisy gunshot signals using a microphone array. **IET Radar, Sonar & Navigation**, Stevenage, p. 1517-1728, 2016.
[14] MAGAND, F.; Donzier, A.; Molliex, F. **PILAR Acoustic Gunshot Detection & Localization system**: principles of acoustic localization of small caliber gunshots. Joint Congress CFA–DAGA, Strasbourg, France, 2004.
[15] Raytheon Intelligence & Space, "Boomerang Gunshot Detection: Locate the Enemy - Coordinate the Response". **Raytheon BBN Technologies**, Cambridge, 2020. Disponível em: https://pt.scribd.com/document/532314657/boomerang-data-sheet-soft-copy-final. Acesso em: 9 jun. 2025.
[16] TRANSVARO SAVUNMA SANAYİ A.Ş. **TV-SD 500 Acoustic Sniper Detection System: user manual**. İstanbul; Ankara: Transvaro Savunma Sanayi A.Ş., [s.d.]. Disponível em: https://www.transvaro.com/wp-content/uploads/akustik-eng.pdf. Acesso em: 7 jun. 2025.
[17] MÄKINEN, T.; PERTILÄ, P. Shooter localization and bullet trajectory, caliber, and speed estimation based on detected firing sounds. **Applied Acoustics**, Amsterdam, v. 71, n. 10, p. 902-913, 2010. https://doi.org/10.1016/j.apacoust.2010.05.021
[18] AHMED, T.; UPPAL, M.; MUHAMMAD, A. Improving efficiency and reliability of gunshot detection systems. In: IEEE International Conference on Acoustics, Speech, and Signal Processing (ICASSP), 2013, Vancouver. **Anais** […]. Vancouver: IEEE, 2013. p. 513-517.
[19] HRABINA, M.; SIGMUND, M. Comparison of feature performance in gunshot detection depending on noise degradation. *In*: International Conference Radioelektronika, 27., 2017, Brno. **Anais** […]. Brno: 2017. p. 223-226.
[20] MAHER, R. C. Modeling and signal processing of acoustic gunshot recordings. Signal Processing Education Workshop, Teton National Park, 4., Piscataway, 2006. Anais […[. Piscataway: IEE, 2006. pp. 257-261. https://doi.org/10.1109/DSPWS.2006.265386.
[21] LARNER, A. J. **The 2×2 Matrix Contingency, Confusion, and the Metrics of Binary Classification**. Liverpool: Springer Nature Switzerland AG, 2021. https://doi.org/10.1007/978-3-030-74920-0
[22] INDÚSTRIA DE MATERIAL BÉLICO DO BRASIL (IMBEL). **Manual do Fuzil .308 – IMBEL AGLC**: instruções de operação, manutenção e características técnicas. Brasília: IMBEL, 2018. Disponível em: https://www.imbel.gov.br/phocadownload/produtos/manuais/fz-ca/manual-fzaglc308.pdf. Acesso em: 7 jun. 2025.
[23] BRASIL. Ministério do Exército. **Manual de Campanha C-23-65**: Metralhadora .50 M2. 3. ed. Rio de Janeiro: Ministério do Exército, 1963. Disponível em: https://bdex.eb.mil.br/jspui/bitstream/123456789/425/5/C-23-65-final.pdf. Acesso em: 7 jun. 2025.
[24] INDÚSTRIA DE MATERIAL BÉLICO DO BRASIL (IMBEL). **Manual do Fuzil 7,62 M964–FAL / M964A1–PARAFAL**: operação, manutenção e características técnicas. Brasília, DF: IMBEL, 2014. Disponível em: https://www.imbel.gov.br/phocadownload/produtos/manuais/fz-ca/manual-fz762m964.pdf. Acesso em: 7 jun. 2025.
[25] INDÚSTRIA DE MATERIAL BÉLICO DO BRASIL (IMBEL). **Manual do Usuário do Fuzil de Assalto 5,56 – IMBEL A2**: operação e manutenção. Brasília, DF: IMBEL, 2017. Disponível em: https://www.imbel.gov.br/phocadownload/produtos/manuais/fz-ca/manual-fuzil-imbel-556-IA2.pdf. Acesso em: 7 jun. 2025.
[26] BEHRINGER. ECM8000: Ultra-linear measurement condenser microphone – Technical Specifications, Music Tribe Global Brands Ltd., 2021. Disponível em: https://www.behringer.com/product.html?modelCode=0506-AAA. Acesso em: 7 jun. 2025.
[27] CALHOUN, R. B. *et al*. Precision and accuracy of acoustic gunshot location in an urban environment. **ShotSpotter Inc.**, Newark, v. 1, p.9-16, 2020. https://doi.org/10.48550/arXiv.2108.07377
[28] SILVA, R. L. A. **Sistema Detector e Localizador de Caçador**. Projeto de Final de Curso (Bacharelado em Engenharia de Comunicações) – Instituto Militar de Engenharia (IME), Rio de Janeiro, Brasil, 2023.

PÓS-GRADUAÇÃO NO IME

Bolsas: CAPES, CNPq e FAPERJ

Mestrado

- Sistemas e Computação
- Engenharia Mecânica

Mestrado e Doutorado

- Química
- Ciência dos Materiais
- Engenharia de Defesa
- Engenharia Nuclear
- Engenharia Elétrica
- Engenharia de Transportes

Matrículas: Semestral

Tel.: (21) 2546-7114 – Fax: (21) 2546-7089 – www.ime.eb.br – sd1@ime.eb.br